

**Universität
Rostock**



Traditio et Innovatio



Frontal Instability and Energy Dissipation in Submesoscale Fronts

Dissertation

zur

Erlangung des akademischen Grades

doctor rerum naturalium (Dr. rer. nat.)

der Mathematisch-Naturwissenschaftlichen Fakultät

der Universität Rostock

vorgelegt von

Jen-Ping Peng,

geb. am 24. September 1990 in Taipei City, Taiwan (R.O.C.)

Rostock, Juni 2020



Dieses Werk ist lizenziert unter einer
Creative Commons Namensnennung - Nicht-kommerziell - Weitergabe
unter gleichen Bedingungen 4.0 International Lizenz.

Gutachter:

1. PD Dr. Lars Umlauf
Leibniz-Institut für Ostseeforschung Warnemünde
2. Prof. Dr. Bill Smyth
Oregon State University, USA

Datum der Einreichung: 25 Juni 2020

Datum der Verteidigung: 13 November 2020

Abstract

Theory and numerical simulations suggest that submesoscale fronts and filaments are subject to various types of instabilities, providing a potentially important pathway for the downscale transport and dissipation of mesoscale kinetic energy in the ocean. This thesis discusses the real-ocean relevance of these recent concepts based on high-resolution turbulence microstructure and near-surface velocity data from transient submesoscale upwelling filaments in the Benguela upwelling system (South-East Atlantic). The focus of this study is sharp submesoscale fronts located at the edge of the filaments, characterized by persistent downfront winds, a strong frontal jet, and vigorous turbulence under different buoyancy forcing conditions. The data measured in the presence of destabilizing surface forcing reveal three distinct frontal stability regimes: forced symmetric instability (SI) in a deep mixing layer region, inertial/symmetric instability (ISI) on the anticyclonic side of the front, and marginal shear instability on the cyclonic side. Dissipation rates in these regions agree quantitatively and qualitatively with recent numerical simulations of forced SI and ISI. For the first time, a dataset obtained under negligible net buoyancy forcing has revealed an unforced SI in the surface boundary layer, which is ignored in the current parameterizations. This differs from the thermocline region, where turbulence inside a thin mixing layer was driven by a cross-front inertial shear. Finally, a further dataset obtained in the presence of stabilizing buoyancy forcing reveals a complete shut-down of frontal instability, and that the turbulence is controlled by surface forcing. The observations in this thesis provide direct evidence for the relevance of forced/unforced SI, ISI, and marginal shear instability for overall energy dissipation in submesoscale fronts and filaments.

Zusammenfassung

Theorie und numerische Simulationen legen nahe, dass submesoskalige Fronten und Filamente verschiedener Arten von Instabilitäten unterliegen, was einen potenziell wichtigen Weg für den Transport und die Dissipation von mesoskaliger kinetischer Energie im Ozean darstellt. In dieser Arbeit wird die reale Ozeanrelevanz dieser neuen Konzepte diskutiert, die auf hochauflösenden Turbulenzmikrostruktur- und oberflächennahen Geschwindigkeitsdaten von transienten submesoskaligen Auftriebsfilamenten im Benguela-Auftriebssystem (Südostatlantik) basieren. Der Schwerpunkt dieser Studie liegt auf scharfen submesoskaligen Fronten am Rand des Filamente, die durch anhaltende Winde, einen starken Frontalstrahl und starke Turbulenzen unter verschiedenen Auftriebsbedingungen gekennzeichnet sind. Die in Gegenwart eines destabilisierenden Oberflächenantriebs gemessenen Daten zeigen drei unterschiedliche frontale Stabilitätsregime: erzwungene symmetrische Instabilität (SI) in einer tiefen, gut durchmischten Deckschicht und Trägheits/symmetrische Instabilität (ISI) auf der antizyklonalen Seite der Front und marginale Scherinstabilität auf der zyklonalen Seite. Die Dissipationsraten in diesen Regionen stimmen quantitativ und qualitativ mit numerischen Simulationen von SI und ISI überein. Der Datensatz, der unter vernachlässigbaren Auftriebsbedingungen aufgenommen wurde, zeigt zum ersten Mal eine ungezwungene SI in der Oberflächengrenzschicht, die bei der aktuellen Parametrisierung ignoriert wird. Dies unterscheidet sich von dem Bereich der Thermokline, in dem Turbulenzen innerhalb einer dünnen Mischschicht durch Trägheitsscherung an der Vorderseite der Front angetrieben wurden. Schließlich zeigt ein weiterer Datensatz, der in Gegenwart eines stabilisierenden Auftriebsantriebs erhalten wurde, eine vollständige Abschaltung der frontalen Instabilität und dass die Turbulenz durch Ober-

flächenantrieb gesteuert wird. Die Beobachtungen in dieser Arbeit liefern direkte Belege für die Relevanz von erzwungener/ungezwungener SI, ISI und marginaler Scherinstabilität für die Gesamtenergiedissipation in submesoskaligen Fronten und Filamenten.

Acknowledgements

In the last 3.5 years, there have been many individuals who have given me assistance and support on my Ph.D. research, life in Germany, and daily happiness, without which the research included in this dissertation could not have been performed.

First and foremost, I would like to express my deep gratitude to my thesis advisor Lars Umlauf for selecting me from about 10,000 km away as his Ph.D. student. He offered me so much advice, patiently supervised me as I undertook teaching and data analysis, and always guided me back to the right track when I get lost. Throughout my candidature, he always gave 100% making sure that all my writing and presentations were done perfectly. Without his help, I could not have finished my dissertation successfully.

I would also like to express my thanks to the Scientific Committee members, Hans Burchard, Gregor Rehder, Jeff Carpenter, and Alexa Griesel, for their constructive comments, which enabled me to make the necessary improvements to my Ph.D. research.

I am grateful of the help for my colleagues Peter Holtermann, who helped me to process the catamaran-ADCP data, is my co-author on my JPO paper, and checking my abstracts, and technicians Toralf Heene and Martin Sass for their technical support during the cruise. Because of your professional technical support, I was able to obtain wonderful data sets to complete my dissertation. Thanks to all the former colleagues who shared their office 214 with me in the last years and helped in many aspects (from science to daily life): Chris Lappe, Merten Siegfried, Selina Müller, and Madline Kniebusch. Special thanks to my current colleagues Marvin Lorenz for sharing his teaching experience of the lecture and correcting my German abstract, Evridiki Chrysagi for welcoming me at the first day of my arrival in the IOW, discussing the theory of submesoscale processes, and always traveling with me to different conferences, and Nicky Koganti for motivating me to lift 120 kg in the gym, and sharing Indian culture and food with me. Thanks also to my colleagues Martin Schmidt, Knut Klingbeil, Manja Placke, Xaver Lange, Florian Börgel, Hadi Bordbar, Mahdi Mohammadi-Aragh,

Sadegh Yari, Fernanda Nascimento, and Natalia Herran for having nice conversations with me, and sharing useful techniques and experiences. I would also like to thank our department secretary Berit Recklebe for giving me assistance with countless administrative issues.

Many thanks are also given to my TRR181 friends: Serhat Can, Bastian Sommerfeld, Marwa Almowafy, and Kesava Ramachandran, and my Chinese-speaking friends: Dandan Shen, Simeon Chou, Yeong Zen Chua, Rongrong Xie, Quan Zhou, Mo Zhou, and Daniel T. Gschwind for accompanying me in the last years and bringing happiness to my life. Special thanks to Valeska Borges for helping me to settle down in my first home in Germany, and Melissa Hampton-Smith for carefully proofreading my dissertation and kindly sharing land with me to plant flowers.

Finally, I am deeply grateful for the support of my family. Their understanding and love encouraged me to work hard and to complete my Ph.D. work. I particularly thank my sweetheart Lin Chen, who is always with me, makes my flat a home, and pushes me towards my goal.

This research included in this dissertation is part of subproject T2 of the Collaborative Research Centre TRR181 (Energy Transfers in Atmosphere and Ocean), funded through grant 274762653 by the German Research Foundation (DFG).

Contents

1. Introduction	1
1.1. Background and motivation	1
1.2. Current state of understanding	4
1.2.1. Modeling	4
1.2.2. Observations	6
1.3. Thesis objectives and outline	8
2. Theory	9
2.1. Frontogenesis	9
2.2. Classification of frontal instability	11
2.3. Forced symmetric instability	12
2.3.1. Destabilizing surface forcing	12
2.3.2. Forced SI layer	13
2.3.3. Modeled SI dissipation rate	14
2.4. Inertial/symmetric instability	17
2.5. Turbulence parameters	18
2.5.1. Monin-Obukhov scale	18
2.5.2. Ozmidov scale	19
2.5.3. Richardson number	19
3. Study area, instruments and methods	20
3.1. Study area: the Benguela upwelling system	20
3.2. Instruments	22
3.2.1. Turbulence microstructure profiler	22
3.2.2. Velocity measurements	23
3.2.3. Near-surface CTD measurements	24
3.2.4. Atmospheric data	24
3.2.5. Satellite data	25

3.3. Methods	25
3.3.1. Front-based coordinate system	25
3.3.2. Data averaging procedure	26
4. Frontal instability and energy dissipation under destabilizing surface forcing	28
4.1. Filament evolution and structure	28
4.1.1. Formation stage	29
4.1.2. Mature stage	30
4.1.3. Decay stage	32
4.2. Atmospheric forcing	32
4.3. Frontal structure and stability regime classification	34
4.3.1. Frontal structure	34
4.3.2. Stability regime classification	36
4.4. Analysis of frontal instability and turbulence	38
4.4.1. Regions I and II: Deep mixing layers	38
4.4.2. Region III: Effect of anticyclonic vorticity	41
4.4.3. Regions IV-VI: Main frontal region	43
4.5. Discussion	46
4.6. Summary	47
5. Frontal instability and energy dissipation under variable surface forcing	50
5.1. Filament structure and evolution	50
5.2. Atmospheric forcing	52
5.3. Frontal structure	54
5.3.1. Density-compensated front (FO1)	54
5.3.2. Dynamically active front (FO2)	56
5.3.3. Hydrographic and mixing properties	58
5.4. Analysis of frontal instability and turbulence	60
5.4.1. The core frontal region	60
5.4.2. The anticyclonic region	61
5.4.3. The thermocline region	64
5.4.4. Wind-forced inertial oscillation	66
5.5. Discussion	68
5.6. Summary	70

6. Conclusion and outlook	73
6.1. Overview	73
6.2. Conclusion	73
6.3. Outlook	75
A. Accuracy of satellite SSH data	79
B. Catamaran-mounted ADCP correction	81
C. Isopycnal averaging procedure	83
D. Curriculum vitae	84
Bibliography	88

Chapter 1.

Introduction

This thesis is an effort to gain a better understanding of submesoscale dynamics in surface mixed layer fronts of the ocean. As this work is part of the interdisciplinary project “Energy transfers in atmosphere and ocean” (TRR181), the main focus of this thesis is energy transfer in the ocean, with special attention paid to submesoscale frontal instabilities and associated energy dissipation. So far, relevant studies have been largely based on theoretical and numerical modeling; observation-based studies are still limited. Thus, this study will be carried out using turbulence and hydrographic observations.

1.1. Background and motivation

Submesoscale fronts and filaments with typical evolutionary time scales of hours to days are frequently observed at scales around 0.1-10 km in the surface boundary layer (SBL) of the ocean and have been extensively studied in recent decades due to their significant impact on the upper ocean (McWilliams, 2016; Mahadevan, 2016; Lévy et al., 2018). The classical view of oceanic dynamical regimes covers a wide range of processes, ranging from geostrophically-balanced motions, such as planetary scale currents and mesoscale eddies, to gravity waves (e.g. Rossby waves), and ultimately down to small-scale turbulence where kinetic energy is dissipated by viscous friction (Olbers et al., 2012). The physical role of the submesoscale regime in this spectrum of motions is not well understood at the moment.

Besides the unique temporal and length scales of submesoscale motions, it has been shown that the submesoscale regime is also dynamically distinct from balanced mo-

tions and small-scale turbulence as it is characterized by both *Rossby numbers* $Ro = \zeta/f$ and *Richardson numbers* $Ri = N^2/S^2$ of $\mathcal{O}(1)$ (Thomas et al., 2008), where ζ is the vertical component of the relative vorticity, f is the Coriolis parameter, and N^2 and S^2 are the square of the buoyancy frequency and the total velocity shear, respectively. The spatial and temporal regime of submesoscale motions relative to other more classical dynamical regimes of the ocean is illustrated in Fig. 1.1. This figure shows that the submesoscale regime partly overlaps with internal-wave motions. Although their scales are similar, the latter can be easily distinguished from submesoscale motions by their special oscillatory and propagation properties (McWilliams, 2016).

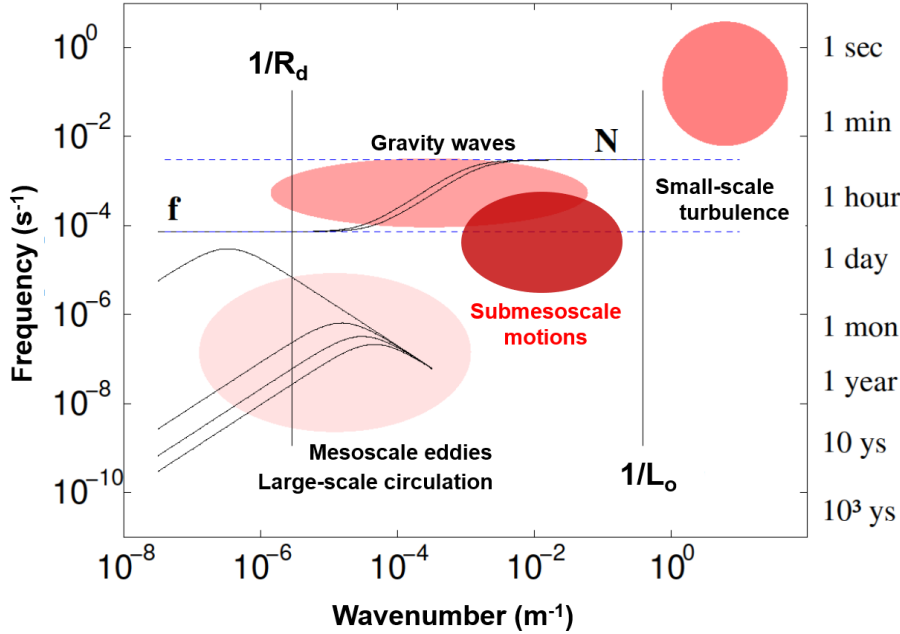


Figure 1.1.: Schematic view of the space-time scales of the principle dynamical regimes in the ocean including the submesoscale regime. Solid lines mark the dispersion relations for linear gravity waves (upper set) and planetary waves (lower set) with internal waves bounded by the Coriolis frequency f and the buoyancy frequency N . Small-scale turbulence is separated from gravity waves and submesoscale motions by the Ozmidov scale L_o . This figure is a modified version from the proposal for a large-scale German project cluster entitled “Energy transfers in atmosphere and ocean” (TRR181), in which also this thesis is embedded.

Research is increasing on submesoscale dynamics, and one of the major areas of interest is related to the large vertical velocities of $\mathcal{O}(100 \text{ m day}^{-1})$ induced by submesoscale motions in the SBL (Mahadevan and Tandon, 2006). These motions significantly modify upper ocean properties through the vertical transport of physical and

biogeochemical tracers, such as heat, salt, and dissolved gases. Previous studies have also shown that this upward transport can bring nutrient-rich water from lower layers up into the light-rich surface layer, allowing phytoplankton to photosynthesize (Lévy et al., 2012; Mahadevan, 2016), thereby forming fertile fishing grounds (Snyder et al., 2017). The downward transport, on the other hand, is capable of subducting dissolved substances into the thermocline (e.g., Nagai et al., 2009; Lévy et al., 2010), leading to a vigorous exchange of tracers between the atmosphere, ocean surface, and ocean interior. These subductions are more effective on the cold side of fronts and filaments, where the downward velocities are particularly intense (Gula et al., 2014).

Besides the effect of large vertical transport of the tracers, there is a large body of literature on the study of SBL restratification generated by energetic submesoscale flows (Boccaletti et al., 2007; Fox-Kemper and Ferrari, 2008; Fox-Kemper et al., 2008, 2011). These studies have shown that submesoscale fronts characterized by strong lateral density gradients cause a slumping of the frontal isopycnals and thus lead to restratification of the SBL on a timescale of days, which is more effective in restratifying the SBL compared to geostrophic adjustment (Tandon and Garrett, 1995). Moreover, Mahadevan (2016) suggested that there is a link between the shoaling of the SBL and primary production, that is, phytoplankton that used to live in the light-limited lower layers is now trapped in the light-rich surface layer by stratification.

As the work of this thesis is part of the large-scale German project cluster “Energy transfers in atmosphere and ocean”, the major motivation of this thesis is the oceanic forward energy cascade generated by submesoscale flows. It has long been recognized that the large-scale circulation, forced by the planetary-scale frictional and buoyancy fluxes at the surface, transfers energy toward mesoscale eddies through balanced instability (Charney, 1971). Due to the balance constraint of the large-scale geostrophic dynamics, i.e. the effect of Earth’s rotation and stratification, these balanced eddies do not provide a route to dissipation, instead, energy is transferred back to large-scale circulation. Thus, in principle, the energy of the balanced regime is conserved in quasi-geostrophic approaches if (parameterized) direct energy losses, e.g. due to bottom friction, are ignored. There is, however, increasing evidence from current ocean models demonstrating that energy is typically lost from the system (Eden and Greatbatch, 2008; Eden et al., 2014).

Xu et al. (2014) found significant temperature biases in climate models, especially in the upwelling regions of the World Ocean, such as the Benguela and Peruvian upwelling system in the Southern Hemisphere on which also this thesis will focus. Biases

in the ocean components of present climate models have also been shown to significantly affect climate predictions (Lucarini and Ragone, 2011; Lucarini et al., 2014). Such temperature biases in climate models may be, at least partly, related to an incorrect representation of the energy cascade in the ocean, and it has been shown that they cannot be eliminated by increased resolution alone (Harlass et al., 2015). Therefore, it is crucial to have a complete understanding of how geostrophically-balanced mesoscale energy is dissipated. As shown in this thesis, submesoscale motions play a key role in this process.

1.2. Current state of understanding

1.2.1. Modeling

Recent theoretical and numerical studies have shown that submesoscale fronts and filaments are thought to be generated by the frontogenesis via mesoscale advective deformation of a preexisting horizontal buoyancy gradient (Hoskins, 1982; Capet et al., 2008), destabilizing Ekman transport driven by “downfront” winds (Thomas, 2005), baroclinic instability of the weakly stratified SBL (Fox-Kemper et al., 2008), and/or other processes related to, e.g., upwelling, differential mixing, and river plumes. It has been shown these processes break the balance constraint of large-scale quasi-geostrophic dynamics via frontogenesis and lead a downward transport of mesoscale energy (McWilliams, 2016). These processes may be especially relevant in the SBL, where other energy sinks such as bottom friction (Sen et al., 2008) and spontaneous emission of internal gravity waves (Nikurashin and Ferrari, 2011; Nikurashin et al., 2013), are likely less relevant.

A number of studies point to the importance of a special class of instabilities that occur in stably stratified flows if the Ertel potential vorticity, q , and the Coriolis parameter, f , attain the opposite signs: $f q < 0$. As summarized by Thomas et al. (2013), two distinct instabilities can be identified in this case: inertial/centrifugal instability, observed in situations with anticyclonic relative vorticity ζ satisfying the condition $f(f + \zeta) < 0$, and symmetric instability (SI) that may occur in stably stratified baroclinic fronts if the absolute vorticity is cyclonic: $f(f + \zeta) > 0$. Of the two, SI has been studied more intensively as ocean fronts are usually located inside energetic hotspots (like the Gulf Stream). These hotspots also have far-reaching effects in other (non-

baroclinic) areas of the ocean, often drawing scientists' attentions. It has been shown that SI forms in the stably stratified SBL under destabilizing atmospheric forcing and downfront winds (Thomas, 2005). Unlike other mixing processes in the SBL that draw energy from winds, surface waves, or atmospheric buoyancy loss, SI grows at the expense of the kinetic energy from the balanced background flow (Taylor and Ferrari, 2010; Thomas and Taylor, 2010). Thus, it represents a sink of balanced large-scale energy, and may therefore trigger a forward energy cascade towards the dissipative scales. In addition, another forward route is through ageostrophic anticyclonic instability (Molemaker et al., 2005; Müller et al., 2005; Barkan et al., 2015). This type of instability is generated when $f + \zeta < S_{st}$, where $S_{st} = ((u_x - v_y)^2 + (v_x + u_y)^2)^{1/2}$ is the strain rates, and u and v are horizontal velocity components. Note that the conditions for ageostrophic anticyclonic instability are easier to satisfy than the conditions of inertial instability ($f + \zeta < 0$).

However, these submesoscale instabilities themselves are not responsible for dissipation as the scales of their structures are still too large to be directly associated with viscous dissipation. This gap between submesoscale motions and small-scale turbulence is also visible in the dynamical regimes shown in Figure 1.1. Based on evidence from large eddy simulations of SI, Taylor and Ferrari (2009) suggested that the final step towards the scales of three-dimensional turbulence and dissipation is bridged by secondary Kelvin-Helmholtz (KH) instabilities. By now, with the above arguments in mind, the oceanic energy routes can be summarized visually as shown in Figure 1.2.

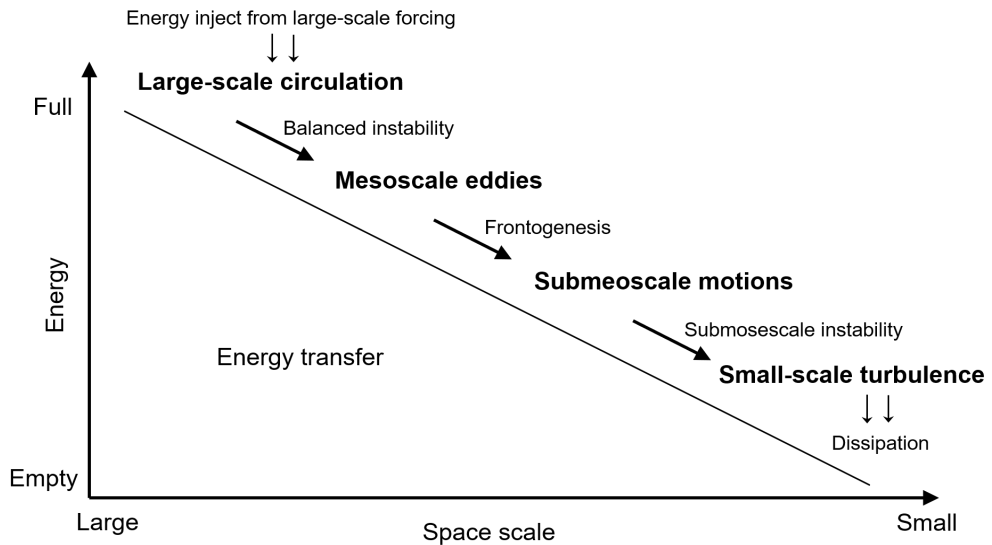


Figure 1.2.: Schematic of the forward energy cascade between oceanic dynamical regimes from large-scale forcing to dissipation.

1.2.2. Observations

While a growing body of work from theoretical and numerical models suggests that submesoscale dynamics play a major role in the dissipation of mesoscale energy, observation-based research, required to test the real-ocean relevance of the recent concepts described above, is still largely lacking. Despite submesoscale features being ubiquitous in the open ocean, field observations on submesoscale dynamics and associated energy dissipation in the SBL is notoriously challenging. On the one hand, the unique spatial and temporal scales of submesoscale motions are too small for many satellites and too quick for ship surveys. On the other hand, a full suite of physical processes in the SBL are known to dominate near-surface mixing processes as illustrated in Figure 1.3, such as convection, the breaking of gravity waves, and wind-driven turbulence, to name a few (Sullivan and McWilliams, 2010). This makes it difficult to separate turbulence associated with submesoscale motions from other processes.

Recent field studies including turbulence microstructure observations have confirmed that submesoscale fronts are regions of enhanced mixing (e.g., Nagai et al., 2009, 2012; Johnston et al., 2011). However, comprehensive investigations that combine turbulence and hydrographic data at resolutions sufficient to resolve the extreme gradients in narrow and quickly evolving submesoscale fronts are still largely missing from the literature. A notable exception is the study of frontal instability and mixing in the Kuroshio Current by D’Asaro et al. (2011), who combined ship-based observations with turbulence data from a tracked Lagrangian float drifting along with the frontal jet. They were the first to conclusively show that enhanced energy dissipation found in a narrow frontal region was generated by forced symmetric instability, and scaled with the Ekman buoyancy flux. A follow-up study in a Gulf Stream front using similar instrumentation (Thomas et al., 2016) arrived at the same conclusions, however, with the caveat that near-inertial waves may induce transient modifications.

In very recent years, important insights into the SI-induced turbulence were gained from a state of the art combination of oceanic instruments and airborne observations in the North Wall of the Gulf Stream (Savelyev et al., 2018). An interesting outcome of this study was the staircase signature of the coherent structures associated with SI turbulence, which were distinctly larger than the structures associated with Langmuir circulation. The decay timescale of kinetic energy from the background flow due to SI was estimated to be of $\mathcal{O}(\text{hours})$. This study was the first to directly show the surface temperature field of SI-induced turbulence without exhibiting the conditions for SI

that were fulfilled. Another novel study was based on a combination of autonomous instruments and multiple mooring observations in a transient front, which argued that the occurrence of symmetric instability in a quiescent open-ocean environment can be seen as representative of a substantial fraction of the global ocean (Yu et al., 2019). So far, there are only a few studies available and none of them showed the vertical structure of SI-induced turbulence. This is the main gap that this thesis dedicates to closing.

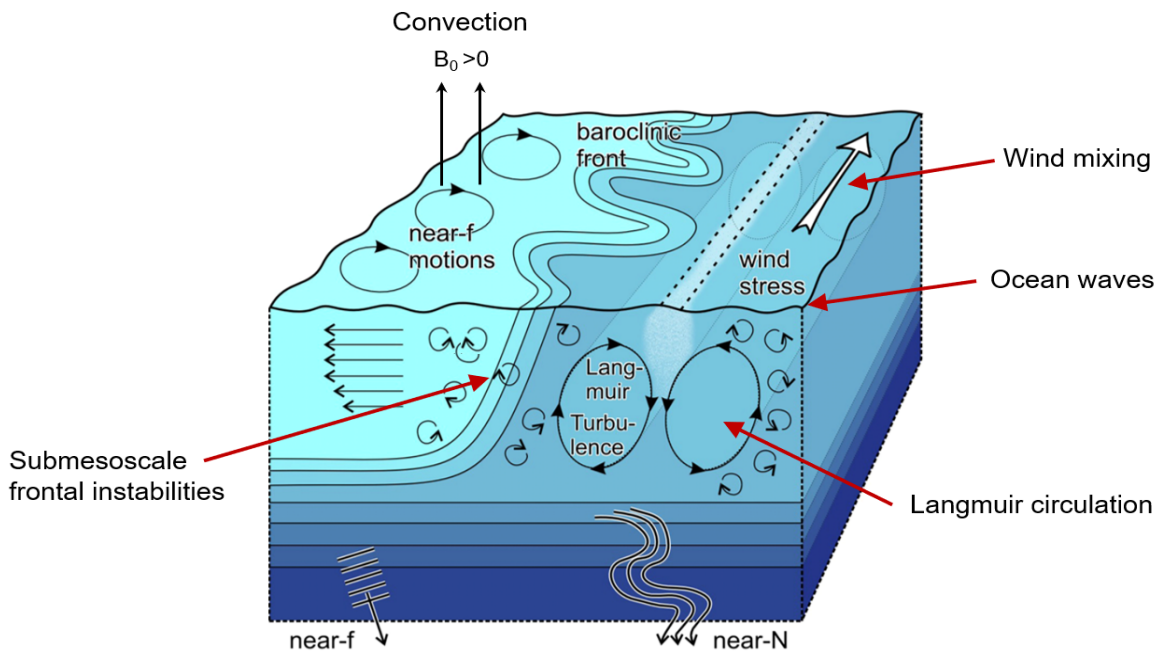


Figure 1.3.: Sketch of dominant mixing processes in the SBL, all of which are associated with small-scale turbulence. These include from left to right: inertial oscillations, convection, submesoscale frontal instabilities, Langmuir turbulence, ocean waves, and wind mixing. Also indicated are the internal waves near the inertial and buoyancy frequencies, respectively, that may be triggered by motions in the SBL. This figure is modified from the proposal for the project “Energy transfers in atmosphere and ocean” (TRR181).

1.3. Thesis objectives and outline

The objective of this thesis is to expand the understanding of submesoscale dynamics in the SBL and associated frontal instabilities that are potential pathways of downscale transport of mesoscale energy. The state of the art of the theory of frontal instability and energy dissipation that forms the starting point of this study is revisited in Chapter 2. Motivated by the large biases in climate models that frequently appear in upwelling regions (Xu et al., 2014), the Benguela upwelling system was selected as the study area. A unique combination of turbulence and velocity measurements were designed to overcome the challenges of observing narrow and quickly evolving submesoscale fronts. General information concerning the research cruise, the study area, the deployed instruments, and the methods of data analysis are summarized in Chapter 3. The investigation of potential conduits of a forward energy cascade under destabilizing surface forcing was accepted in May 2020 by the *Journal of Physical Oceanography* in an article entitled "Frontal instability and energy dissipation in a submesoscale upwelling filament". The analysis and main results of this study are described in Chapter 4 of this thesis. So far, unpublished results from a different submesoscale filament are described in Chapter 5, focusing on the effect of varying surface forcing on SBL instability. Finally, a summary of the main contributions of this thesis to the understanding of frontal instability and energy dissipation in submesoscale fronts, as well as some suggestions for future research is provided in Chapter 6.

Chapter 2.

Theory

This chapter summarizes the state of the art regarding the theoretical description of frontal instability and energy dissipation, required to understand the core Chapters 4 and 5 of this thesis. Some parts of this summary are described in a similar form in the publication by Peng et al. (2020).

2.1. Frontogenesis

The classical view is that fronts and filaments are quickly intensified by frontogenesis induced by a quasi-geostrophic mesoscale strain field, sharpening lateral density gradients and accelerating the frontal jet, as illustrated in Figure 2.1 (note that the sketch has adapted to the southern hemisphere, where $f < 0$). The time scale of this formation process is of the order of a few days (Hoskins and Bretherton, 1972). There is increasing evidence from recent numerical studies that late-stage submesoscale frontogenesis is affected, or even dominated, by an ageostrophic secondary overturning circulation that is tightly connected to strong vertical velocities and vertical turbulent mixing (Mahadevan and Tandon, 2006; Gula et al., 2014; McWilliams et al., 2015). However, the fronts generated by mesoscale straining are inefficient in transferring energy toward smaller scale and dissipation because of the balance constraint of the large-scale quasi-geostrophic dynamics (Lévy et al., 2012). One way to promote frontogenesis is via surface forcing, as suggested by Thomas (2005). When the winds blow in the direction of the frontal jet, a cross-front Ekman transport is triggered, intensifying the front by transporting dense water over light water, that prevents further slumping of the frontal isopycnals due to the ageostrophic secondary overturning cir-

ulation. This point is considered further in Section 2.3 below.

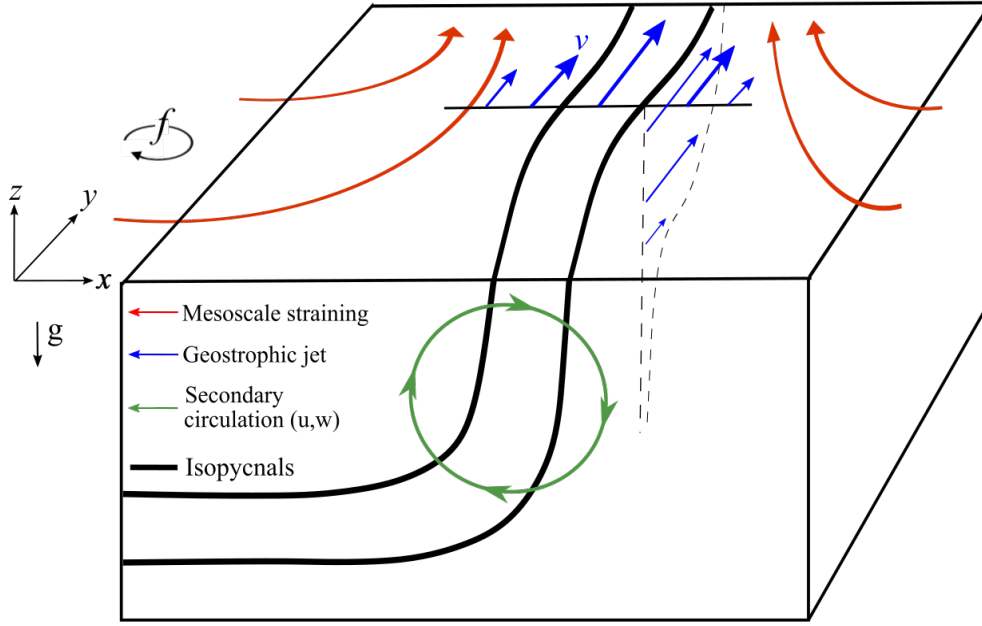


Figure 2.1.: Sketch of the classical view of frontogenesis for the southern hemisphere: The horizontal mesoscale straining (red) creates a confluent density front, intensifying the geostrophic sheared currents in the alongfront direction (blue), and inducing a secondary circulation that tends to flatten tilted isopycnals (green). The cross-front x , alongfront y , and vertical z current speeds that are denoted as u , v and w . This coordinate system of a two-dimensional front (assuming no variations in y direction) will be frequently used in the following.

In the real-ocean, submesoscale fronts can be briefly categorized into persistent fronts and ephemeral fronts. There is a rich literature on the study of persistent fronts, showing that these fronts are associated with persistent large-scale boundary currents, such as the Kuroshio (D’Asaro et al., 2011; Nagai et al., 2012) and Gulf Stream (Thomas et al., 2013, 2016). These studies have shown that if seasonal winds are directed in the downfront direction, they drive a cross-front Ekman transport, due to which the front sharpens, the near-surface stratification decreases, and the frontal jet strengthens. These observations reveal that the entire process of frontogenesis can be completed by surface forcing alone without any support from mesoscale straining, which is different from the classical view of frontogenesis.

Ephemeral fronts, on the other hand, are often observed in upwelling regions (Thomsen et al., 2016; Köhn et al., 2017; Dräger-Dietel et al., 2018) and river plumes

(Jay et al., 2009; Ramachandran et al., 2018). Unlike the fronts in large-scale current systems, this type of fronts is more unpredictable in terms of location and time since they are continuously forming, moving and dissipating. The frontogenesis of such fronts requires a more complex process that inextricably links with mesoscale straining, surface forcing, and baroclinic instability. E.g., Peng et al (2020) revealed the possibility of incorporated working of both downfront winds and mesoscale straining on the intensification of a density front based on observations.

2.2. Classification of frontal instability

Summarizing the conditions for inertial and symmetric instabilities in stably stratified flows, Thomas et al. (2013) pointed out that these types of instability are expected to occur if the Ertel PV, q , and the Coriolis parameter, f , have opposite signs:

$$fq = f(f\hat{\mathbf{k}} + \nabla \times \mathbf{u}) \cdot \nabla b < 0, \quad (2.1)$$

where $\hat{\mathbf{k}}$ is the upward unit vector, ∇ is the gradient operator, $\mathbf{u} = (u, v, w)$ is the velocity vector, and $b = -g\rho_\theta/\rho_0$ the buoyancy, here defined based on the gravitational acceleration g , the potential density ρ_θ , and the reference density $\rho_0 = 1026 \text{ kg m}^{-3}$.

The PV can be decomposed into vertical and baroclinic components, q_ζ and q_{bc} , and (2.1) can thus be rewritten as

$$fq = f(q_\zeta + q_{bc}) < 0. \quad (2.2)$$

The first component is associated with vertical vorticity and stratification,

$$q_\zeta = (f + \zeta)N^2, \quad (2.3)$$

where $\zeta = \hat{\mathbf{k}} \cdot (\nabla \times \mathbf{u})$ is the vertical component of the relative vorticity, and $N^2 = \partial b / \partial z$ the square of the buoyancy frequency. The baroclinic component can be written as

$$q_{bc} = \left(\frac{\partial w}{\partial y} - \frac{\partial v}{\partial z} \right) \frac{\partial b}{\partial x} + \left(\frac{\partial u}{\partial z} - \frac{\partial w}{\partial x} \right) \frac{\partial b}{\partial y}. \quad (2.4)$$

Two types of instability are generally distinguished in stably stratified flows with negative fq : SI is expected to occur for $|fq_{bc}| > fq_\zeta$ with $fq_\zeta > 0$ (absolute vorticity is

cyclonic), whereas flows with $f q_\zeta < 0$ are susceptible to inertial/centrifugal instability (Thomas et al., 2013).

For a two-dimensional front, using the coordinate system defined in Figure 2.1, these two components of the PV reduce to

$$q_\zeta = \left(f + \frac{\partial v}{\partial x} \right) N^2, \quad q_{bc} = \frac{\partial v}{\partial z} M^2, \quad (2.5)$$

where we introduced $M^2 = -\partial b / \partial x$ to denote the cross-front buoyancy gradient. Note that following the definition of the cross-front x -coordinate, $M^2 > 0$ is generally true inside the frontal region. From (2.2) and (2.5), it is clear that cyclonic shear has a stabilizing tendency, whereas, at least in geostrophically balanced fronts with $f q_{bc} = -M^4$, the baroclinic term is always destabilizing. As shown in Chapters 4 and 5 below, both effects are generally important in this study.

2.3. Forced symmetric instability

2.3.1. Destabilizing surface forcing

Thomas (2005) argued that SI can only be sustained by an upward PV flux through the sea surface, permanently draining PV from the SBL. He showed that conditions are favorable for such “forced” SI (FSI) if the sum of the atmospheric buoyancy flux, B_0 , and the Ekman buoyancy flux,

$$B_E = -\frac{\tau_y^w M^2}{\rho_0 f}, \quad (2.6)$$

is positive: $B_0 + B_E > 0$ (here, τ_y^w denotes the downfront component of the wind stress). FSI can thus only persist if the net surface forcing acts to gravitationally destabilize the SBL, either by a destabilizing atmospheric buoyancy flux (e.g., cooling) or by a cross-front Ekman transport that moves dense water on top of lighter water, as illustrated in Figure 2.2 (Note that this example has been adapted to the southern hemisphere, where $f < 0$)

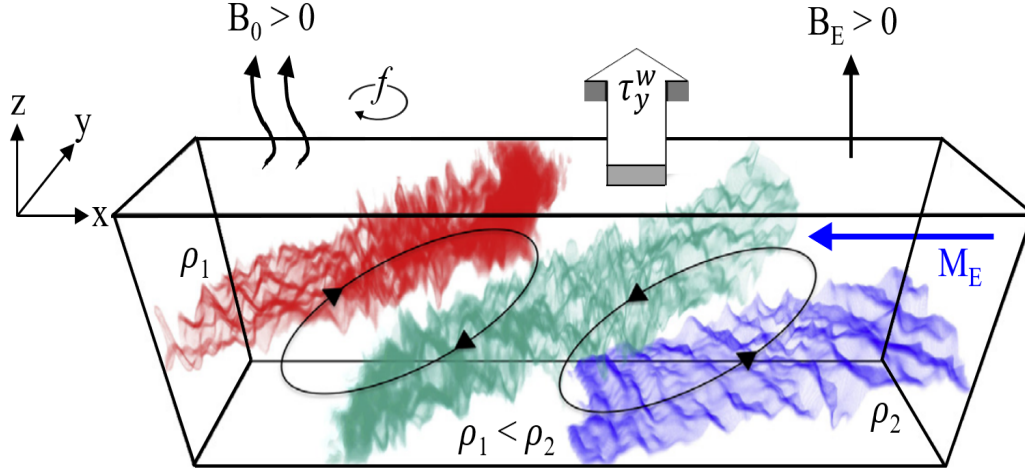


Figure 2.2.: A visualized schematic of SI overturns under destabilizing surface forcing ($B_0 + B_E > 0$) for the Southern Hemisphere. Downfront winds τ_y^w drive a cross-front Ekman transport $M_E = \tau_y^w / \rho_0 f$ (blue arrow) that lifts dense water over light water, reduces the stratification and PV near the surface, and drives the flow toward an SI-unstable state. The resulting SI overturning cells act along isopycnals (color planes) to extract kinetic energy from the background flow, leading to a down-scale transport of kinetic energy towards small-scale turbulence and dissipation. This figure is modified from Bachman et al. (2017).

2.3.2. Forced SI layer

From idealized numerical simulations of FSI, Taylor and Ferrari (2010) describe a turbulent low-PV layer of thickness H as an extension of the classical concept of the “mixed layer”. This low-PV layer is composed of two sublayers with distinct vertical structure and dynamics, as illustrated in Figure 2.3. They found that the upper part of the low-PV layer is characterized by a well-mixed region of thickness h , in which turbulence is directly driven by surface forcing, as in classical convection. Underneath this convective layer, a forced SI layer was shown to develop, under the obvious geometrical constraint that $h/H < 1$. Different from the convective layer, the forced SI layer is characterized by significant stable stratification.

Taylor and Ferrari (2010) derived an implicit relation for the convective layer depth,

$$h^{4/3} = c \frac{f^2}{M^4} (B_0 + B_E)^{2/3} \left[1 - (1 + \alpha_e + \beta_e) \frac{h}{H} \right], \quad (2.7)$$

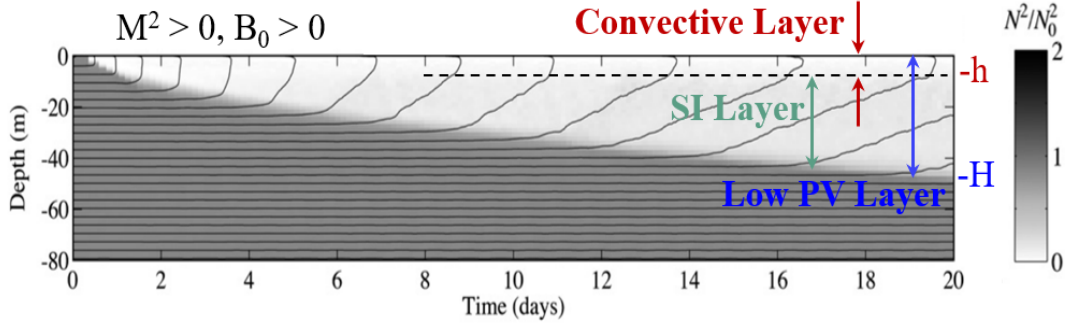


Figure 2.3.: Illustration of the two-layer structure of the near-surface region at a density front ($M^2 > 0$) under convection ($B_0 > 0$) from a simulation of Taylor and Ferrari (2010). The evolution of the normalized buoyancy frequency and isopycnals corresponding to this scenario are shown in background gray shading and contours, respectively. This figure is modified from Taylor and Ferrari (2010).

where $c \approx 14$ is a model constant, and α_e and β_e are two entrainment parameters. That latter are not well constrained but have been shown to play only a relatively small role (Taylor and Ferrari, 2010). In this thesis, following Thomas et al. (2013), $\alpha_e = \beta_e = 0$ is assumed. For the data analysis in later chapters, the vertical thickness H of the low-PV layer was identified with the near-surface region with negative fq (if existing). This definition of the low-PV layer thickness H has the advantages that it does not require any modeling assumptions, avoids the assignment of an (arbitrary) threshold for “low” PV, and is directly connected to the stability condition in (2.2). A sharp increase of fq for $z < -H$ was generally found, such that practically little ambiguity arises about the thickness of the low-PV layer.

2.3.3. Modeled SI dissipation rate

Taylor and Ferrari (2010) identified from large eddy simulations that the geostrophic shear production, $P = \langle v'w' \rangle M^2 / f$, and the negative buoyancy production, $G = \langle w'b' \rangle$, act as a sink of kinetic energy of the geostrophic background flow. The Reynolds average and the deviations from the Reynolds average are denoted as $\langle \cdot \rangle$ and the primes, respectively. Moreover, they derived a relation between $P + G$ and the external forcing using frontal parameters. Based on this work, Thomas and Taylor (2010) showed that the rate at which FSI extracts kinetic energy from the background flow scales with $B_0 + B_E$, and linearly decreases from $B_0 + B_E$ at the surface to zero at the bottom of the low-PV layer.

To derive this important result, the first step is to start from the linearized form of the cross- and along-front momentum equations:

$$\begin{aligned}\frac{\partial u}{\partial t} - fv &= -\frac{1}{\rho_0} \frac{\partial p}{\partial x} + \frac{\partial}{\partial z} \left(\nu \frac{\partial u}{\partial z} - \langle u'w' \rangle \right), \\ \frac{\partial v}{\partial t} + fu &= -\frac{1}{\rho_0} \frac{\partial p}{\partial y} + \frac{\partial}{\partial z} \left(\nu \frac{\partial v}{\partial z} - \langle v'w' \rangle \right),\end{aligned}\quad (2.8)$$

where the coordinate system defined in Figure 2.1 has been adopted, and the kinematic viscosity ν are introduced. The linearized version of the transport equation for buoyancy, that can be derived from the T and S equations, can be written as:

$$\frac{\partial b}{\partial t} - M^2 u = \frac{\partial}{\partial z} \left(\nu^b \frac{\partial b}{\partial z} - \langle w'b' \rangle \right) + \frac{\partial I_b}{\partial z}, \quad (2.9)$$

where the molecular diffusivity of buoyancy ν^b , which corresponds to either the molecular diffusivity of temperature ν^θ or the molecular diffusivity of salinity ν^S , and the local buoyancy gain due to absorption of solar radiation $I_b = \alpha g Q_{SW} / \rho_0 C_p$ (in $\text{m}^2 \text{s}^{-3}$) as the only external source, in which thermal expansion coefficient α , short-wave solar radiation Q_{SW} (in W m^{-2}), and the heat capacity at constant pressure $C_p \approx 4000 \text{ (J kg}^{-1} \text{ K}^{-1})$, are introduced. Note that the last term with I_b only appears if b has been derived from the temperature equation.

Then, assuming stationarity in (2.8) and only considering two-dimensional fronts (no variations in the alongfront direction y) as defined in Figure 2.1, we have $\partial v / \partial t$ and $\partial p / \partial y = 0$, and the momentum equation in (2.8) becomes

$$fu + \frac{\partial}{\partial z} \langle v'w' \rangle = \frac{\partial}{\partial z} \left(\nu \frac{\partial v}{\partial z} \right). \quad (2.10)$$

The Coriolis force is balanced by viscous and turbulent stress, which is also known as the turbulent Ekman balance. Multiplying (2.10) by M^2/f and integrating the equation from arbitrary depth z to the surface, yields

$$M^2 \int_z^0 u \, dz - \frac{M^2}{f} \langle v'w' \rangle = \frac{\tau_y^w}{\rho_0} \frac{M^2}{f} - \frac{M^2}{f} \nu \frac{\partial v}{\partial z}, \quad (2.11)$$

where $\nu \partial v / \partial z$ at the surface is replaced by τ_y^w / ρ_0 , and $\langle v'w' \rangle = 0$ at the surface as $w' = 0$, assuming the absence of surface waves. Inserting the shear production $P = \langle v'w' \rangle M^2 / f$ and the Ekman buoyancy flux $B_E = -\tau_y^w M^2 / \rho_0 f$ and neglecting the last

term in (2.11) due to its small contribution gives

$$M^2 \int_z^0 u \, dz - P = -B_E \quad (2.12)$$

The vertical integral of (2.9) from arbitrary depth z to the surface of the form yields:

$$\int_z^0 \frac{\partial b}{\partial t} \, dz - M^2 \int_z^0 u \, dz = \left(\nu^b \frac{\partial b}{\partial z} + I_b \right) \Big|_{z=0} - \left(\nu^b \frac{\partial b}{\partial z} + I_b \right) + \langle w'b' \rangle, \quad (2.13)$$

where $\langle w'b' \rangle = 0$ at the surface where $w' = 0$. Adding (2.12) and (2.13) and using $G = \langle w'b' \rangle$ results in an expression of the form

$$\int_z^0 \frac{\partial b}{\partial t} \, dz - P = -B_E + \left(\nu^b \frac{\partial b}{\partial z} + I_b \right) \Big|_{z=0} + G, \quad (2.14)$$

where the terms involving the diffusivity and I_b at z are ignored, assuming that all solar radiation is absorbed at the surface. Now, recalling that the second term on the right hand side of (2.14) corresponds to the atmospheric buoyancy flux $B_0 = -(\nu^b \partial b / \partial z + I_b)$, (2.14) can be re-written as

$$P + G = B_E + B_0 + \int_z^0 \frac{\partial b}{\partial t} \, dz. \quad (2.15)$$

Taylor and Ferrari (2010) showed it is often justified to assume that $\partial b / \partial t$ is constant across the low-PV layer, thus the last term on the right hand side of (2.15) can be written as $-(\partial b / \partial t)z$. Now, recalling (2.9) and integrating again but now across the low-PV layer ($-H < z < 0$):

$$H \frac{\partial b}{\partial t} - M^2 \int_{-H}^0 u \, dz = \left(\nu^b \frac{\partial b}{\partial z} + I_b \right) \Big|_{z=0} - \left(\nu^b \frac{\partial b}{\partial z} + I_b \right) + \langle w'b' \rangle, \quad (2.16)$$

where the same assumptions are also made here so that I_b at $z = -H$ and $\langle w'b' \rangle$ at the surface are neglected. Following Taylor and Ferrari (2010), using the entrainment parameters at $z = -H$, $\alpha_e = (\langle w'b' \rangle - \nu^b \partial b / \partial z) / (B_0 + B_E)$ and $\beta_e = (-M^2 \tau_y^w / \rho_0 f + M^2 \int_{-H}^0 u \, dz) / (B_0 + B_E)$, into (2.16), results in an expression of the form

$$H \frac{\partial b}{\partial t} = (-1 + \alpha_e + \beta_e)(B_0 + B_E). \quad (2.17)$$

Replacing the last term of (2.15) by (2.17), yields

$$P + G = (B_0 + B_E) - \frac{z}{H}(-1 + \alpha_e + \beta_e)(B_0 + B_E). \quad (2.18)$$

Following Thomas et al. (2013), assuming $\alpha_e = \beta_e = 0$, (2.18) can be simplified as the following expression

$$P + G = (B_0 + B_E)\left(\frac{z + H}{H}\right). \quad (2.19)$$

This expression shows that the production rate at which FSI extracts kinetic energy from the background flow scales with surface buoyancy fluxes, and linearly decreases from $B_0 + B_E$ at the surface to zero at the bottom of the low-PV layer. Assuming that this energy is locally dissipated, and the flow is quasi-steady state ($\varepsilon = P + G$), the average of the dissipation rate across the low-PV layer ($-H < z < 0$) is

$$\varepsilon_{SI} = \frac{B_0 + B_E}{2}. \quad (2.20)$$

A modified version of (2.20) that only takes the forced SI layer ($-H < z < -h$) into account can be written as

$$\varepsilon_{SI} = \frac{B_0 + B_E}{2} \left(1 - \frac{h}{H}\right)^2, \quad (2.21)$$

where $(1 - \frac{h}{H})^2$ is the modification factor. This result will be used largely below when comparing the turbulence observations to the model of Thomas and Taylor (2010).

So far, only a few studies have tested the above parameterization for the scaling of SI dissipation rate in both numerical and observational approaches (Thomas and Taylor, 2010; D'Asaro et al., 2011; Thomas et al., 2016). It is still unclear how SI-turbulence behaves if B_0 and $B_E < 0$, or if the wind is predominately in the cross-front direction. At the moment, the models ignore SI-induced mixing if $B_0 + B_E \leq 0$, e.g. Bachman et al. (2017).

2.4. Inertial/symmetric instability

Different from the classical view that SI grows at the expense of the background kinetic energy, Grisouard (2018) recently argued that inertial/symmetric instability (denoted

as ISI in the following) may also exchange potential energy between the instability and the background flow in finite-width fronts. The focus of the study by Grisouard (2018) were SBL instabilities growing inside a region with $f q < 0$ and $\zeta/f \approx -1$ on the anticyclonic side of an idealized, finite-width front.

From a series of numerical experiments, three phases of the growth of ISI were identified: (i) during the initial phase, the fastest growing perturbations were aligned with the tilted isopycnals, as theoretically predicted for SI in an unbounded domain; (ii) for finite-width fronts, however, the cross-front velocities associated with the growing instability eventually induced isopycnal displacements and even density overturns, as shown in Figure 5 of Grisouard (2018); (iii) potential energy from the background flow converts into the ageostrophic perturbations, resulting in energy dissipation. This regime, so far, has rarely been investigated in field observations.

2.5. Turbulence parameters

A series of turbulence parameters, describing the characteristics of turbulence and mixing, required to understand the analysis in the following of this thesis, are summarized in the following.

2.5.1. Monin-Obukhov scale

The Classical Monin-Obukhov scale, $L_{MO} = u_*^3 / \kappa B_0$, vertically separates regions of shear-driven turbulence ($z > -|L_{MO}|$) from the deeper parts of the SBL where buoyancy effects become important. The friction velocity, $u_* = \sqrt{|\tau^w| / \rho_0}$, is computed from the wind stress τ^w , and $\kappa = 0.4$ denotes the von Kármán constant. A negative L_{MO} appears when the surface is heated, indicating the SBL is stabilizing, and vice versa for the cooling conditions. Note that at dawn and dusk when the heat flux across zero, L_{MO} becomes infinite.

Considering the effect of the Ekman buoyancy flux B_E in the presence of a front, the impact of surface buoyancy fluxes on SBL turbulence can be quantified with the

help of a modified version of L_{MO} of the form:

$$L_{MO} = \frac{u_*^3}{\kappa(B_0 + B_E)} \quad (2.22)$$

2.5.2. Ozmidov scale

The Ozmidov scale, $L_O = (\varepsilon/N^3)^{1/2}$, approximates the largest size of turbulent overturns in stratified turbulence. Comparing the Ozmidov scale with the wall-layer scale, $l = \kappa|z|$ (with $\kappa = 0.4$) shows if turbulent overturns are limited by stratification or by the presence of the free surface, respectively. E.g., for $L_O > \kappa|z|$, the overturning scales are likely controlled by the proximity of the surface rather than by stratification.

2.5.3. Richardson number

The (gradient) Richardson number, $Ri = N^2/S^2$, with the (square of) the total vertical shear, defined as

$$S^2 = \left(\frac{\partial u}{\partial z}\right)^2 + \left(\frac{\partial v}{\partial z}\right)^2, \quad (2.23)$$

has been widely used as an indicator for shear instability ($Ri < 1/4$). If the Richardson number fluctuates around the critical value for shear instability, the flow is often said to be in a state of “marginal stability”, e.g. Smyth and Moum (2013).

Chapter 3.

Study area, instruments and methods

3.1. Study area: the Benguela upwelling system

The Benguela upwelling system, located in the south-eastern Atlantic Ocean off the Namibian coast, is one of the major upwelling systems of the global ocean. Upwelling in this region is linked to predominantly equatorward winds along the coast, and tends to be governed by strong spatial and temporal variability of the wind field (Risien et al., 2004). A regional overview (Figure 3.1) shows that mesoscale and submesoscale eddies, filaments, and fronts are ubiquitous in the Benguela system, providing an ideal environment for this study.

The focus of this thesis were two distinct filaments: (i) a freshly forming upwelling filament in the vicinity of the Lüderitz upwelling cell, one of the most energetic upwelling hotspots of the Benguela system (Shannon and Nelson, 1996). The filament evolved out of the main upwelling front in a region associated with strong mesoscale activity; (ii) a longer filament with a zonal extent of approximately 300 km off the Namibian coast (black boxes in Figure 3.1a). These experimental sites are located at approximately 14°E, 27°S, and 12°E, 27°S, respectively, with local depths of roughly 400 m and 4000 m, respectively. Note that the filaments in the outer and near-coastal region (Figure 3.1a) will be denoted as “FO” and “FC”, respectively, throughout the entire thesis. Winds were around 10 m s^{-1} , directed equatorward along the coast with little spatial variability, thus providing stable conditions for coastal upwelling. The local inertial period is $T_f = -2\pi/f = 26.5$ hours, where $f = -6.6 \times 10^{-5} \text{ rad s}^{-1}$ is the Coriolis parameter.

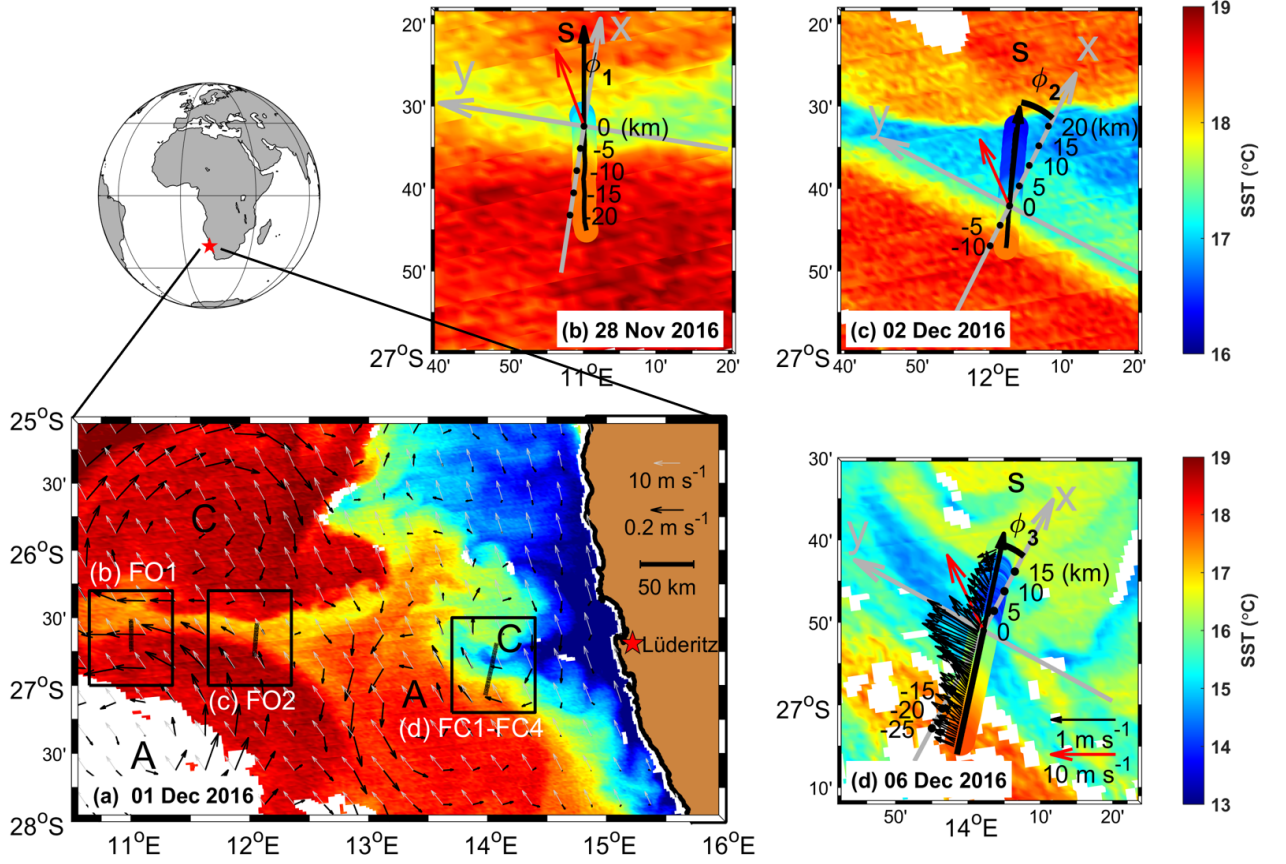


Figure 3.1.: (a) Overview map of the Benguela upwelling system with satellite SST (in color), geostrophic currents calculated from the SSH data (black arrows), and wind field (gray arrows), all from 01 December 2016. The experimental sites (black box) and the main ship transects (black line) are marked. (b) and (c) Expanded view of the study area for Chapter 5 with satellite SST from 28 November 2016 and 02 December 2016, respectively. Also shown are ship-based SST measurements (colored markers) along the ship track of transects FO1 and FO2 (see Table 3.1), respectively. The frontal coordinate system (in gray) is rotated by $\phi_1 = 9^\circ$ and $\phi_2 = 22^\circ$ with respect to the alongtrack direction s for transects FO1 and FO2, respectively. The red arrow indicates the wind speed, averaged over the transect. (d) as (b) and (c) but now for Chapter 4 with satellite SST from 06 December 2016. Additional shown is near-surface velocities (arrows) along the ship track of transect FC3. The frontal coordinate system (in gray) is rotated by $\phi_3 = 16.2^\circ$ with respect to the alongtrack direction s .

The key components of the ship-based observations were high-resolution turbulence microstructure and near-surface velocity measurements, obtained from 28 November to 07 December 2016 during a cruise with R/V *Meteor*. These measurements were carried out on six repeated transects across the filaments, either from continuous “tow-yo” profiling from the slowly cruising ship (transects FO1, FO2, FC3, and FC4) or from

the drifting ship near fixed stations distributed along the transect (transects FC1 and FC2), as summarized in Table 3.1. Transects FC1 - FC4 were acquired across the freshly forming filament on the shelf (Figure 3.1c) while transect FO2 was obtained across filament FO in the outer region (Figure 3.1b). Transect FO1 was measured at the tail of filament FO (westernmost transect in Figure 3.1a) for comparison with transect FO2 as their sea-surface structures were similar.

Table 3.1.: Summary of measurements during the six cross-filament transects. FS: measurements at “fixed stations” along the transect. CS: “continuous” measurements along the transect. The last column indicates the availability of ADCP data from the towed research catamaran, CADC, (data from the vessel-mounted ADCP were always available).

Transect Nr.	Time (UTC)	Type	CADC
FO1	2016-11-28 09:13 – 2016-11-28 17:58	CS	No
FO2	2016-12-02 01:56 – 2016-12-02 10:33	CS	No
FC1	2016-12-04 12:07 – 2016-12-04 17:32	FS	No
FC2	2016-12-05 16:15 – 2016-12-06 04:28	FS	No
FC3	2016-12-06 15:22 – 2016-12-07 01:38	CS	Yes
FC4	2016-12-07 14:47 – 2016-12-07 20:48	CS	No

3.2. Instruments

3.2.1. Turbulence microstructure profiler

Stratification and mixing data were obtained with the help of an MSS90-L turbulence microstructure profiler from ISW (Germany), equipped with two airfoil shear probes for turbulence measurement, a fast-response thermistor, a Seapoint turbidity sensor, and precision CTD sensors from Sea & Sun Technology (Germany). The free-falling profiler was balanced for a sinking speed of 0.6-0.7 m s⁻¹, yielding a 100-m profile every 5-6 minutes. Microstructure profiling was performed in a “tow-yo” mode from the stern of the ship while slowly [speed: 1-2 kn, (1 kn \approx 0.51 m s⁻¹)] cruising against wind and waves. This resulted in an effective horizontal profile spacing of a few hundred meters, depending on ship speed.

Microstructure data, collected at 1024 Hz, were averaged down to 256 Hz for noise reduction before further processing. Data from the CTD sensors were then averaged into 0.1-m vertical bins, and converted into conservative temperature, Θ , and absolute salinity, S_A , according to the international TEOS-10 standard for seawater (Millero et al., 2008; Feistel et al., 2010). The energy dissipation rate, ε , was estimated by integrating shear spectra across the dissipative subrange inside half-overlapping 256-point windows:

$$\varepsilon = \frac{15}{2} \nu \int_{k_1}^{k_2} S(k) dk \quad (3.1)$$

where ν denotes eddy viscosity (typical value: $10^{-6} \text{ m}^2 \text{ s}^{-1}$), $S(k)$ the shear spectra, and k the corresponding wave number. The lower wave number k_1 is fixed at 2 cpm (cycles per meter) suggested by the length of the profiler while the upper wave number k_2 for integration was found iteratively as a function of the Kolmogorov wave number with a correction for lost variance as described in Moum et al. (1995). The noise level is $\varepsilon \approx 10^{-9} \text{ W kg}^{-1}$. These dissipation rate estimates were then averaged into 0.5-m vertical bins. As the upper meters of the water column is likely affected by the presence of the ship, data above 5 m depth are not shown in the following, and data above 10 m are excluded from the analysis.

3.2.2. Velocity measurements

Horizontal velocities were obtained from a vessel-mounted 75-kHz ADCP (RDI Workhorse, Ocean Surveyor), sampling the water column in 8-m vertical bins at 1 Hz. With the uppermost bin located at 17.5 m depth, this instrument was not able to provide velocity data in the important near-surface region, where the core of the frontal jet was located. The ship-based velocity measurements were therefore complemented by data from a downward-looking 300 kHz broad-band ADCP (RDI Workhorse), mounted on a 5.5-m research catamaran that was towed at a distance of 100-150 m behind the ship, in parallel with the microstructure measurements. This instrument sampled the upper part of the water column at 2-s intervals in 2-m vertical bins with the uppermost bin located 4.5 m below the surface. The catamaran was equipped with a remote-controlled rudder, allowing it to be laterally steered out of the ship's wake in order to obtain near-surface velocity data that were undisturbed by ship effects. It turns out

to be a useful tool to investigate near-surface processes as the mixed layer was only a few tens of meters thick in the two study areas.

As acoustic bottom tracking data were not available due to the large water depth, the speed over the ground was estimated based on GPS data that were available independently on both platforms (R/V *Meteor* and the research catamaran). Velocity data from both ADCPs were averaged over intervals of 120 s and rotated into the alongfront and cross-front directions as described below. The data processing for the catamaran-mounted ADCP is described in Appendix B. A comparison of velocity data from both ADCPs in the overlapping depth range between 17.5 m and 73.5 m showed excellent agreement (see Appendix B).

3.2.3. Near-surface CTD measurements

In order to locate upwelling filaments, R/V *Meteor*'s thermosalinograph measurements were monitored closely and combined with information from satellite sea surface temperature data. Alongtrack near-surface temperatures at 10-s intervals were obtained from an SBE38 temperature sensor (SeaBird, USA) mounted at 2 m depth inside the hull of the ship. Near-surface salinity data, provided by a SBE21 thermosalinograph, were corrected based on the near-surface salinity from microstructure data for consistency.

3.2.4. Atmospheric data

A ship-board weather station, operated by the German Weather Service (DWD), provided continuous meteorological data during the entire cruise. These included wind speed and direction, air temperature and pressure, shortwave and longwave radiation, and humidity, all at approximately 35 m height. These data were used to estimate the cross-front and downfront components of the wind stress, τ_x^w and τ_y^w , and the net upward heat flux (or net ocean heat loss) $Q_{net} = Q_{SW} + Q_{LW} + Q_S + Q_L$, using the COARE 3.5 routines (Fairall et al., 2003; Edson et al., 2013). Here, $-Q_{SW}$ is the net downward shortwave radiation, and $Q_{LW} = Q_{LW}^{out} - Q_{LW}^{in}$ the net upward longwave radiation, calculated from the difference between the outgoing longwave radiation, Q_{LW}^{out} , and the observed downward longwave radiation, Q_{LW}^{in} . The former was estimated using the Stefan-Boltzman law (with an emissivity of 0.985), using ship-based

SST measurements (Köhn et al., 2017). The sensible and latent heat losses, Q_S and Q_L , were calculated from the COARE 3.5 bulk formulas.

For the subsequent analysis, the atmospheric buoyancy flux was calculated as $B_0 = \alpha g Q_{net} \rho^{-1} C_p^{-1}$, where α denotes thermal expansion coefficient, g the gravitational acceleration, ρ the density of seawater, and $C_p = 4000$ ($\text{J kg}^{-1} \text{K}^{-1}$) the specific heat of water. Positive B_0 denotes buoyancy loss. The contribution of precipitation to the buoyancy flux was neglected as there was virtually no rainfall during the measurements.

3.2.5. Satellite data

Daily SST data at 1 km resolution, provided by the Ocean Biology Processing Group (OBPG, <http://oceancolor.gsfc.nasa.gov>), and sea surface height anomalies (SSHA) at 25 km resolution, taken from AVISO (<http://www.aviso.altimetry.fr/>), were used for the detection of fronts and filaments (see Appendix A for the accuracy of the SSH data). Infrared SST data were strongly affected by clouds during large parts of the main ship-based transect measurements (02-07 December 2016). However, a virtually cloud-free scene of the entire study area could be obtained just a few days before the main measurements (01 December), as shown in Figure 3.1a. For the wind field, daily ASCAT data with 0.25° grid resolution from the Asia-Pacific Data-Research Center (<http://apdrc.soest.hawaii.edu/>) were used.

3.3. Methods

3.3.1. Front-based coordinate system

For the subsequent analysis, rotated coordinate systems were introduced for each of the cross-front transects with the cross-front and alongfront directions denoted as x and y , respectively, as indicated in Figure 3.1b, c, and d. For filament FO, the coordinate system for transects FO1 and FO2 were chosen such that the alongfront direction was aligned with the southern front, as suggested by the available SST data (Figure 3.1b and c). This resulted in an angle of 81° and 63° between the x -axis and the East direction for transects FO1 and FO2, respectively. This implies $\phi_1 = 9^\circ$ and

$\phi_2 = 22^\circ$ for the angle between the x -axis and the alongtrack direction s for transects FO1 and FO2, respectively (Figure 3.1b and c). For filament FC, a large offset between satellite and ship-board measurements from the transect FC3 (see Table 3.1) makes the front-based coordinate system difficult to define based on SST data alone. Alternatively, near-surface velocities along the main transect FC3 (Figure 3.1d) shows a remarkably strong frontal jet associated with the south-western front with near-surface velocities exceeding 1 m s^{-1} . The alongfront direction y was therefore aligned with the frontal jet, based on near-surface velocities along the main transect FC3. This resulted in an angle of 61.3° between the x -axis and the East direction and thus, $\phi_3 = 16.2^\circ$ for the angle between the x -axis and the alongtrack direction s (Figure 3.1d).

For all the coordinate systems, the origin of the cross-front coordinate, $x = 0$, is collocated with the maximum cross-front density gradient at the surface. All data measured along the ship track were projected onto their cross-front coordinate x , assuming homogeneity in the y -direction. Similarly, gradients along the ship track were converted into cross-front gradients using the relation $\partial/\partial s = \cos \phi \partial/\partial x$. Vectorial quantities pointing into the cross- and alongfront directions are denoted by the subscripts x and y , respectively, except for the cross-front and alongfront current speeds that are referred to as u and v .

3.3.2. Data averaging procedure

To investigate the stability properties and turbulence of the two filaments, the region-averaged cross- and alongfront velocities \bar{u} and \bar{v} were computed by averaging the raw (catamaran-based) velocity profiles at 2-m vertical resolution over each of the selected regions, respectively (see Figure 4.4d and Figure 5.6d). Similarly, region-averaged density profiles were computed at 0.1-m vertical resolution, based on the available microstructure casts inside these regions. These profiles were vertically filtered with a centered 2-m box filter to obtain representative density, $\bar{\rho}$, and buoyancy, \bar{b} , profiles at a resolution comparable to the velocity data. This becomes important when vertical density and velocity gradients are quantitatively compared, e.g. in terms of non-dimensional parameters like the gradient Richardson number $Ri = N^2/S^2$ (see Section 2.5.3).

From these region-averaged profiles, the (squares of) the total vertical shear,

$$S^2 = \left(\frac{\partial \bar{u}}{\partial z} \right)^2 + \left(\frac{\partial \bar{v}}{\partial z} \right)^2, \quad (3.2)$$

and the buoyancy frequency, $N^2 = \partial \bar{b} / \partial z$, by vertical finite differencing. The region-averaged vertical vorticity, $\zeta = \partial \bar{v} / \partial x$, and cross-front buoyancy gradient, $M^2 = -\partial \bar{b} / \partial x$, were computed from averaging the cross-front gradients over each of the selected subregions, respectively (e.g. Figure 4.4d)

Chapter 4.

Frontal instability and energy dissipation under destabilizing surface forcing

This chapter is focused on frontal instability and associated turbulence in the upwelling filament FC in the near-coastal region under destabilizing surface forcing. Highlights from the transects FC1 - FC4 (see Figure 3.1a,d) corresponding to this filament will be presented in the following. Parts of the results presented here are already published in the *Journal of Physical Oceanography* in an article entitled “Frontal instability and energy dissipation in a submesoscale upwelling filament” (Peng et al., 2020). My contributions included: (i) the development of the general paper strategy, (ii) the entire data analysis, (iii) the design and generation of all figures, and (iv) the writing of the initial version of the manuscript. Findings from other studies are clearly marked and referred to. There is no conflicting interest with the co-authors of the above mentioned publication.

4.1. Filament evolution and structure

The spatial evolution of filament FC for the period 28 November - 07 December 2016 is shown in Figure 4.1. These satellite-based observations were complemented by four cross-filament transects (FC1-FC4, see Table 3.1) that were obtained on 04-07 December 2016, as shown in Figure 4.2. All these transects exactly followed the along-track coordinate s shown in Figure 3.1d, although with different start and end points, re-

spectively. Data measured along the ship track were then projected onto the cross-front direction x as described in Section 3.3.1. Note that the local coordinate system, based on transect FC3 (Figure 3.1d), remains fixed for all four transects to more clearly illustrate the relative motion of the front.

Based on the spatial pattern and vertical isopycnal structure of the filament, the entire evolutionary process was divided into three stages: 28 November - 04 December (formation stage), 05-06 December (mature stage), and 07 December (decay stage).

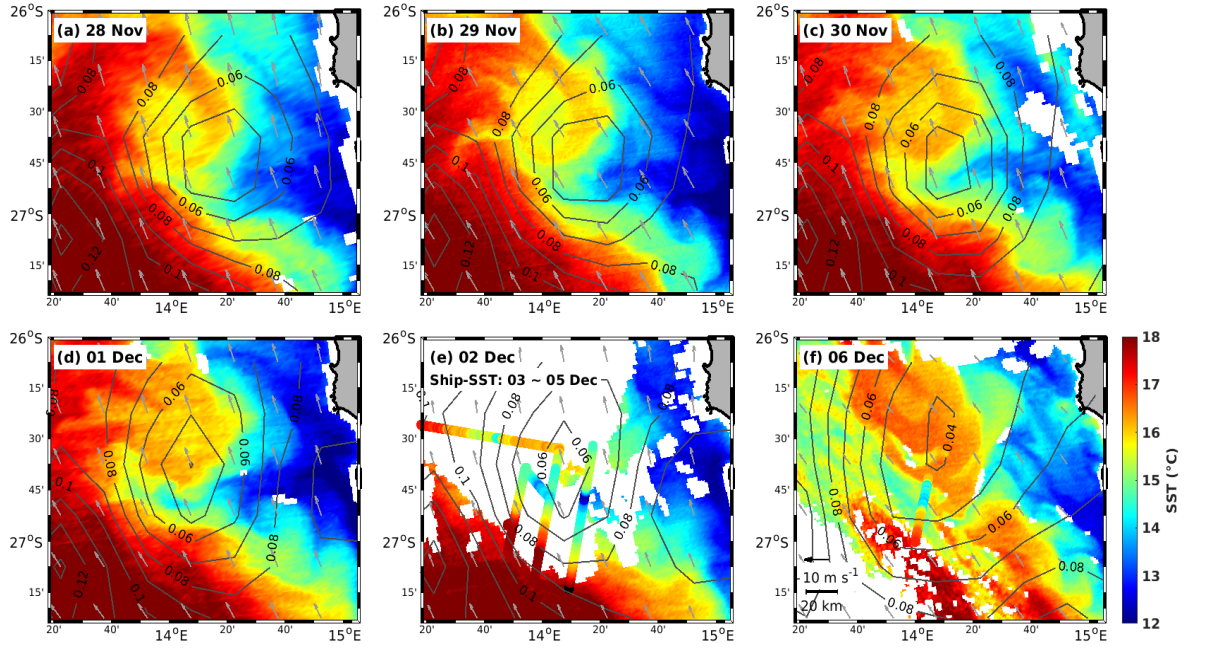


Figure 4.1.: Sequence of satellite-based SST snapshots (all obtained around midday), SSHA (black contour lines at 0.01 m intervals), and surface wind field (vector scale in panel f) from 28 November to 6 December 2016. Panels (e) and (f) include SST measurements along the ship track, obtained on 03-06 December. The figure is taken from Peng et al. (2020).

4.1.1. Formation stage

Figure 3.1a suggests that the formation and evolution of the filament may be linked to the interaction of two mesoscale eddies (anticyclonic and cyclonic, marked as “A” and “C” in the figure) with the main upwelling front. This becomes clearer from the enlarged view in Figure 4.1a-d, showing that these two eddies induced a confluent strain field, locally deforming the main upwelling front by entraining a filament of

30 Frontal instability and energy dissipation under destabilizing surface forcing

cold waters from the coastal upwelling cell. During the days from 28 November to 01 December, the filament intensified and was entrained further westward into the warm waters outside the upwelling region. This process is consistent with the classical view of frontogenesis due to a mesoscale strain field (Hoskins, 1982) that has been shown to dominate the initial phase of filament generation and intensification also in high-resolution simulations (e.g., Capet et al., 2008; Gula et al., 2014).

The evolution of the vertical structure of the filament during this period is shown in Figure 4.2. The short transect FC1 (Figure 4.2a,b), observed on 04 December, only covered the frontal region bounding the filament in the south-west (SW in the following). Outcropping isopycnals in this region bridged a lateral density contrast of approximately 0.6 kg m^{-3} , which was largely due to temperature differences that were only to a small extent compensated by salinity effects (the upwelled water inside the filament is slightly fresher). Near-surface thermosalinograph measurements at high spatial resolution show smooth temperature and salinity transitions across the entire transect with no indications for locally intensified, sharp fronts. This suggests that, in this case, lateral gradients in the near-surface region were well resolved even with the coarse-resolution station measurements of this study. On the SW side of the front ($x < -5 \text{ km}$, approximately), a well-defined SBL, bounded by a sharp thermocline at 50 m depth, can be identified. This layer showed indications for a reduction of vertical stratification towards the surface but was nowhere “well-mixed” except close to the surface at the SW end of the transect. Thermocline isopycnals outcrop within $-5 < x < 5 \text{ km}$, which was reflected in an intensification of the cross-front buoyancy gradient at the surface.

4.1.2. Mature stage

From 02 December onwards, cloud cover increased, and useful satellite images became rare. The last available snapshot before the start of the ship-based measurements is from 02 December, providing SST data only in the southern and eastern parts of the domain. Combined with the high-resolution thermosalinograph observations along the cruise track (03-05 December), these data nevertheless show that the filament remained a stable feature until 05 December (Figure 4.1e).

The longer transect FC2 (05 December) shows a picture on the SW side of the transect that is similar to the transect FC1, but now reveals that the filament merges

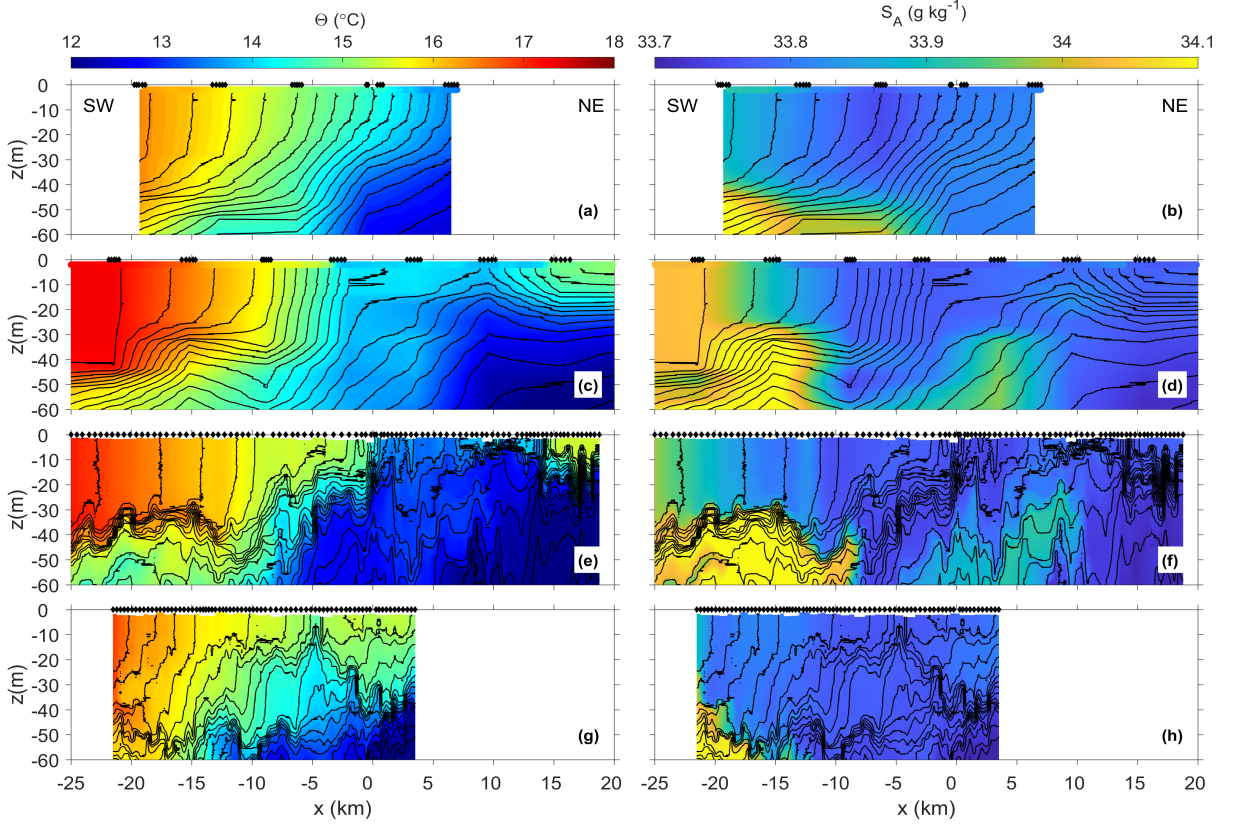


Figure 4.2.: Cross-filament variability of temperature (left column) and salinity (right column) for transects FC1-FC4 on 04-07 December 2016, as summarized in Table 3.1. Positions of individual microstructure casts are indicated at the top of each panel, respectively. The low-resolution transects FC1 and FC2 contain additional near-surface temperature and salinity data based on high-resolution thermosalinograph measurements at 2 m depth (colored markers). Black lines denote isopycnals (potential density) at intervals of 0.05 kg ^{-3} . The figure is taken from Peng et al. (2020).

into a second, shallower front at the north-east (NE) end (Figure 4.2c,d). The high-resolution thermosalinograph data show that smooth cross-front density gradients found in transect FC1 have now evolved into a sharp front at $x = -3 \text{ km}$. Another front at the NE end of the filament (near $x = 14 \text{ km}$), is also observed. Clearly, the horizontal structure of these sharp fronts was not resolved by the coarse-resolution microstructure stations.

The advantage of the high-resolution observations becomes evident for the main transect FC3 (06 December, Figure 4.2e,f), which is based on continuously repeated microstructure profiling with a horizontal spacing of a few hundred meters only. While the large-scale structure of the filament in FC3 is comparable to FC2, the high-resolution

32 Frontal instability and energy dissipation under destabilizing surface forcing

data for FC3 reveal a wealth of additional small-scale features. Most importantly, these data resolve two sharp fronts on either side of the filament, and reveal a strong asymmetry in mixed-layer depths, with a shallow (less than 20 m deep) mixed layer on the NE side, and a more than 35 m deep mixed layer on the SW side. This asymmetry of the filament differs from the symmetric filaments that were previously studied in the idealized simulations (Gula et al., 2014; McWilliams, 2016). Surface forcing plays a major role in this regard (see Section 4.3). Additionally, indications for internal-wave motions inside and below the thermocline were observed throughout the transect.

4.1.3. Decay stage

Finally, on 06 December, SSHA data show first indications for a disintegration of the cyclonic eddy in the center of the domain, and an associated collapse of the eastern end of the filament, resulting from the advection of warm fluid patches into the transition region between the filament and the main upwelling cell (Figure 4.1f). It is important to note, however, that the sharp front bounding the filament from the SW remained remarkably robust until 06 December, and did not show indications for meandering or other strong distortions in the vicinity of the main transect FC3 (Figure 3.1b). The following transect FC4, sampled on 07 December (Figure 4.2g,h), shows the collapse of the filament. This is consistent with Figure 4.1f, in which indications for the beginning disintegration of the eastern part of the filament became evident already a day before.

4.2. Atmospheric forcing

Figure 4.3 shows the temporal variability of the atmospheric forcing shortly before and during the ship-based measurements along transects FC1-FC4. With an average around 0.4 Pa, the wind stress was strongest during transect FC1, and decayed to approximately half this value during the main transect FC3 (Figure 4.3a). The down-front component of the wind stress, τ_y^w , was positive throughout the measurements, and generally dominated the total wind stress, except for transect FC2, when winds were comparatively weak, however. This suggests that the SW front of the filament was characterized by destabilizing Ekman transports (dense water is moved on top of light water) while the NE front was permanently stabilized, as discussed in greater detail below.

The surface buoyancy flux B_0 (positive upward, i.e. positive for buoyancy loss, as defined in Section 3.2.4) shows a clear diurnal signal peaking at approximately $B_0 = -4 \times 10^{-7} \text{ m}^2 \text{ s}^{-3}$ around midday due to strong solar heating (Figure 4.3b). During nighttime, atmospheric cooling induced a buoyancy loss that was typically in the range $B_0 = 4 - 6 \times 10^{-8} \text{ m}^2 \text{ s}^{-3}$. This diurnal cycle was imprinted on the ship transects, depending on their relative timing. Transect FC1 was exposed to strong daytime heating (buoyancy gain), while FC2 was affected by only weak atmospheric heat fluxes with a slight cooling tendency. The main transect FC3 was characterized by a transition from late-afternoon weak diurnal warming to nighttime cooling just when R/V Meteor crossed the SW front on its way from the cold filament to the warm ambient waters further offshore.

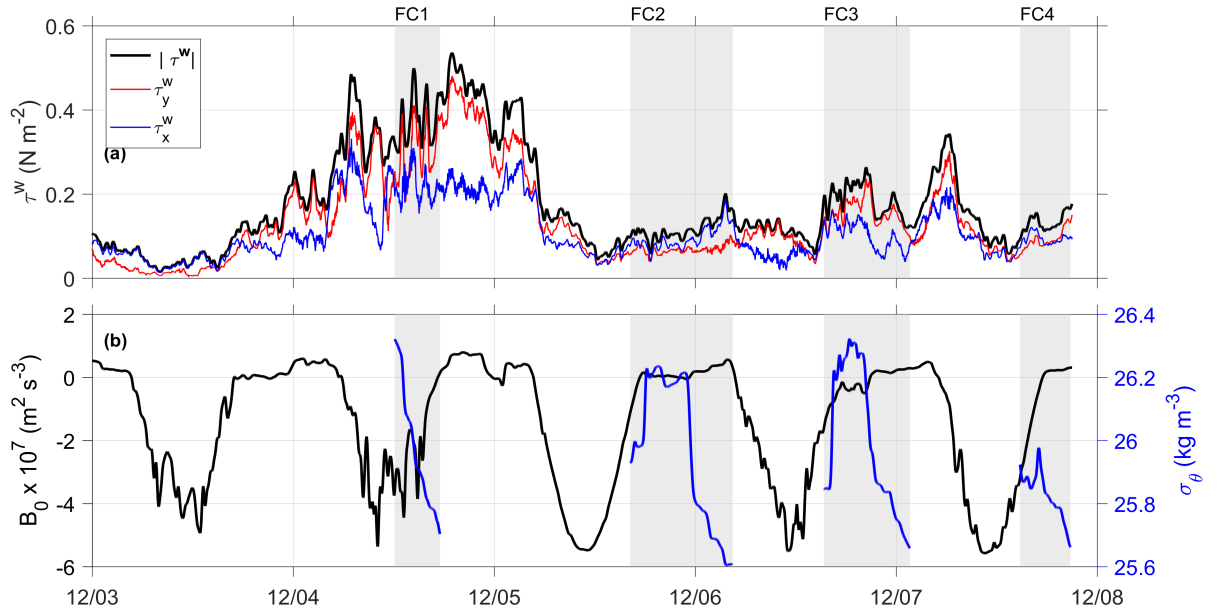


Figure 4.3.: Time series of (a) wind stress magnitude and cross-front, τ_x^w , and downfront, τ_y^w , components; and (b) net upward buoyancy flux (positive for buoyancy loss) B_0 before and during the transect measurements. The surface density observed along the cross-filament transects FC1-FC4 is shown in blue color in (b). Note that the decomposition into cross-front and downfront components in (a) is based on the orientation of the front during transect FC3 (see Figure 3.1d). The figure is taken from Peng et al. (2020).

4.3. Frontal structure and stability regime classification

Motivated by the robustness of the sharp front bounding filament FC3 in the SW during the measurements, the availability of both very high-resolution microstructure and undisturbed near-surface velocity data from the research catamaran, and conditions favorable for FSI due to downfront winds, the vertical structure of this sharp front will be discussed in more detail in the following.

4.3.1. Frontal structure

Figure 4.4 shows that the strongest horizontal buoyancy gradients (up to $M^2 = 2 \times 10^{-6} \text{ s}^{-2}$, as defined in Section 2.2) were found inside a narrow region with outcropping isopycnals ($-2 \text{ km} < x < 2 \text{ km}$), where the frontal jet induces downfront velocities of up to 1 m s^{-1} . Further SW ($x < -10 \text{ km}$), the main front merges into a 30-35 m deep SBL with weak stratification and strong turbulence. Here, horizontal buoyancy gradients were substantially smaller compared to the main front but still of the order of few times 10^{-7} s^{-2} . For comparison, Taylor and Ferrari (2010) used $M^2 = 2.1 - 8.5 \times 10^{-7} \text{ s}^{-2}$ in their simulations of turbulent SBL fronts, noting that their intermediate value ($M^2 = 4.2 \times 10^{-7} \text{ s}^{-2}$) “represents a relatively strong front”. Also, their SBL depths were similar to the observations presented in this thesis.

The downfront wind stress τ_y^w was relatively constant along the transect, and the Ekman buoyancy flux B_E defined in (2.6) thus largely traces the variability of the horizontal buoyancy gradient (Figure 4.4a). The total buoyancy flux, $B_0 + B_E$, was positive throughout the frontal region, providing favorable conditions for FSI (see Section 2.3). Note that due to the strength of the cross-front buoyancy gradients, and weak to negligible solar radiation during the transect (late afternoon and nighttime), we generally have $B_0/B_E \ll 1$ (red and black curves in Figure 4.4a). It is noteworthy that a negative B_E due to downfront winds is expected on the NE front of the filament. Thus, the two fronts bounding the filament exhibited a marked asymmetry in mixing-layer depth, likely resulting from the stabilizing or destabilizing Ekman transports on the two sides of the filament.

On the SW side of the transect ($x < -10 \text{ km}$), i.e. outside the main frontal region, a weakly stratified SBL can be discerned with turbulence reaching down to the upper edge of the thermocline at 30-35 m depth (Figure 4.4c). This is contrasted by the

frontal region ($-2 \text{ km} < x < 2 \text{ km}$), which is seen to be vigorously turbulent down to 25 m, however, without any indications for a well-mixed SBL.

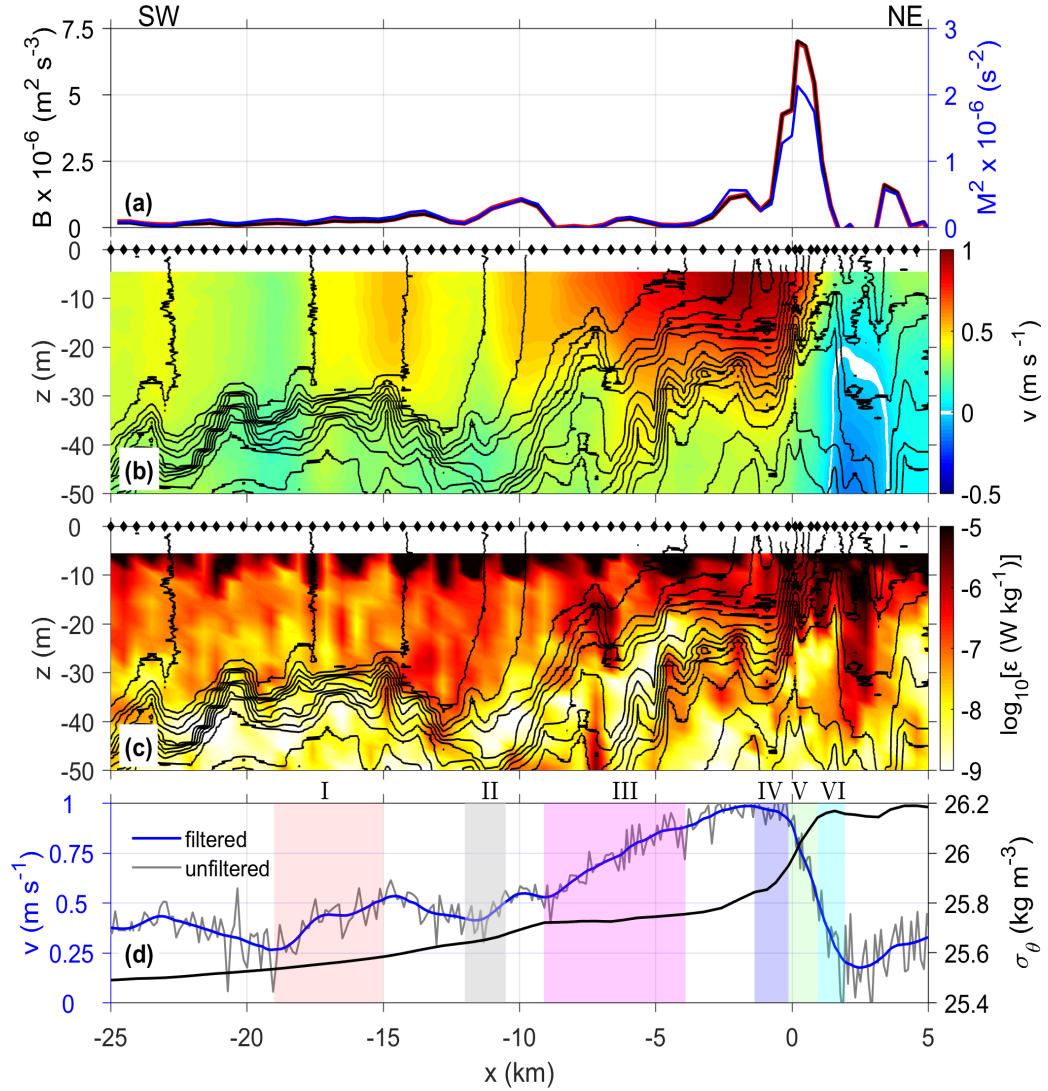


Figure 4.4.: Cross-front variability for transect FC3: (a) Ekman buoyancy flux (black), total buoyancy flux (red), and cross-front buoyancy gradient (blue); (b) downfront velocity; and (c) turbulence dissipation rate. Black contour lines in (b) and (c) denote isopycnals at 0.05 kg m^{-3} intervals; black markers indicate locations of individual microstructure casts. Panel (d) shows the catamaran-based near-surface velocity (in blue, unfiltered raw data in gray) and density (black) at 4.5 m depth. The color-shaded areas indicate selected regions used for the stability analysis. The figure is modified from Peng et al. (2020).

4.3.2. Stability regime classification

For the subsequent analysis, six subregions were identified (see Figure 4.4d), characterized by distinct dynamics and structure, respectively. As discussed in more detail below, each of these regions represents a different stability regime. The key parameters for each region are summarized in Table 4.1.

Table 4.1.: Averaged parameters for regions I-VI, including the cross-front buoyancy gradient M^2 and the total buoyancy flux $B_0 + B_E$ (both based on thermosalinograph data at 2 m depth), and the Rossby number ζ/f (computed from catamaran-based velocity measurements at 4.5 m depth), the low PV layer depth H , the convective layer depth h , and Monin-Obukhov length L_{MO} .

Region	M^2 (s^{-2})	$B_0 + B_E$ ($m^2 s^{-3}$)	ζ/f	H (m)	h (m)	L_{MO} (m)
I	1.19×10^{-7}	2.05×10^{-7}	-1.00	27.5	18.5	15.8
II	2.62×10^{-7}	6.65×10^{-7}	-1.36	32.0	14.8	9.8
III	3.92×10^{-8}	1.00×10^{-7}	-0.67	–	–	–
IV	6.51×10^{-7}	2.17×10^{-6}	0.90	17.5	7.0	3.6
V	1.74×10^{-6}	5.54×10^{-6}	4.80	–	–	1.6
VI	2.63×10^{-7}	7.09×10^{-7}	2.27	–	–	12

Regions I and II are both located on the SW part of the transect, characterized by deep mixed layers and moderate horizontal density gradients. While the well-mixed layer for region I reached down to the thermocline, region II can be vertically separated into a well-mixed surface region, and a deeper layer with significant stratification (see isopycnal structure in Figure 4.4b,c) that is reminiscent of the structure in the numerical simulations described in Taylor and Ferrari (2010). Also the mixing layer depth, the horizontal buoyancy gradient M^2 , and the buoyancy forcing $B_0 + B_E$ (see Table 4.1) are within the parameter range investigated by Taylor and Ferrari (2010), suggesting that region II provides a direct benchmark for their numerical study.

Region III is located inside the anticyclonic flank of the frontal jet (Figure 4.4d), characterized by Rossby numbers $\zeta/f \approx -1$, and relatively weak $B_0 + B_E$ and small M^2 (1-2 orders of magnitude smaller compared to the other selected subregions). This situation is similar to the numerical experiments designed by Grisouard (2018), which were focusing on SBL instabilities growing inside a region on the anticyclonic side of

an idealized, finite-width front. This regime, rarely investigated in field observations so far, will be discussed in depth below.

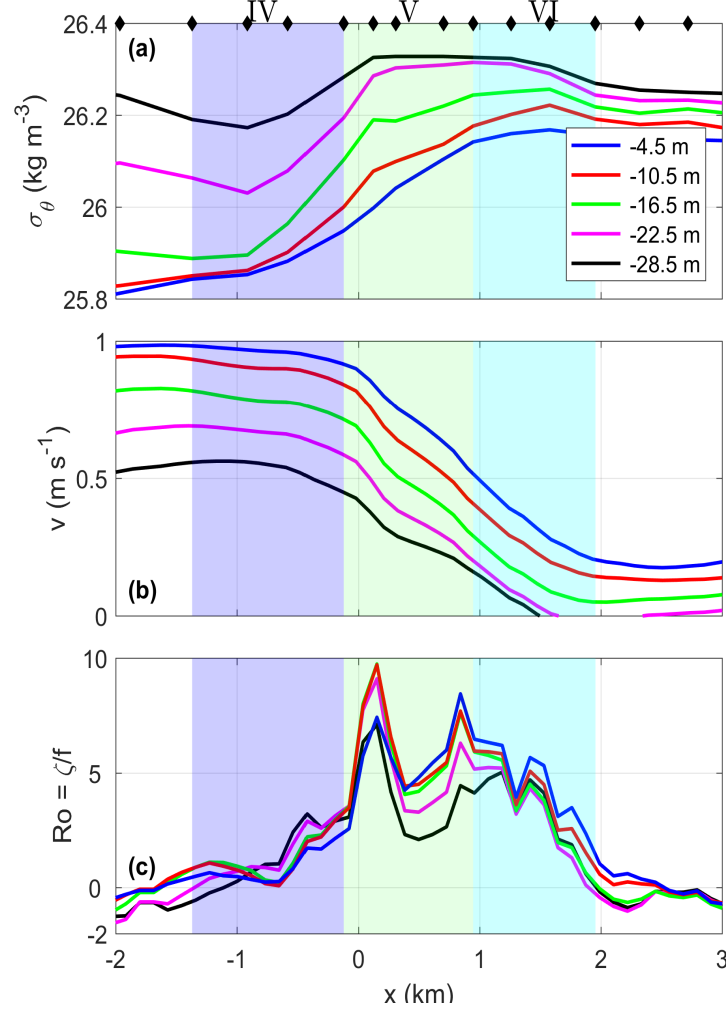


Figure 4.5.: Enlarged view of (a) density, (b) velocity, and (c) Rossby number at different depth levels for subregions IV, V, and VI (see Figure 4.4d). Black markers indicate locations of individual microstructure casts. These data were horizontally filtered with a 2-km box filter, which was found to effectively remove random fluctuations in the raw velocity data without significantly damping the mean frontal velocity gradients (see Figure 4.4d). The figure is taken from Peng et al. (2020).

Regions IV, V, and VI are located in the main frontal zone where the horizontal density gradient and the frontal jet reach their maximum strength, respectively (Figure 4.4d). The distinction between these regions becomes clearer from the enlarged view of the density and velocity structure inside the frontal region in Figure 4.5. Most of the cross-front density gradient in the near-surface region ($z > -20$ m, approximately) was found in regions IV and V, while most of the cross-front (cyclonic) shear

was confined to regions V and VI. Recalling the competing roles of cyclonic shear and baroclinicity with regard to SI according to (2.2), the classification of regions IV-VI thus reflects the following physical regimes: strong baroclinicity and weak vorticity (region IV), strong baroclinicity and strong cyclonic vorticity (region V), and weak baroclinicity and strong cyclonic vorticity (region VI). This distinction is also mirrored in the results of the stability analysis as shown in the next section. It is important to note that despite the small width of the frontal regions IV-VI [$\mathcal{O}(1 \text{ km})$], and different from most previous studies, horizontal gradients were well resolved by the velocity and microstructure measurements in this study.

4.4. Analysis of frontal instability and turbulence

In this section, the theory and methods outlined in Chapter 2 and Section 3.3.2, respectively, are applied to investigate the stability properties of regions I-VI.

4.4.1. Regions I and II: Deep mixing layers

Regions I and II are located SW of the main frontal region, on the warm side of the front (Figure 4.4d), where mixed layers were deep and both atmospheric and Ekman buoyancy forcing were destabilizing during nighttime conditions ($B_0 + B_E > 0$, see Table 4.1). Individual potential density profiles in the SBL exhibit extended regions with unstable stratification, indicating convective mixing. These unstable regions were less clearly reflected in the region-averaged N^2 (Figure 4.6c,d), which was often dominated by a few stably stratified patches in the same depth range. Still, however, the averaged stratification in the near-surface region was very small [$N^2 = \mathcal{O}(10^{-7} - 10^{-6} \text{ s}^{-2})$], and depth intervals with $N^2 < 0$ (circle markers) can be found in both regions even after the averaging procedure.

For region II (Figure 4.6), the thickness of this weakly/unstably stratified near-surface layer was in good agreement with the predicted convective layer depth $h = 14.8 \text{ m}$ (gray dashed line in Figure 4.6d), computed from (2.7) according to the model by Taylor and Ferrari (2010). For $z < -h$, gradually increasing stable stratification was observed, and the Ozmidov scale L_O started to control the size of the turbulent overturns (red line in Figure 4.7d). Most importantly, however, Figure 4.7b shows that this stably stratified but vigorously turbulent layer below the unstratified near-surface

region was characterized by $f q < 0$ and $f q_\zeta > 0$, indicating conditions favorable for FSI down to a depth of $z = -H = -32$ m. The destabilizing baroclinic term q_{bc} dominates the total PV in the stability condition (2.2), and outweighs the slightly cyclonic, hence stabilizing, vertical component q_ζ . Figure 4.6b shows that the velocity difference between the bottom of the low-PV layer and the convective layer was largely geostrophically balanced, although local deviations from a perfect geostrophic balance can be discerned. The conditions for FSI (Taylor and Ferrari, 2010) were thus satisfied in an approximately 17 m thick lower layer in the range $-H < z < -h$. It is worth noting that the parameter space, the vertical scales, and the geometry with a forced SI layer underneath a directly forced convective layer are similar to the numerical simulations of mixed layer fronts by Taylor and Ferrari (2010).

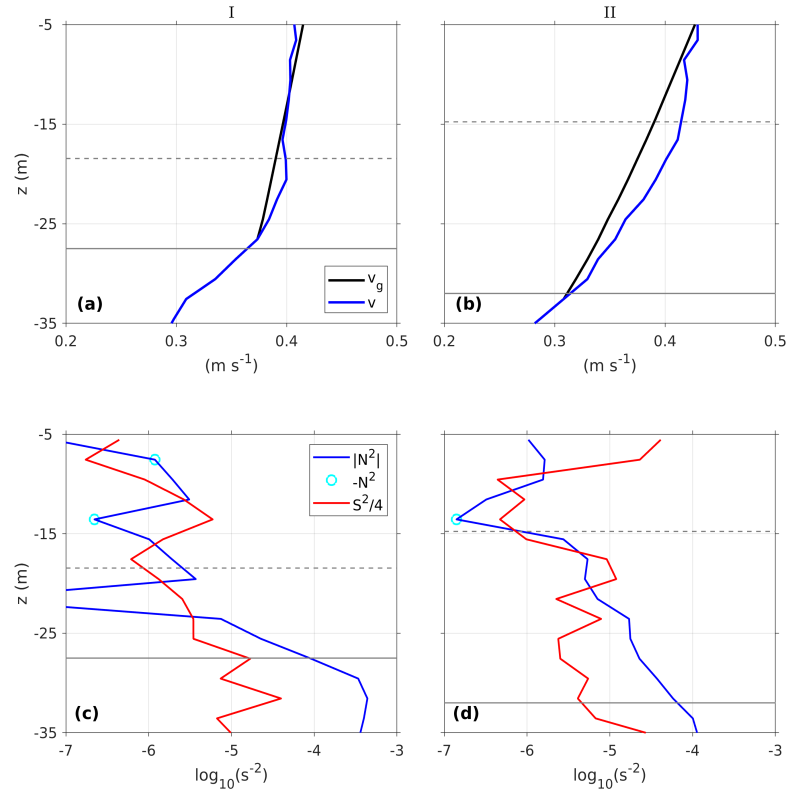


Figure 4.6.: Upper row: geostrophic and observed downfront velocities for (a) subregion I and (b) subregion II. The geostrophic velocity v_g was computed from integrating the observed thermal wind shear $\partial v_g / \partial z = -M^2 / f$ from the bottom of the low-PV layer to the surface. Lower row: squares of total vertical shear and buoyancy frequency for (c) subregion I and (d) subregion II. Note that the shear squared has been divided by a factor of 4 to ease comparison with the critical Richardson number ($Ri = 1/4$). Gray dashed and solid lines denote the convective layer depth h and the low PV layer depth H , respectively. The figure is taken from Peng et al. (2020).

40 Frontal instability and energy dissipation under destabilizing surface forcing

Figure 4.7b shows that the dissipation rates inside the forced SI layer ($-H < z < -h$) slightly decreased with depth with an average value of $\varepsilon = 1.6 \times 10^{-7} \text{ W kg}^{-1}$. As discussed in Section 2.2b, the model of Thomas and Taylor (2010) predicts $\varepsilon_{SI} = (B_0 + B_E)(1 - h/H)^2/2$ for the average dissipation rate inside the forced SI layer. From the values in Table 4.1, the dissipation rate due to FSI is $\varepsilon_{SI} = 1.0 \times 10^{-7} \text{ W kg}^{-1}$. This is within a factor of 2 of the observed value, supporting the hypothesis that FSI was the main energy source for turbulence in this region. As noted by Thomas and Taylor (2010), however, the vertical scales of SI were too large to be directly associated with turbulence dissipation at centimeter scales. Numerical simulations by Taylor and Ferrari (2009) have shown that SI only mediates the energy transfer to scales that become amenable to vertical shear instability, which ultimately triggers small-scale turbulence and energy dissipation.

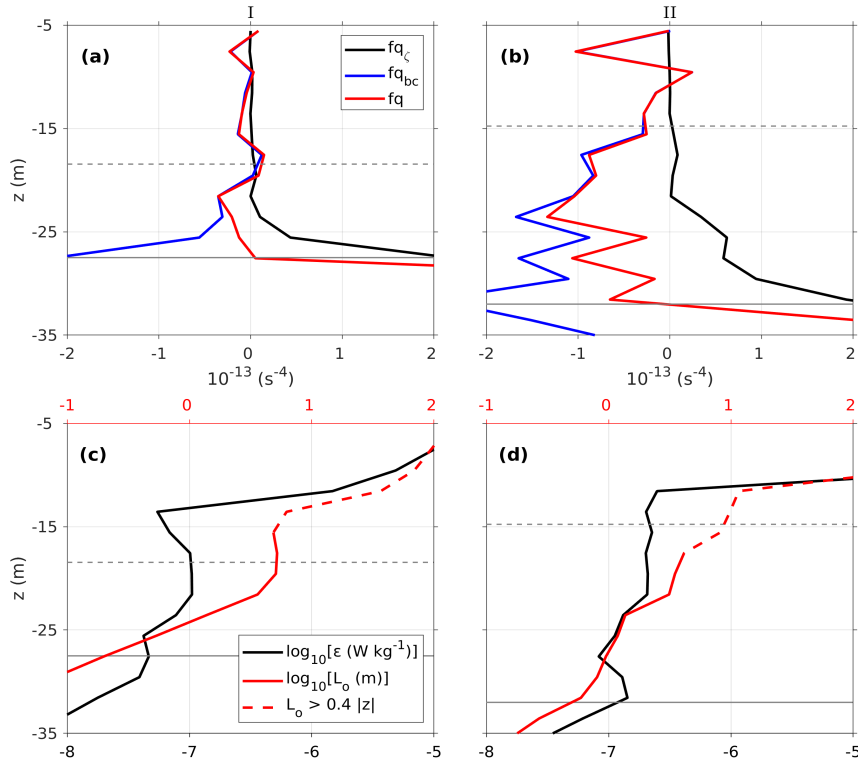


Figure 4.7.: Upper row: vertical, baroclinic, and total PV as defined in (2.2) and (2.5) for (a) subregion I and (b) subregion II. Lower row: turbulence dissipation rate and Ozmidov length (both plotted on a logarithmic scale) for (c) subregion I and (d) subregion II. Dashed red lines indicate regions where the Ozmidov scale is larger than the wall length scale, $L_O > \kappa z$. Gray dashed and solid lines denote the convective layer depth, h , and the low PV layer depth, H , respectively. The figure is taken from Peng et al. (2020).

With the limited vertical resolution (2-m) of the catamaran-based shear measurements, it is unclear to what extent the vertical scales of these secondary shear-instabilities were resolved. Nevertheless, Figure 4.6d shows that the local Richardson number $Ri = N^2/S^2$ was favorable for shear instability ($Ri < 1/4$) in the upper part of the forced SI layer, while it approached larger values of order one in the deeper parts.

In region I, the well-mixed/unstably stratified surface layer was significantly deeper compared to region II, and persistent stable stratification was observed only below approximately 23 m depth (Figure 4.6c). The model of Taylor and Ferrari (2010) in (2.7) yields $h = 18.5$ m from the values in Table 4.1, and therefore underpredicts the observed value by approximately 20%. Figure 4.7a shows that the PV in region I was generally much closer to zero compared to region II but nevertheless reveals a layer with negative $f q$ and positive $f q_\zeta$ down a depth of approximately $H = 27.5$ m. This leaves room for a less than 5 m thick turbulent layer between 23 m and 27.5 m depth, where strong turbulence coincides with significant stable stratification, and conditions were favorable for SI. Overall, however, the evidence for FSI is less clear compared to region II.

4.4.2. Region III: Effect of anticyclonic vorticity

Region III is located inside the anticyclonic flank of the frontal jet (Figure 4.4d). As shown in Figure 4.8b, the central part of this region satisfied the condition for instability ($f q < 0$, see pink contour lines) and contained extended areas with $\zeta/f < -1$ (blue shading), indicating that the flow was unstable with respect to ISI. This is supported by Figure 4.8c, showing a layered structure of the cross-front velocity that is in many respects similar to that found in the simulations (Grisouard, 2018, see their Figures 4 and 8). Consistent with the structure of the cross-front velocity field are pycnostads and local density overturns at the edge of the unstable region (near $x = -7$ km), similar to those visible in Figure 5 of Grisouard (2018). Figure 4.8a shows that these overturns are associated with strongly enhanced energy dissipation, implying an exchange of potential energy between the instability and the background flow, which is different from the classical view that SI grows at the expense of the background kinetic energy, as recently suggested by Grisouard (2018). This also suggests that ISI provides a direct pathway for the down-scale transport of large-scale *potential* energy towards small-scale turbulence and dissipation.

42 Frontal instability and energy dissipation under destabilizing surface forcing

ISI prevents Rossby numbers larger than $\zeta/f \approx -1$ on the anticyclonic side of the front, whereas the cyclonic side remains stable with respect to SI even for $\zeta/f \gg 1$ due to the damping effect of large cyclonic vorticity. This result may help to explain the striking asymmetry in the distribution of cyclonic and anticyclonic vorticity in frontal regions, for which various processes have been suggested (McWilliams, 2016).

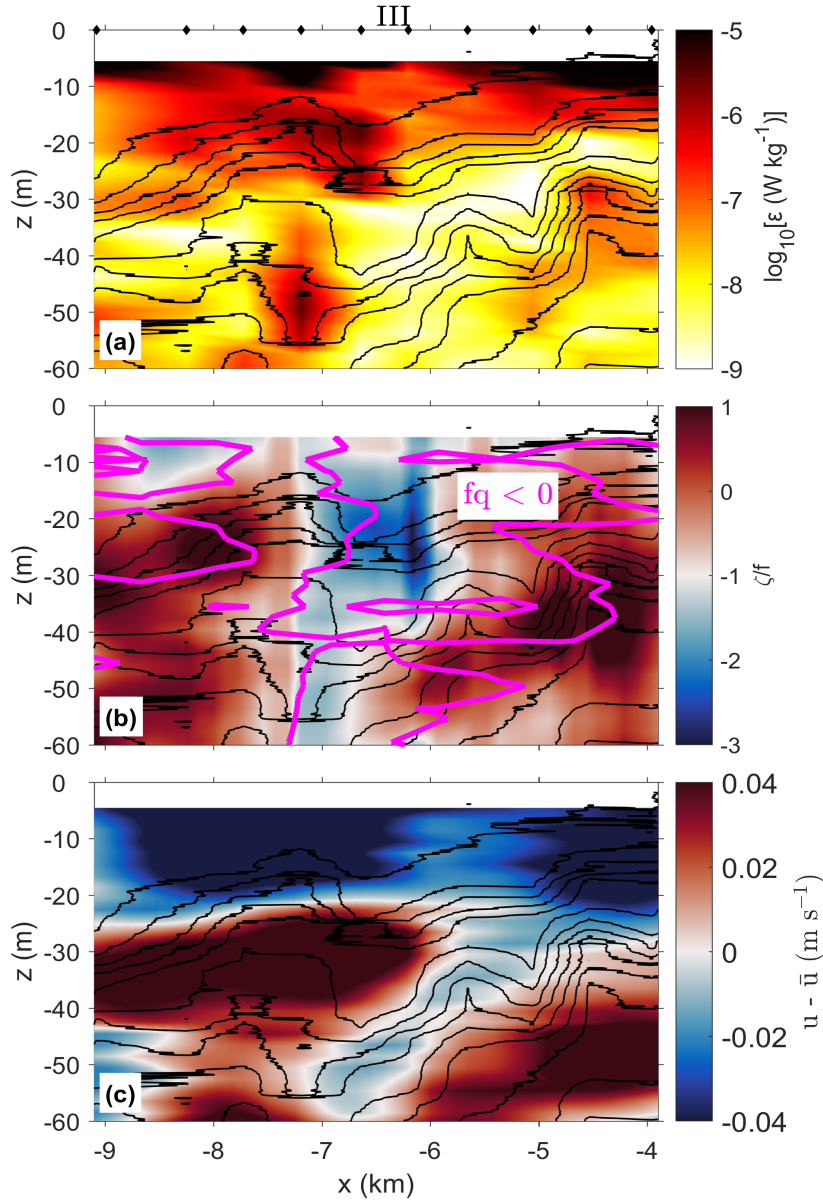


Figure 4.8.: Cross-front variability for region III: (a) turbulence dissipation rate; (b) Rossby number with unstable flow region ($f q < 0$, contour lines in magenta) ; (c) deviation of the cross-front velocity u from the vertical average \bar{u} . Black contour lines in each figure denote isopycnals at 0.05 kg m^{-3} intervals; black markers at the top of panel (a) indicate locations of individual microstructure casts. The figure is taken from Peng et al. (2020).

4.4.3. Regions IV-VI: Main frontal region

The averaging procedure (Section 3.3.2) was also conducted for regions IV, V, and VI to determine the stability characteristics of the main frontal region around $-2 \text{ km} < x < 2 \text{ km}$. As discussed in the context of Figure 4.5, region IV is located in a zone with large M^2 but relatively small cyclonic vorticity with an average Rossby number, ζ/f , close to 1 (Table 4.1). This is reflected in the vertical and baroclinic contributions to the total PV (Figure 4.10a), showing a clear dominance of the destabilizing baroclinic component, q_{bc} , over the stabilizing vertical contribution, q_ζ . The resulting layer with negative $f q$ has a thickness of $H = 17.5 \text{ m}$, substantially larger than the thickness $h = 7 \text{ m}$ of the directly forced near-surface layer computed from (2.7). In contrast to regions I and II, the existence of unstable stratification cannot be directly confirmed here as measurements in the upper few meters are unreliable due to ship effects. Nevertheless, Figure 4.9d does show a strong increase of N^2 below $z = -h$, and Table 4.1 suggests that the buoyancy forcing $B_0 + B_E$ was approximately twice the value of region II, such that gravitationally unstable stratification near the surface may be expected.

The forced SI layer ($z < -h$) in region IV was largely geostrophically balanced (Figure 4.9a) and strongly turbulent with $L_O = \mathcal{O}(1 \text{ m})$, suggesting that turbulence was not directly affected by the presence of the free surface (Figure 4.10d). The Thomas and Taylor (2010) estimate for the FSI-induced dissipation rate averaged across the forced SI layer, $\varepsilon_{SI} = (B_0 + B_E)(1 - h/H)^2/2$ (section 2.2b), yields $\varepsilon_{SI} = 0.4 \times 10^{-6} \text{ W kg}^{-1}$ in this case. This value is of the same order of magnitude but slightly smaller than the observed value, $\varepsilon = 1.5 \times 10^{-6} \text{ W kg}^{-1}$, pointing at an additional source of turbulence in the forced SI layer. Values of the gradient Richardson number were close to or below the threshold for shear instability throughout the forced SI layer (Figure 4.9d) suggest that region IV may be characterized by a mixture of shear-instability and FSI.

The stability regime in region IV is contrasted by region VI, where cyclonic vorticity was relatively strong, while M^2 was small, and may even became negative at greater depths (Figure 4.5a). In view of the latter, it is little surprising that the frontal jet in this region shows no indications for a geostrophic balance (Figure 4.9c), and no layer with negative PV can be identified (Figure 4.10c). SI can therefore not be expected, and other instabilities must be acting to maintain the observed high levels of turbulence (Figure 4.10f) in the presence strong restratification (note that N^2 increases toward

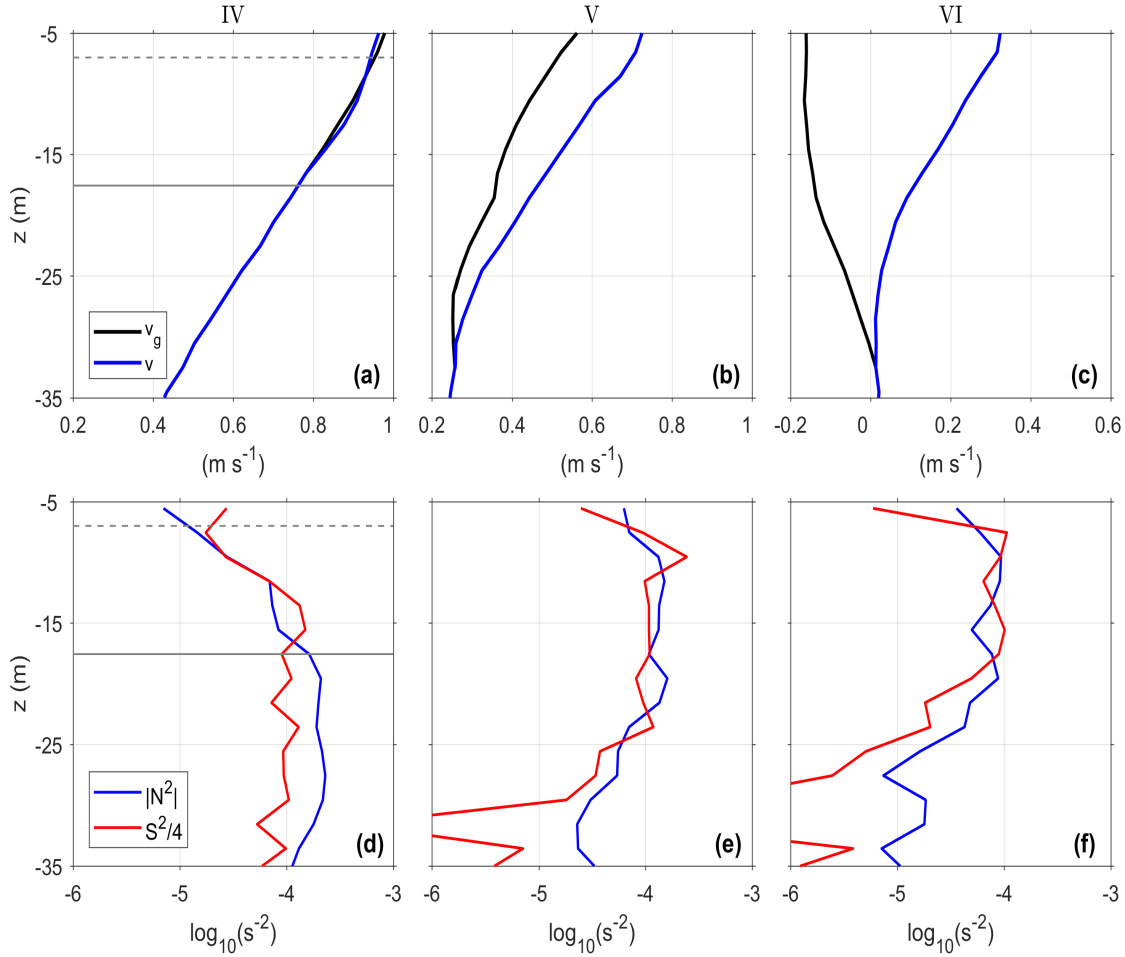


Figure 4.9.: As Figure 4.6 but now for subregions IV, V, and VI. Note the different axes ranges compared to Figure 4.6. The figure is taken from Peng et al. (2020).

the surface in this region, opposite to what would be expected in a classical oceanic SBL). With the Richardson number fluctuating around the critical value $Ri = 1/4$ in the upper 20 m of the water column (Figure 4.9f), shear instability appeared to be the most likely source of turbulence in this region. In regions deeper than approximately 20 m, the shear of the frontal jet decays, and Ri became too large for shear instability. It may be speculated that the patchy turbulence in this region was driven by internal-wave breaking with vertical and temporal scales too small to be resolved by the measurements of this study.

Especially interesting is the frontal core region V, where both cyclonic vorticity and M^2 are large (Figure 4.5a,c), suggesting a competition between stabilizing and destabilizing effects according to (2.2). Figure 4.10b shows that the extreme vorticity, with $\zeta/f = 4.8$ on the average (Table 4.1) and local values nearly twice as large

(Figure 4.5c), was strong enough to fully compensate the destabilizing effect of baroclinicity throughout the SBL. SI therefore cannot play a role in this region. Figure 4.9e shows that, similar to region VI, the vertical shear associated with the frontal jet was sufficient to maintain a Richardson number close to the critical value for shear instability throughout the upper 25 m of the water column.

It is worth noting that the situation in regions V and VI is reminiscent of the “marginal stability” regime described by Smyth and Moum (2013) in the context of a stably stratified shear layer in the upper flank of the equatorial undercurrent, with the caveat that rotation effects play a more important role in the Benguela upwelling region.

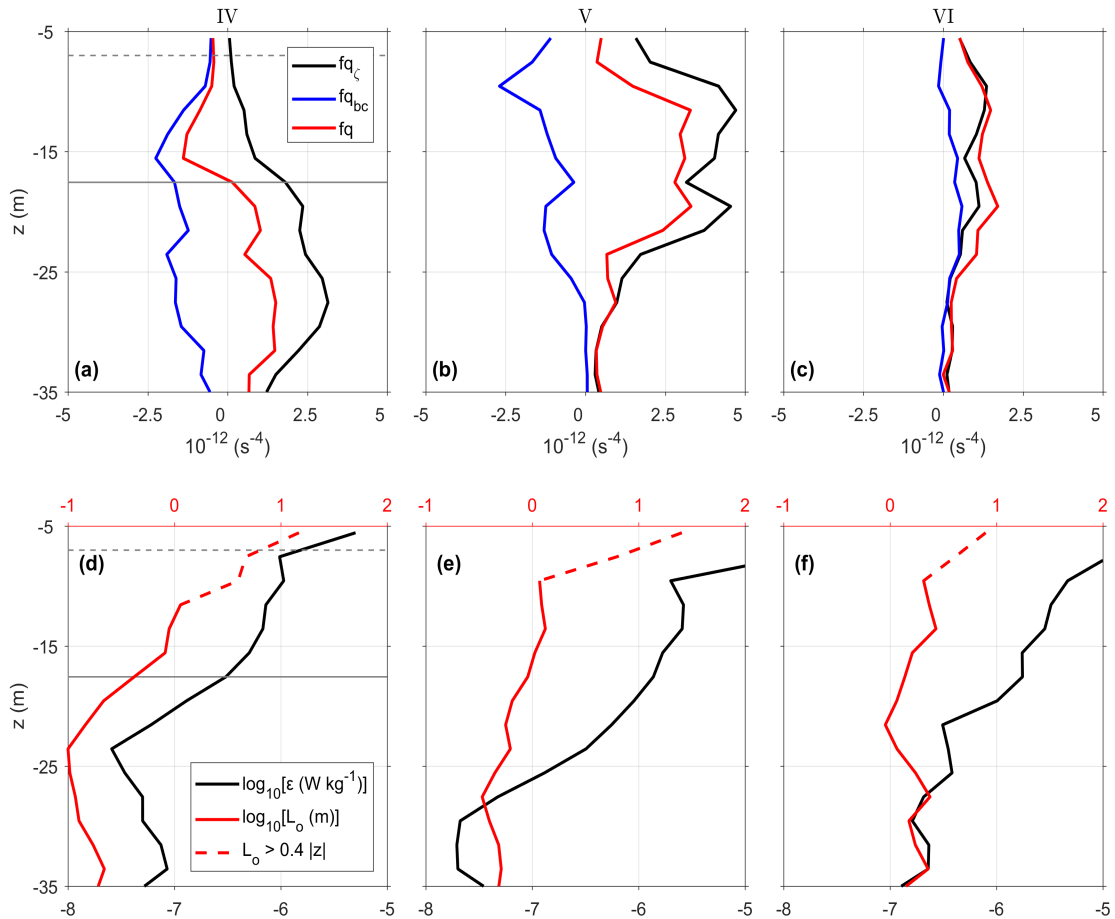


Figure 4.10.: As Figure 4.7 but now for subregions IV, V, and VI. Note the different axes ranges compared to Figure 4.7. The figure is taken from Peng et al. (2020).

4.5. Discussion

The very few existing studies of energy dissipation associated with FSI in submesoscale fronts identified similar processes and scaling relationships as in the regions II and IV (D’Asaro et al., 2011; Thomas et al., 2016). These investigations were, however, based on SBL-averaged turbulence parameters from a Lagrangian float, which complicates a direct comparison to the idealized simulations of Thomas and Taylor (2010) because SBL turbulence production by processes other than FSI (direct wind forcing, wave breaking, Langmuir turbulence, etc.) is more difficult to quantify. The microstructure-based measurements used in this thesis resolve the vertical structure of SBL turbulence, permitting, for the first time, to explicitly focus on the forced SI layer that is less likely affected by these processes due to the protecting effect of stable stratification and its deeper location at the bottom of the SBL, remote from the wave-affected near-surface region.

The impact of the cross-front density gradient on SBL turbulence can be quantified with the help of a modified Monin-Obukhov length scale (2.22) and the expression for the Ekman buoyancy flux in (2.6), assuming $B_E \gg B_0$ (as in the data used in this study). This yields

$$\frac{L_{MO}}{H} = \frac{1}{\kappa \cos \alpha_\tau} \frac{u_* f}{H M^2} = \frac{1}{\kappa \cos \alpha_\tau} \frac{u_*}{\Delta v_g}, \quad (4.1)$$

with α_τ denoting the angle between the downfront direction and the wind stress (recall that $\Delta v_g = H M^2 / f$ is the geostrophic velocity difference across the low-PV layer). Thus, while strong winds have a tendency to increase both Ekman-driven convective and directly wind-driven SBL turbulence, (4.1) shows that the latter effect dominates. This tendency may, however, be compensated by an increase in M^2 if the wind stress contains a downfront component. Moving from region IV in the core of the front to region I on the light side, ignoring the special region III for the moment, the values in Table 4.1 yield: $h/H = (0.41, 0.46, 0.67)$ and $L_{MO}/H = (0.21, 0.31, 0.57)$, suggesting that the variability of h , H , and L_{MO} among regions I, II, and IV is in excellent agreement with the prediction by (4.1). For the outermost region of the front ($-25 \text{ km} < x < -20 \text{ km}$), where the horizontal buoyancy gradient has decayed to $M^2 = 7.8 \times 10^{-8} \text{ s}^{-2}$, $L_{MO} = 35.3 \text{ m}$ is comparable to the total SBL depth, suggesting SBL turbulence is largely wind-driven, and not significantly affected anymore by the frontal buoyancy gradient. Region I approximately marks the transition point at which

FSI starts to become a relevant process in the lower part of the SBL. Although the lateral buoyancy gradient in region III is comparable to that in the outermost region (see Table 4.1), it has been shown in Section 4.4 that the governing processes are entirely different. The main reasons for these difference are the different vertical structure and the different lateral vorticity in both regions. While the outermost region was almost perfectly mixed across the upper 30-35 m, region III was characterized strong density gradients and strong anticyclonic vorticity, inducing mixed inertial/symmetrical instability.

4.6. Summary

The main results of this chapter are summarized in Figure 4.11, demonstrating the governing processes on the warm side of the front, and inside the anticyclonic and cyclonic flanks of the frontal jet. With reference to Figure 4.4d, the warm side of the front, corresponding to the range $-25 \text{ km} < x < -10 \text{ km}$, includes the outer region and regions I and II. This part of the frontal zone was characterized by a deep SBL and a moderate horizontal buoyancy gradient. The anticyclonic flank of the frontal jet (region III, $-9 \text{ km} < x < -4 \text{ km}$) was characterized by a Rossby number of $\zeta/f \approx -1$. Finally, the core frontal region was found near $-2 \text{ km} < x < 2 \text{ km}$ (regions IV-VI), where the strong cyclonic vorticity inside the flank of frontal jet plays an essential role.

The vertical structure and the governing processes in regions II and IV (Figure 4.11) are strikingly similar to those found in the idealized simulations of FSI by Taylor and Ferrari (2010). Moreover, the dissipation rates observed in the forced SI layer in the lower part of the SBL were in good quantitative agreement with a simple model by Thomas and Taylor (2010), based on idealized simulations, showing that the dissipation rate at which FSI extracts energy from the background flow scales with the Ekman buoyancy flux. These findings are consistent with previous studies (D'Asaro et al., 2011; Thomas et al., 2016), but extend them in one important point: the analysis of the vertical structure of FSI in submesoscale fronts.

Region III, located at the anticyclonic side of the front, was characterized by $\zeta/f < -1$ and $f q < 0$. This, combined with the characteristic instability patterns found in the cross-front velocity and indications for associated pycnostads and local density overturns, suggests that the flow was unstable with respect to ISI, as suggested by

Grisouard (2018). These indications for ISI are tightly linked to the strongly enhanced dissipation rate in this region, suggesting that ISI provides a direct pathway for the down-scale transport of large-scale *potential* energy towards small-scale turbulence and dissipation, extracting kinetic energy from the background flow.

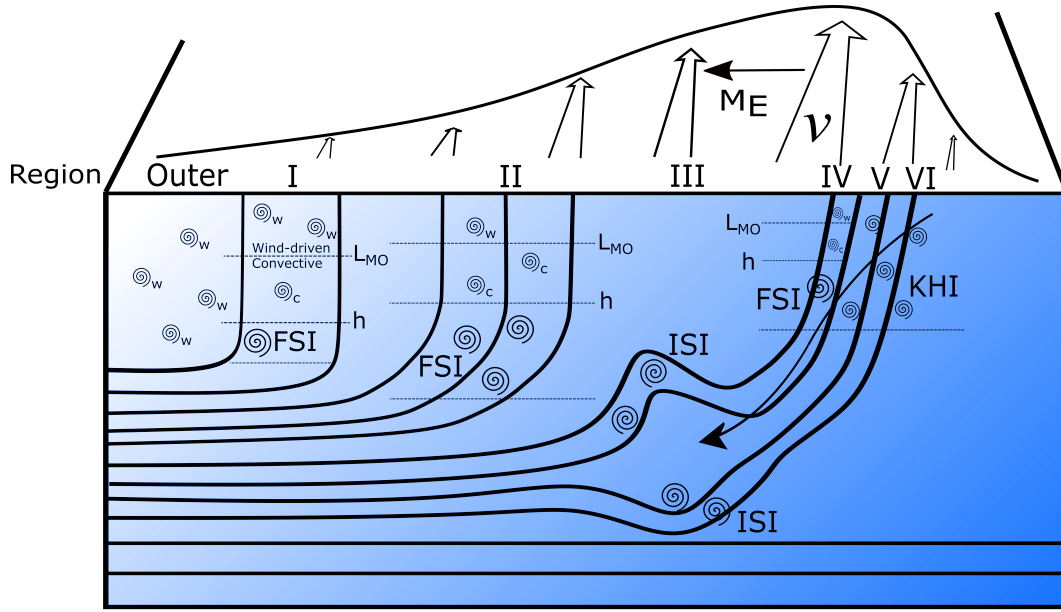


Figure 4.11.: Sketch of governing processes: (i) Region outer, I and II, corresponding to the region $(-25 \text{ km} < x < -10 \text{ km})$ with a deep SBL on the warm side of the main front, (ii) Region III, corresponding to the region $(-9 \text{ km} < x < -4 \text{ km})$ inside the anticyclonic flank of the frontal jet, and (iii) Region IV - VI, corresponding to the frontal region $(-2 \text{ km} < x < 2 \text{ km})$ with outcropping isopycnals inside the cyclonic flank of the frontal jet (see frontal structure in Figure 4.4). Abbreviations “w” and “c” refer to wind-driven and convectively-driven turbulence, respectively. KHI denotes regions prone to Kelvin-Helmholtz instability.

In regions V and VI, located at the cyclonic side of the frontal jet, conditions for SI ($|f q_{bc}| > f q_c$) were not satisfied due to strong cyclonic vorticity (Rossby numbers up to $\zeta/f = \mathcal{O}(10)$) in the upper 20 m, underlining the importance of the catamaran-based near-surface velocity measurements used in this study to correctly determine the stability properties of this narrow frontal region. Instead of FSI, it was found that in both regions V and VI, the vertical shear associated with the frontal jet brings the Richardson number close to the critical value for shear instability ($Ri = 1/4$), suggesting that the observed high mixing rates in these regions were associated with marginal shear instability (Figure 4.11).

The overall conclusion for this chapter is that forced symmetric instability, FSI, and marginal shear instability provide a down-scale transport of large-scale kinetic energy towards small-scale turbulence and dissipation, whereas inertial/symmetric instability, ISI, interacts with the large-scale density structure of the front, and thus provides an alternative pathway for the down-scale transport of potential energy.

Chapter 5.

Frontal instability and energy dissipation under variable surface forcing

This chapter is focused on frontal instability and associated turbulence in the upwelling filament FO in the outer region during daytime warming. The distinct hydrographic properties between dynamically active and density-compensated fronts are highlighted in the following. Enhanced turbulence found in the former is investigated in depth. This work is part of a manuscript in preparation.

5.1. Filament structure and evolution

Two corotating mesoscale eddies induced a confluent strain field, deforming the filament FO with a zonal extent of approximately 300 km off the Namibian coast (Figure 3.1a), consistent with the classical view of frontogenesis described in Section 2.1. Winds were around 10 m s^{-1} , directed northwestward with very little spatial variability (arrows in Figure 5.1a). Figure 5.1a,b shows that the front at the southern flank of the filament was generally more robust compared to that at the northern flank. This asymmetry is likely resulting from the stabilizing and destabilizing Ekman transports on the two sides of the filament, respectively. Both satellite and near-surface SST measurements across the southern front revealed a clear temperature gradient, suggesting the possibility of a density front.

The vertical structure along transects FO1 and FO2 is shown in Figure 5.1 which covers the inner region of the filament and its southern flank, bounded by the warm and saline ambient waters. During transects FO1 and FO2, microstructure measurements (see Section 3.2.1 for more details) were deployed in a continuous tow-yo mode from the slowly cruising ship, yielding an averaged horizontal profile spacing of a few hundred meters, sufficient to resolve the narrow fronts bounding the filament. Note that the high-resolution catamaran-based ADCP measurements were not available here, thus the ship-based ADCP measurements with much coarser resolution were used (see Section 3.2.2 for more details), thereby near-surface velocity structure were not resolved. However, the ship-based ADCP measurements were still helpful as the mixed layer depth was deep in this region during the cruise.

The transect FO1 (Figure 5.1c,e), observed during the transition from midday to late afternoon on 28 November, shows a well-defined SBL down to approximately 40 m depth, where it was capped by a stable density interface associated with the thermocline. It is noteworthy that a weaker secondary thermocline was observed inside the SBL, rising from around 20-30 m depth in the southern part of the transect up to the surface in the North. Clearly, the horizontal temperature gradients seen in Figure 5.1a,c were almost completely compensated by the cross-front salinity gradients induced by the lower salinity of the upwelling waters. Due to this effect, the resulting cross-front density contrast in the SBL was less than 0.1 kg m^{-3} .

The transect FO2 (Figure 5.1d,f), sampled from nighttime cooling to daytime warming on 02 December, exhibits a similar picture, however, with a smaller effect of density-compensation due to salinity, and thus a significantly larger cross-front density gradient. In the northern part of the transect, the filament was characterized by a well-mixed SBL of around 30-40 m thickness, capped by a sharp thermocline, whereas at the southern flank of the filament, indications of a secondary thermocline can be found at around 15 m depth. This suggests an increase in vertical stratification due to daytime warming. Especially interesting is the core frontal region, where a strong cross-front density gradient and outcropping isopycnals can be identified, pointing, in contrast to FO1, at a dynamically active frontal region.

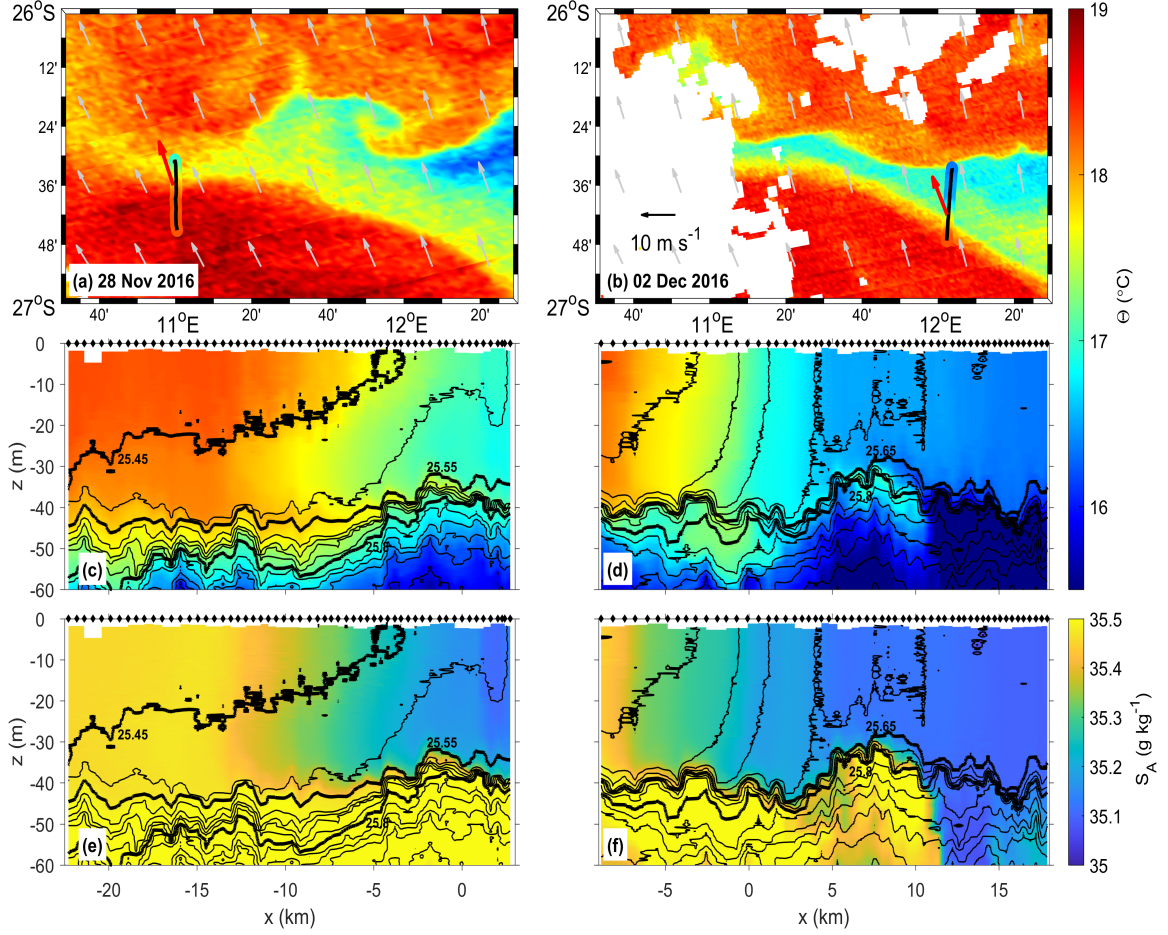


Figure 5.1.: Spatial and vertical structure for transects FO1 (left column) and FO2 (right column). Top row: satellite-based SST structure, obtained on 28 November and 02 December 2016, respectively, including near-surface temperature data along the ship track; cross-front variability of temperature (middle row), and salinity (bottom row) were projected onto the cross-front coordinate x as described in Section 3.3.1. Black contour lines in panels (c)-(f) denote isopycnals (potential density) at intervals of 0.05 kg m^{-3} ; black markers indicate locations of individual microstructure casts.

5.2. Atmospheric forcing

The temporal variability of the atmospheric forcing observed over 6 days, including the period of the ship-based measurements along transects FO1 and FO2, is shown in Figure 5.2. Note that, here, the decomposition of the wind stress into cross-front and downfront components in Figure 5.2a is based on the orientation of the front during transect FO2 (see Figure 3.1c). The wind stress was highly variable during this

period. The downfront component of the wind stress, τ_y^w , was positive throughout the measurements (thus supporting FSI via a positive Ekman buoyancy flux), but did not always dominate the total wind stress. The wind stress peaked around 0.4 Pa shortly after transect FO1 and exhibited another peak around 0.3 Pa just before transect FO2. Between these two transects, there were several events with a sudden change in the wind stress, pointing at a possible generation of near-inertial SBL oscillations that are known to affect frontal dynamics (e.g., Thomas et al., 2016). This mechanism will be discussed in greater detail below.

Figure 5.2b shows a clear diurnal signal in the surface buoyancy flux B_0 (positive for buoyancy loss, as defined in Section 3.2.4), peaking at approximately $B_0 = -6 \times 10^{-7} \text{ m}^2 \text{ s}^{-3}$ around midday due to strong solar heating, and at around $B_0 = 1 \times 10^{-7} \text{ m}^2 \text{ s}^{-3}$ due to atmospheric cooling during nighttime. This diurnal cycle was imprinted on the ship transects, depending on their relative timing. Both transects FO1 and FO2 were generally exposed to strong daytime heating (buoyancy gain), except for small parts affected by only weak atmospheric heat fluxes with a slight cooling tendency.

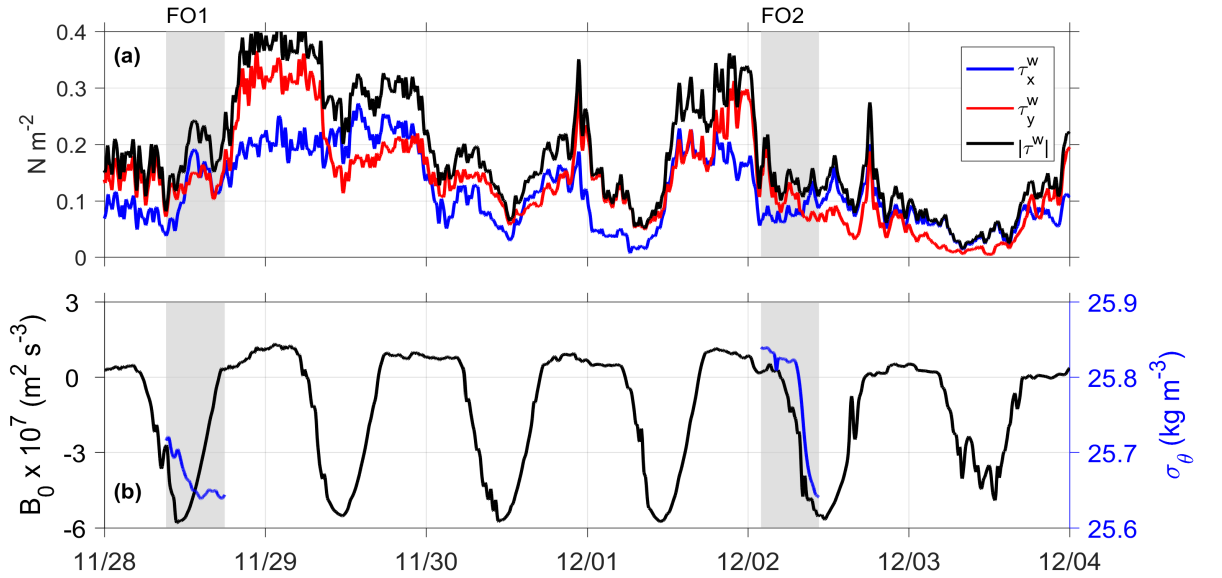


Figure 5.2.: Time series of (a) wind stress magnitude and cross-front, τ_x^w , and downfront, τ_y^w , components; and (b) net upward buoyancy flux B_0 (positive for buoyancy loss) during the transect measurements. The surface density observed along the cross-filament transects FO1-FO2 is shown in blue color in (b). Note that the decomposition into cross-front and downfront components in (a) is based on the orientation of the front during transect FO2 (see Figure 3.1c).

5.3. Frontal structure

Motivated by the competition between the destabilizing Ekman forcing associated with downfront winds and the stabilizing atmospheric forcing associated with diurnal warming, the velocity and turbulence structure of the density-compensated and dynamically active fronts will be discussed in greater depth in the following. The following data measured along the transects FO1 and FO2 were projected onto the cross-front direction x based on the respective frontal coordinate systems (see Figure 3.1b,c) as described in the context of Section 3.3.1.

5.3.1. Density-compensated front (FO1)

Transect FO1 (Figure 5.3) covers the transition between the warm ambient waters ($x < -5$ km) and the cold upwelling waters ($x > -5$ km) of the southern part of the large upwelling filament FO, as indicated in Figure 5.1c,e. Figure 5.3 shows that this transect was characterized by downfront velocities up to 0.6 m s^{-1} for $x > -5$ km, cross-front velocities up to -0.3 m s^{-1} for $x < -5$ km, and an approximately 40 m deep SBL with weak lateral buoyancy gradients (M^2 , as defined in Section 2.2). The value of M^2 peaked at a maximum value of $1.2 \times 10^{-7} \text{ m}^2 \text{ s}^{-3}$, which is reflected in the cross-front Ekman buoyancy flux B_E as defined in (2.6) (Figure 5.3a). During the transect, the negative atmospheric buoyancy flux B_0 (surface heating) was nearly always a few times larger than the Ekman buoyancy flux, thus indicating a tendency for restratification that leads to a suppression of turbulence in the mixing layer and thus to a strong reduction of the mixing layer depth shown in Figure 5.3d.

The turbulence data (Figure 5.3d) shows that the strongly turbulent near-surface region was capped from below by a secondary thermocline during daytime due to solar heating as discussed in Section 5.1. The mixing layer extended down to nearly 40 m at the southern end of the transect during nighttime cooling, while the tendency for restratification induced by solar heating lead to a strong reduction of the mixing layer depth to approximately 20 m at the northern end of the transect. The Monin-Obukhov length scale, defined in 2.5.1, generally traces the thickness of the SBL, except for the southern end of the transect ($x < -15$ m) where the total buoyancy flux was close to zero. This suggests that the turbulence in the upper part of the SBL (for $z > L_{MO}$) was driven by wind-forcing, and that mixing in the lower part of the SBL was suppressed by solar heating. However, as the focus of this thesis is on frontal instability, these

processes, associated mainly with the surface forcing, will not be analyzed in greater detail here.

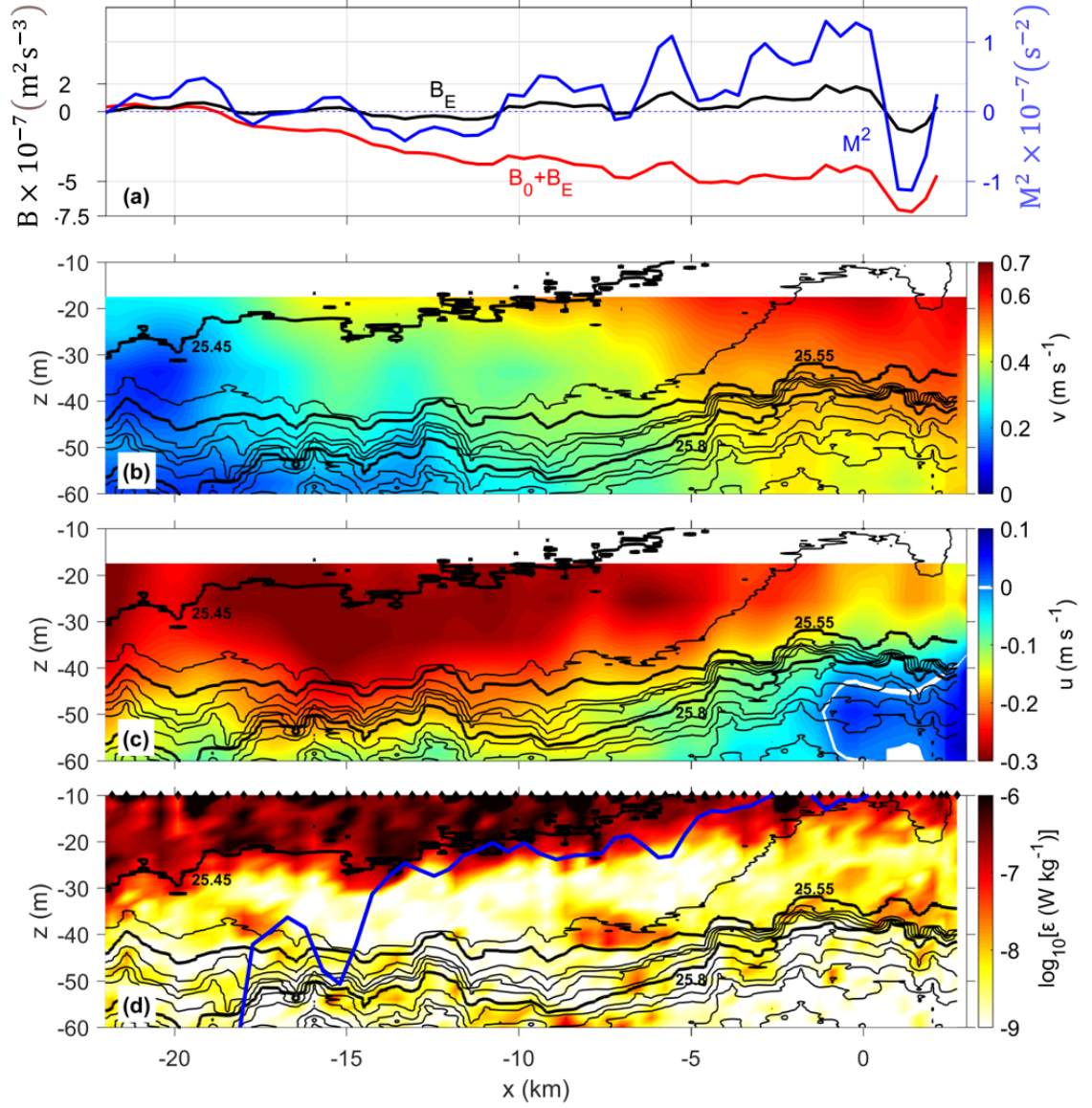


Figure 5.3.: Cross-front variability for transect FO1: (a) Ekman buoyancy flux (black), total buoyancy flux (red), and cross-front buoyancy gradient (blue); (b) downfront velocity; (c) cross-front velocity; and (d) turbulence dissipation rate. Blue line in (d) indicated the Monin Obukhov length scale defined in 2.5.1. Black contour lines in panels (b)-(d) denote isopycnals at 0.05 kg m^{-3} intervals; ; black markers indicate locations of individual microstructure casts.

5.3.2. Dynamically active front (FO2)

Figure 5.4 illustrates the structure of the southern part of the large upwelling filament shown in Figure 5.1b along transect FO2. Here, a 30-40 m deep SBL was observed, characterized by weak stratification, strong turbulence, and horizontal buoyancy gradients of the order of a few times 10^{-7} s^{-2} . The southern flank of the filament was bounded by a density front ($-3 \text{ km} < x < 4 \text{ km}$) with horizontal buoyancy gradients up to $M^2 = 4 \times 10^{-7} \text{ s}^{-2}$, and the frontal jet induced downfront velocities of up to 0.6 m s^{-1} . Further south ($x < -5 \text{ km}$), the transect was characterized by stably stratified waters with a relatively thinner turbulent mixing layer reaching down to around 15 m depth. For comparison, the strength of this density front is similar to region II ($M^2 = 2.6 \times 10^{-7} \text{ s}^{-2}$) of transect FC3 in the previous chapter, and the fronts with $M^2 = 2.1 - 8.5 \times 10^{-7} \text{ s}^{-2}$ used in the simulations of Taylor and Ferrari (2010).

The cross-front Ekman buoyancy flux B_E largely traces the variability of the horizontal buoyancy gradient (Figure 5.4a), and was generally positive. Thus, a destabilizing Ekman transport that moves dense water on top of lighter water is expected (see Section 2.3), which is consistent with the southward cross-front flow shown in Figure 5.4c. The competition between B_E and B_0 begins south of approximately $x = 5 \text{ km}$ due to increasing solar heating during the start of the day (the transect was measured in the southward direction between 1:56 UTC and 10:41 UTC). The stabilizing atmospheric forcing was generally sufficient to outweigh the destabilizing Ekman forcing, i.e. $B_0 + B_E < 0$ (red curve in Figure 5.4a). However, at $x = 0$, where the strongest buoyancy gradients are located, both buoyancy fluxes were in an approximate balance, i.e. $B_0 + B_E \approx 0$. No net buoyancy forcing is therefore expected in the core frontal region, which is important for the discussion of frontal instability in Section 5.4.1 below.

In the northern part of the transect, where the destabilizing surface forcing was still dominating, turbulence data (Figure 5.4d) show a strongly turbulent surface mixing layer that extended down to approximately 30-40 m depth, where it was capped by a stable density interface. At the southern flank of the filament, however, the beginning solar heating started to restratify the near-surface region, leading to a suppression of mixing in the lower part of the SBL. The situation is somewhat different in the core frontal region, where the destabilizing Ekman buoyancy flux plays an essential role, compensating the effect of solar heating. Thus, the vigorously turbulent mixing layer here is able to reach down to 30 m. It is noteworthy that patchy turbulence can also

be seen close or even inside the thermocline, pointing at local shear instability in this region.

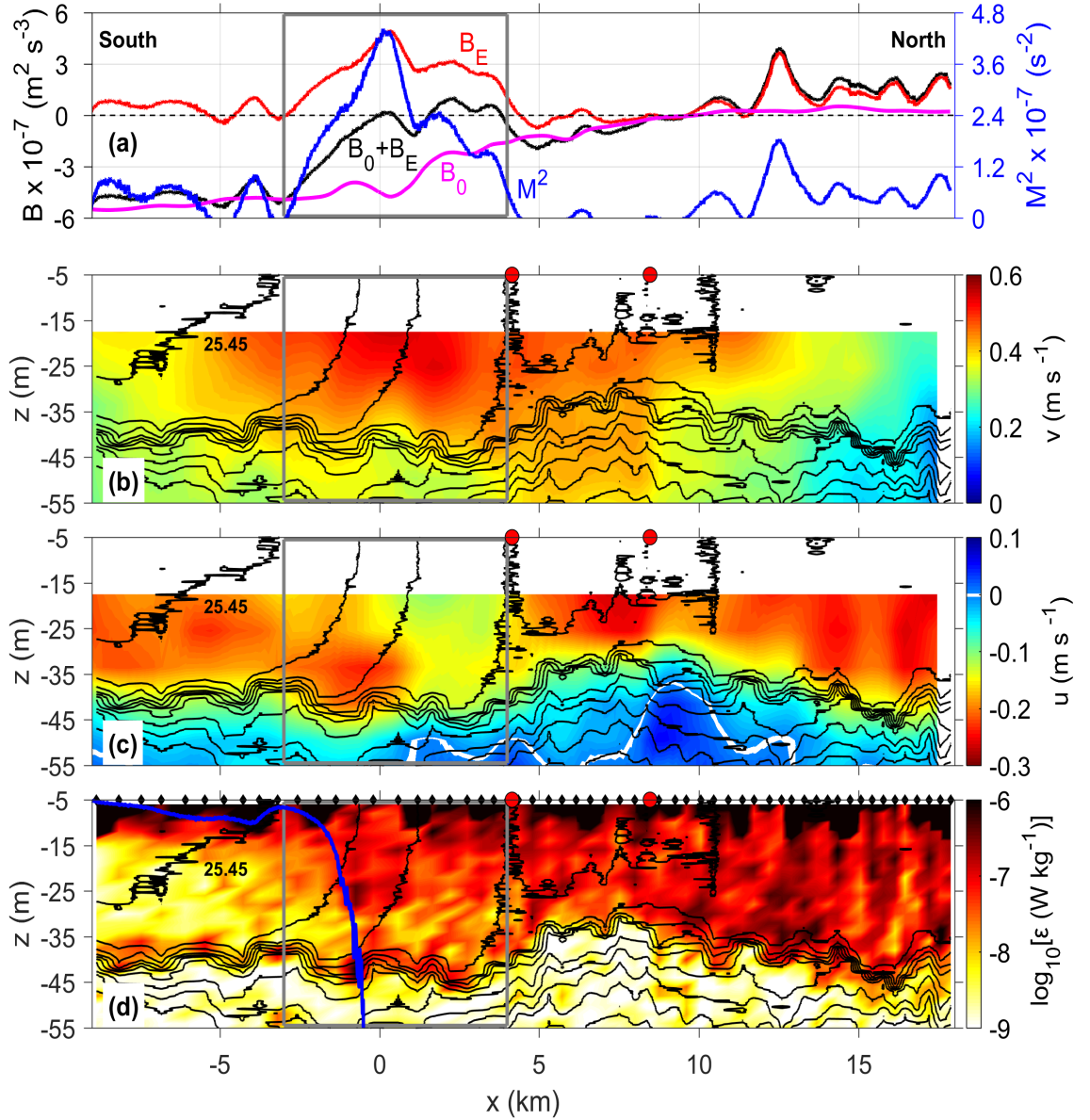


Figure 5.4.: Cross-front variability for transect FO2: (a) Ekman buoyancy flux (black), total buoyancy flux (red), and cross-front buoyancy gradient (blue); (b) downfront velocity; (c) cross-front velocity; and (d) turbulence dissipation rate. Black contour lines in panels (b)-(d) denote isopycnals at 0.05 kg m^{-3} intervals; black markers in panel (d) indicate locations of individual microstructure casts; gray thick line in panel (a) denotes the frontal region for the following discussion.

5.3.3. Hydrographic and mixing properties

The $\theta - S$ diagrams (Figure 5.5), covering the entire SBL and a small fraction of thermocline, shows the presence of different water masses and corresponding energy dissipation rates inside transects FO1 and FO2. Vertically, the data used for the $\theta - S$ diagrams ranges from an isopycnal with $\sigma_\theta = 25.8 \text{ kg m}^{-3}$ in the thermocline to the surface, excluding the uppermost 10 m due to the ship effects. Note that selected isopycnals, relevant for the following analysis, are labeled in Figure 5.1, Figure 5.3, and Figure 5.4, respectively.

For transect FO1 (Figure 5.5a), where a nearly density-compensated front was identified as shown in Figure 5.1c,e, the water masses can be categorized into three groups. With reference to Figure 5.1c,e, these groups include the warm and saline ambient waters, the cold and fresher upwelling waters, and the thermocline waters as indicated in Figure 5.5a. Data inside the SBL span a considerable temperature and salinity range but line up along a narrow density range in the vicinity of 25.5 kg m^{-3} , indicating that the upwelling waters and the ambient waters were well-mixed and that the cross-front density gradient was small (compensated front). The isopycnal corresponding to 25.45 kg m^{-3} separates a thin turbulent mixing layer in the upper part of the SBL from the non-turbulent, weakly stratified waters in the lower part of the SBL (indicated in Figure 5.5a), consistent with the secondary thermocline identified in Figure 5.3d. The nearly well-mixed but non-turbulent waters in the deeper layer below this secondary thermocline likely resulted from nighttime mixing, when SBL turbulence was not suppressed by solar heating (see above). The continuum of intermediate water masses bridging the range between the warm and salty ambient waters and the cold and fresh upwelling waters (Figure 5.5a) is interpreted here as the end product of continued cross-front mixing processes (see blue double-arrow). As any cross-front density gradients have nearly vanished at the location of outer filament FO1, these mixing processes must have a tendency to reduce such gradients. Thermocline turbulence is negligible along transect FO1 but turbulent patches are occasionally observed at the SBL base, indicating sporadic local shear instabilities (also see Figure 5.3d).

The $\theta - S$ diagram for the transect FO2 (Figure 5.5b), where a dynamically active front was observed, reveals similar water masses but suggests somewhat different dynamics, compared to the transect FO1 (Figure 5.5a). For transect FO2, the 25.65 kg m^{-3} isopycnal was used to separate the SBL from the thermocline (see blue dashed

line in Figure 5.5b and labeled isopycnals in Figure 5.4). Inside the SBL, the frontal waters bridged a considerable range of isopycnals between the warm and salty ambient waters and the cold and fresh upwelling waters (see blue double arrows), which is different from the nearly compensated front found along transect FO1. Enhanced dissipation rates in this region suggest that diapycnal (i.e., cross-front) mixing takes place, which will eventually lead to a reduction of the cross-front density gradient. In a Lagrangian sense, this might explain the observed reduction of the cross-front density gradient between FO2 and FO1.

On the other hand, the diapycnal mixing also occurred through the thermocline along various pathways (see 25.65 - 25.8 kg m^{-3} isopycnals in Figure 5.5b). Notably, the diapycnal mixing between the upwelling and thermocline waters can be clearly identified (see red double arrow), whereas the other pathways associated with the frontal waters and the ambient waters, however, were unclear to be identified. Nonetheless, the active isopycnal mixing among different water masses through the thermocline points to the importance of thermocline turbulence.

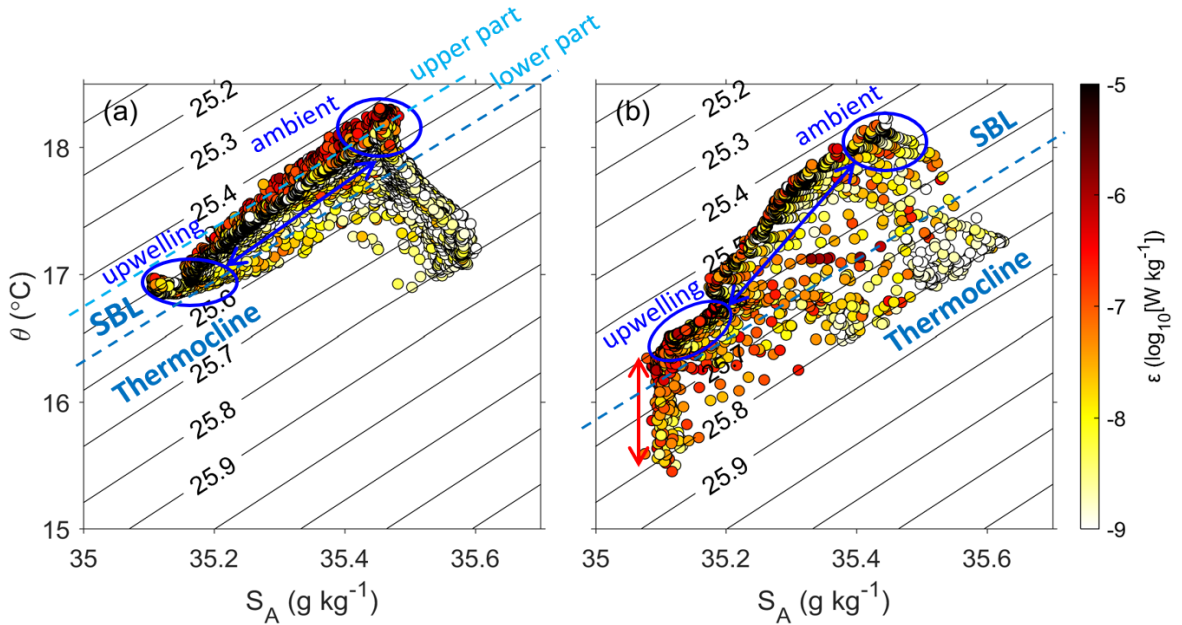


Figure 5.5.: The $\theta - S$ diagram for transects FO1 (a) and FO2 (b), with data above the isopycnal of 25.8 kg m^{-3} as indicated in Figure 5.1c-f, excluding the uppermost 10 m. The color shading indicates turbulence dissipation rate.

5.4. Analysis of frontal instability and turbulence

In this section, the theory and methods outlined in Chapter 2 and Section 3.3.2, respectively, are applied to investigate frontal and the thermocline mixing along transect FO2. To this end, the microstructure data and the ADCP data were processed with the following procedures.

First of all, the raw density profiles from the microstructure data at 0.1-m vertical resolution (described in Section 3.2.1) and the raw cross- and alongfront velocity profiles from the ADCP data at 8-m vertical resolution (described in Section 3.2.2) were horizontally filtered with a 2-km box filter to remove random fluctuations in the raw data. Then, the density data were vertically filtered with a 8-m box filter, corresponding to the thickness of the ADCP bins, and the ADCP data were horizontally interpolated to the locations of the microstructure casts (see black dots in Figure 5.4c). For the subsequent analysis, the vertical velocity shear and vertical buoyancy gradient were computed for each profile by vertical finite differencing across two ADCP bins, yielding quantities located between the centers of the staggered vertical ADCP bins. Horizontal velocity shear and horizontal buoyancy gradients were computed for each profile by horizontal finite differencing, which were then linearly interpolated to locations of vertical gradients for consistency.

5.4.1. The core frontal region

The core frontal region for transect FO2 approximately corresponds to the range $-3 \text{ km} < x < 4 \text{ km}$ (as indicated by the gray horizontal bar on the top of Figure 5.4a), where B_E and M^2 were always positive and outcropping isopycnals were observed. This region, characterized by a moderate lateral buoyancy gradient, stable stratification, and vigorous turbulence, was only weakly affected by the surface buoyancy forcing as $B_0 + B_E \approx 0$ (see Figure 5.4a).

This core frontal region can be horizontally subdivided into a cyclonic side ($Ro = \zeta/f > 0$) and an anticyclonic side ($Ro < 0$) based on the Rossby numbers shown in Figure 5.6d. Figure 5.6c illustrates that both regions contain subregions that satisfy the condition for symmetric instability ($f q < 0$, see blue contour). Recalling the stability conditions in (2.2), the cyclonic (anticyclonic) vorticity has a tendency of stabilizing (destabilizing) the flow by increasing (decreasing) the vertical component $f q_\zeta$ of the

total PV. This relation becomes clearer in the individual components of the total PV shown in Figure 5.6d, which were computed by vertical averaging of the data across the uppermost two bins for the total vertical shear (located between the centers of the staggered vertical ADCP bins) as indicated by the black dashed lines in Figure 5.6c.

Figure 5.6d shows that on the cyclonic side of the front, the vertical component $f q_\zeta$ of the total PV was positive but not sufficiently large to fully compensate for the destabilizing baroclinic term $f q_{bc}$ of the total PV everywhere. Over most of this region, the values of $f q$ therefore remain close to zero, indicating unclear conditions for SI, but they do show a trend towards negative values near the transition from the cyclonic to the anticyclonic side of the front. The gradient Richardson number Ri , indicated by the red contour in Figure 5.6b, suggests that turbulence on the cyclonic side of the front was mainly associated with shear instability. On the anticyclonic side of the front, on the other hand, the destabilizing baroclinic term $f q_{bc}$ dominates the total PV and clearly outweighs the positive vertical component $f q_\zeta$, resulting in a negative $f q$ across the entire region, and thus in conditions favorable for SI. It is interesting to note that active SI was identified here in a situation where the total surface buoyancy flux $B_E + B_0$ was close to zero. This is inconsistent with the argument that forced SI in the SBL can only be sustained for $B_E + B_0 > 0$, i.e. when PV is permanently drained from the SBL at the surface (D'Asaro et al., 2011; Taylor and Ferrari, 2010; Thomas and Taylor, 2010). Therefore, for the subsequent analysis, the anticyclonic side of the front, characterized $Ro < 0$, will be the focus.

5.4.2. The anticyclonic region

The anticyclonic region ($Ro < 0$) of the core frontal region is defined here as the horizontal range $-1.6 \text{ km} < x < 0.3 \text{ km}$ (indicated by the gray shaded area in Figure 5.6d). As shown in Figure 5.6c,d, this region was characterized by $f q < 0$ and $f q_\zeta > 0$, and the conditions for SI were thus clearly satisfied. For the subsequent analysis, region-averaged profiles were obtained by horizontally averaging the processed data across the anticyclonic region. Note that due to the low vertical resolution of the ADCP, only two vertical shear bins were available in the low-PV layer, defined here, analogously to Chapter 4, as the near-surface layer for which $f q < 0$ (Figure 5.6b). Note that the vertical gradients inside this layer were small, and they could therefore be resolved even with the low-resolution ADCP data that were available for this study (this is different from the thermocline region discussed below).

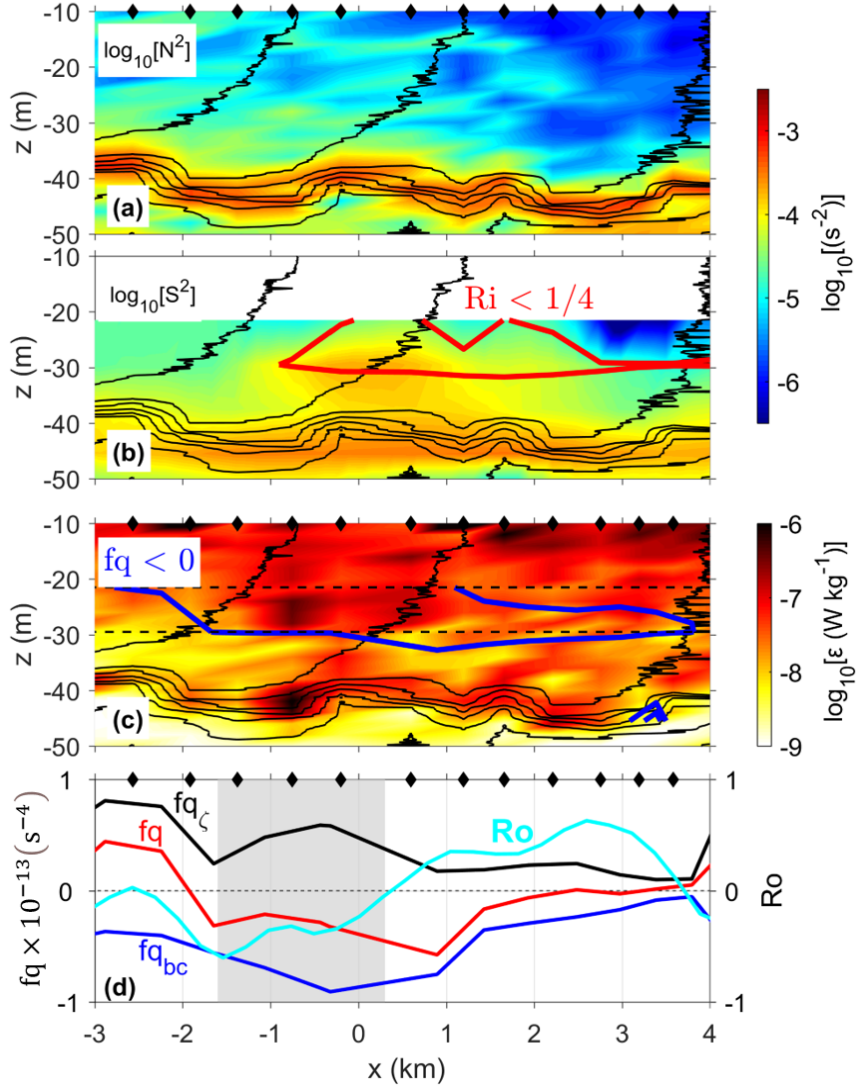


Figure 5.6.: Cross-front variability for the frontal region: (a) the square of buoyancy frequency, (b) the square of total shear with the condition for shear instability marked by the red contour line (c) turbulence dissipation rate with regions with $f_q < 0$ as indicated by the blue contour line, (d) vertical-averaged vertical, baroclinic, and total PV as defined in (2.2) and (2.5), based on the data at the depth levels indicated by black dashed lines in panel (c), and the Rossby number from the uppermost bin of the ADCP at -17.5 m (cyan line). Black contour lines in (a), (b), and (c) denote isopycnals at 0.05 kg m^{-3} intervals; black markers indicate locations of individual microstructure casts; the gray-shaded area denotes the anticyclonic region of the front used for the stability analysis.

The low-PV layer in this region was approximately geostrophically balanced (Figure 5.7a) and strongly turbulent with $L_O = \mathcal{O}(1 \text{ m})$, suggesting that turbulence was not directly affected by the surface forcing. Values of the gradient Richardson num-

ber were close to the threshold for shear instability ($Ri < 1/4$) in the low-PV layer (Figure 5.7c), suggesting that this region was characterized by a mixture of shear instability and SI, which is similar to region IV in Chapter 4, except for the negligible net buoyancy forcing. As transect FO2 was measured during the transition from nighttime to daytime, one could therefore argue that SI was the dominant source for turbulence during nighttime, when the buoyancy forcing was much stronger, and that shear instability took over later during daytime, when the solar heating had further increased. More specifically, the measurements took place exactly at the transition between SI and shear instability. No matter which of these two regimes was active, it ultimately triggered small-scale turbulence and energy dissipation.

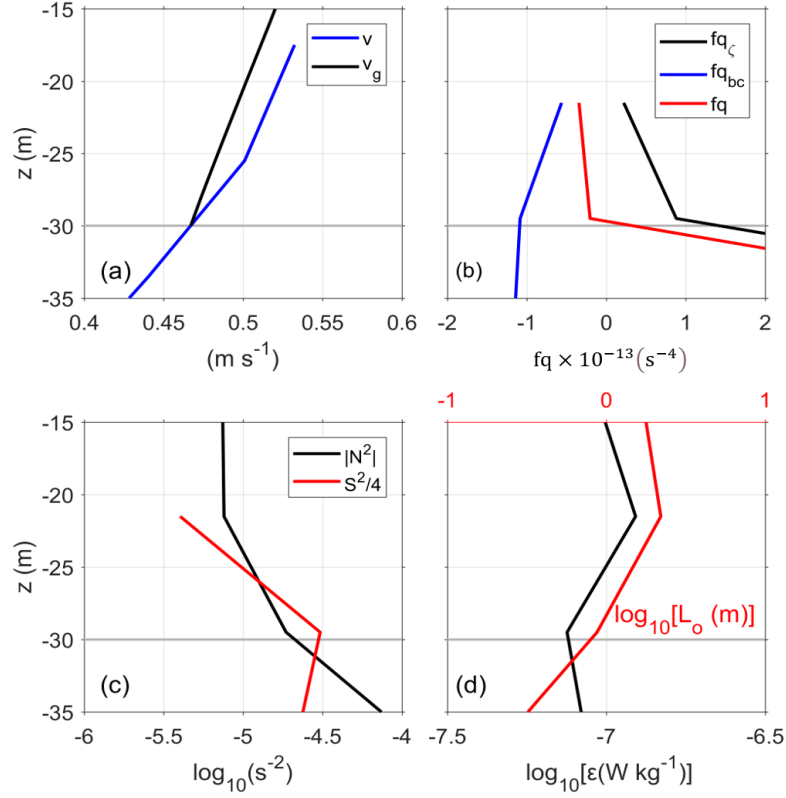


Figure 5.7.: Region-averaged profiles for the gray-shaded area in Figure 5.6d: (a) geostrophic and observed alongfront velocities, (b) vertical, baroclinic, and total PV as defined in (2.2) and (2.5), (c) squares of buoyancy frequency and total vertical shear. Note that the shear squared has been divided by a factor of 4 to ease comparison with the critical Richardson number ($Ri = 1/4$), and (d) turbulence dissipation rate and Ozmidov length (2.5.2).

5.4.3. The thermocline region

The thermocline region, where a local peak in the dissipation rate was observed (Figure 5.6c), is the focus of Figure 5.8. The overlying stable stratification limits the penetration of surface-layer turbulence down to the thermocline level. This suggests that the thin turbulent layer inside the thermocline was likely generated by the local shear across the thermocline, rather than being directly affected by surface turbulence. Of the two components of the total vertical shear, the cross-front shear was dominating (Figure 5.8c-e). The only conceivable generation mechanism that can possibly cause turbulence inside the thermocline in this situation is shear instability. To investigate this point in more detail, vertical profiles of shear and stratification were computed at the 8-m vertical resolution of the vessel-mounted ADCP (density profiles were again 8-m vertically filtered for consistency, as described above), and horizontally averaged over a subregion with particularly strong thermocline turbulence (see the gray bar in Figure 5.8a). The results in Figure 5.9 show, surprisingly, no indication for shear instability ($Ri < 1/4$) in the thermocline.

One likely explanation is that the available 8-m resolution for the velocity data is hardly sufficient to resolve the shear across a thermocline that is only a few meters thick. Moreover, horizontal averaging is likely to overestimate the thickness of the thermocline due to the large isopycnal displacements visible in Figure 5.8, which would also be reflected in a spurious increase of Ri . To estimate the relevance of this bias, horizontally and isopycnally averaged values of ε and N^2 are compared in Figure 5.9a,b (see Appendix C for more details). For the isopycnal averaging, a density range between $\rho_{up} = 25.57 \text{ kg m}^{-3}$ at the bottom of the SBL and $\rho_{lo} = 25.83 \text{ kg m}^{-3}$ just below the thermocline was used as indicated by pink lines in Figure 5.8.

Figure 5.9a,b show a clear discrepancy between isopycnally-averaged and depth-averaged N^2 and ε , e.g. regarding the peak value of N^2 and the thickness of the turbulent layer, illustrating that the large isopycnal displacements in the thermocline smears the density interface while averaging the data horizontally (see gray and blue curves). Moreover, it also illustrates that 8-m vertical averaging (black curve) strongly underestimates both parameters in the density interface, and obviously the same has to be expected for the shear shown in Figure 5.8c-e. This explains that the 8-m resolution of the ADCP is not sufficient to resolve a thin turbulent shear layer with a thickness of approximately 5 m (black curve Figure 5.9a,b) inside the thermocline. It is therefore not surprising that no indications for shear instability are found at 8-m res-

olution. Finally, it is important to note that the strong cross-front shear dominated the total vertical shear in the thermocline (Figure 5.9c), and the locally enhanced mixing rates therefore have to be attributed to this component. In the next section, possible mechanisms inducing the strong cross-front shear will be discussed.

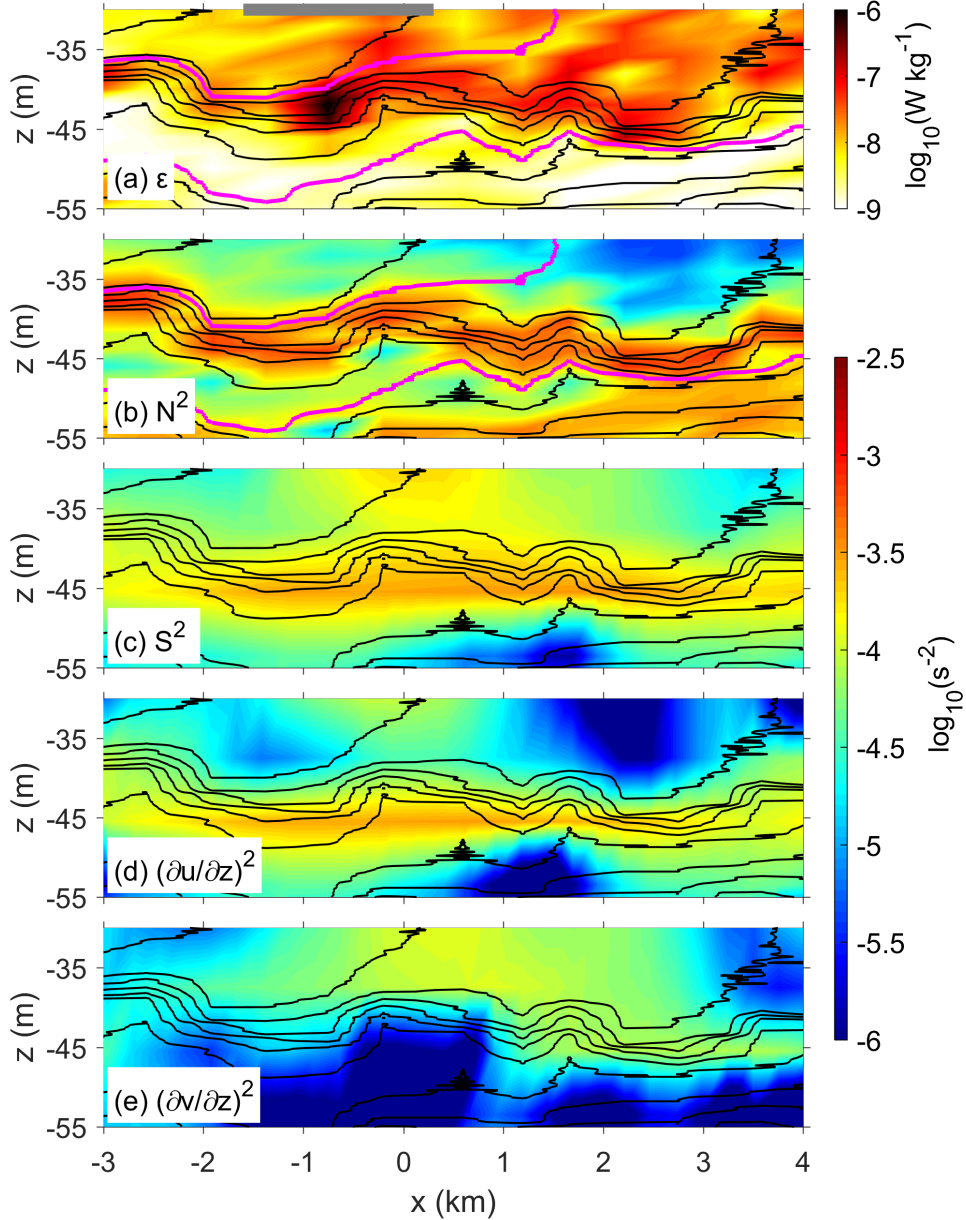


Figure 5.8.: Cross-front variability of (a) turbulence dissipation rate (b, c) the squares of buoyancy frequency and total vertical shear, and (d, e) the squares of cross-front and along-front components of the total vertical shear for the frontal region. Black contour lines denote isopycnals at 0.05 kg m^{-3} intervals; the gray bar on the top of panel (a) denotes the core frontal region; pink lines in panel (a) and (b) define the upper and lower limits used for isopycnally averaging.

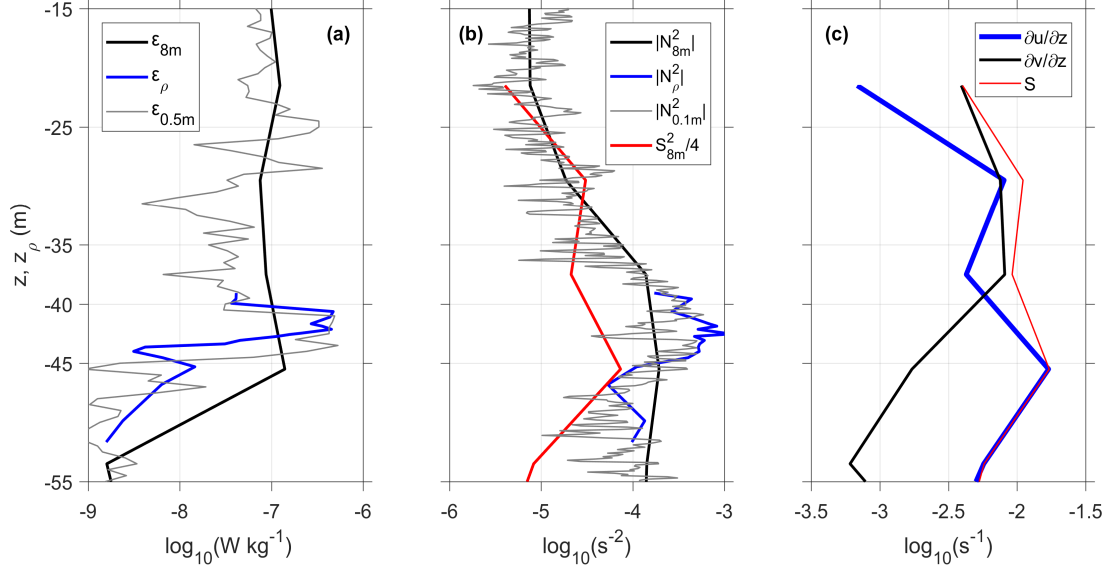


Figure 5.9.: Profiles of (a) depth-averaged and isopycnally-averaged turbulence dissipation rate, ε and ε_ρ , (b) depth-averaged and isopycnally-averaged squares of buoyancy frequency, $|N^2|$ and $|N_\rho^2|$, and depth-averaged total vertical shear, and (c) depth-averaged total vertical shear and its u and v components for the selected region indicated by the gray line in Figure 5.8a.

5.4.4. Wind-forced inertial oscillation

The combination of the strong cross-front shear (Figure 5.9c) and large variations in the wind stresses (Figure 5.2a) points towards the possibility of inertial motions in the SBL that have been frequently studied with slab-like models in the past (e.g., Pollard, 1970; D’Asaro, 1985; Thomas et al., 2016). To investigate this point, a simulation based on a slab-like model was conducted here. The equations governing the dynamics of wind-forced inertial motions averaged over the surface boundary depth H can simply be derived from integrating (2.8), assuming horizontal homogeneity ($\partial p/\partial x = \partial p/\partial y = 0$). Under these conditions, (2.8) becomes

$$\begin{aligned} \frac{\partial u}{\partial t} - fv &= \frac{\tau_x^w}{\rho_0 H}, \\ \frac{\partial v}{\partial t} + fu &= \frac{\tau_y^w}{\rho_0 H}, \end{aligned} \quad (5.1)$$

where $\nu \partial u/\partial z$, $\nu \partial v/\partial z$, $\langle u'w' \rangle$, and $\langle v'w' \rangle$ at $z = -H$ are neglected due to their (assumed) small contribution. To be directly comparable with the observations, this simulation was forced with the observed wind stresses (see Figure 5.10a). The wind

speed was spatially rather uniform within a radius of 200 km around transect FO2, such that similar inertial oscillations are expected to be generated everywhere in this region. This justifies the use of meteorological data from a non-stationary platform to compute the model forcing. The simulation was initialized on 28 November with $u = v = 0$, and a constant $H = 40$ m, corresponding to a typical SBL depth during the measurements, was assumed. This gives the simulation time to spin-up before the strong wind events during the period 30 November - 02 December. Note that the modeled u and v components are based on the orientation of the front during transect FO2 because this front is the main focus here (see Figure 3.1c). This decomposition is obviously arbitrary for measurements taken far away from the front.

Real-ocean velocities generally are dominated by geostrophic currents. For comparison with the model results, the contribution of the geostrophic currents therefore needs to be subtracted from the observed velocity, u_{obs} and v_{obs} . The geostrophic velocity at a given depth is the sum of two contributions: the first is the barotropic geostrophic velocity, $u_{g(bt)}$ and $v_{g(bt)}$, associated with the sea surface height (SSH) gradient, which is vertically constant; and the second is the baroclinic contribution, $u_{g(bc)}$ and $v_{g(bc)}$, due to horizontal density gradients, which is vertically variable. The SSH data described in Section 3.2.1 allow us to compute the barotropic geostrophic velocity for the entire domain (see Figure 3.1a), while the baroclinic geostrophic velocity was computed based on the density profiles from the microstructure data described in Section 3.2.5. These baroclinic velocities are, however, only available for the frontal region along transect FO2, and only $v_{g(bc)}$ was computed as no variability in alongfront direction is assumed. In addition, it is important to consider the effects of Ekman transport as it is potentially controlling the cross-front velocities when there is a downfront wind (described in Section 2.3). Therefore, the Ekman velocities, $u_{Ek} = \tau_y^w / \rho_0 f H$ and $v_{Ek} = -\tau_x^w / \rho_0 f H$ (a constant $H = 40$ m, corresponding to a typical SBL depth during the measurements, was assumed), need to be subtracted from u_{obs} . For the comparison, the residual observed velocities were vertically averaged over the SBL.

A number of key features are well-reproduced in the simulation. Figure 5.10b,c shows that the flow (black curves in the figure) oscillates with a period of slightly longer than a day, consistent with the inertial period $T_f = -2\pi/f = 26.5$ hours in this area, indicating an inertial oscillation. The magnitude of this oscillation increases significantly from 01 December onwards, following a strong wind event (Figure 5.10a). The good agreement in the cross-front velocity u between the model and the observations for the core frontal region along transect FO2 (indicated by the gray-shaded

area) supports that above idea that the strong cross-front shear can be attributed to cross-front inertial oscillations, which were at a local maximum at the time of the measurements. Note that the model was not tuned in any way to match the observations. Figure 5.10c shows that other processes were dominating the alongfront velocity v rather than only geostrophic currents and Ekman currents.

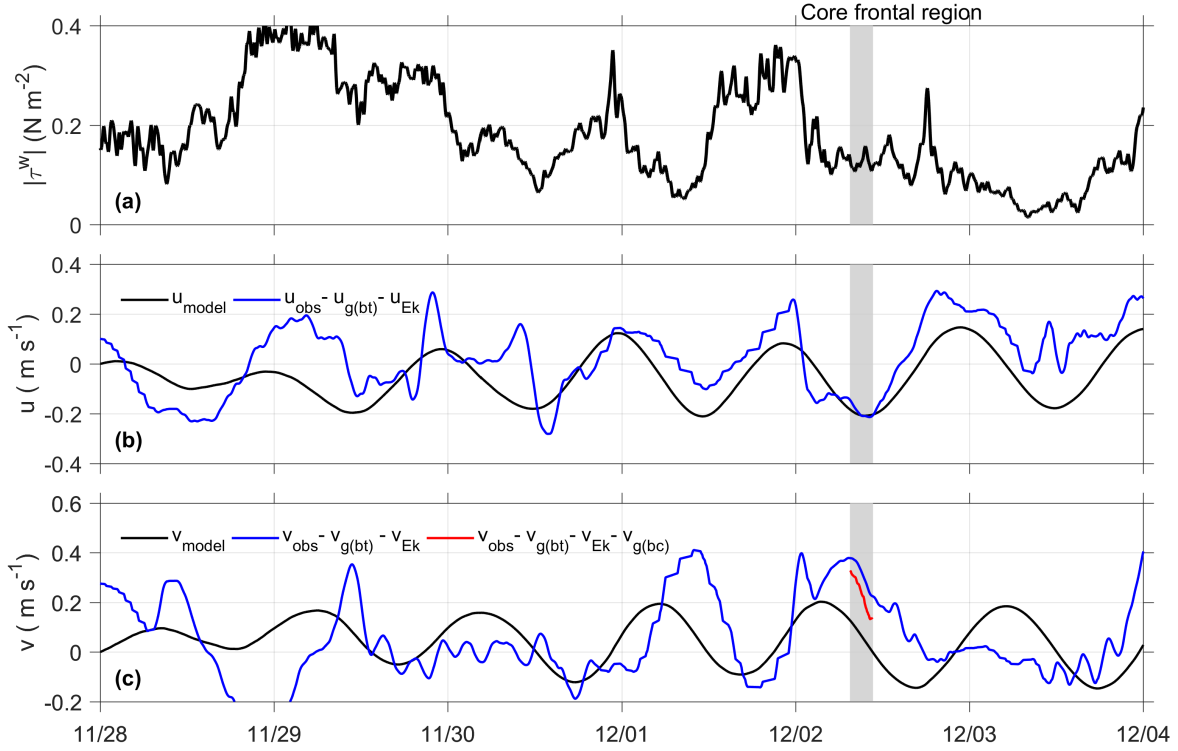


Figure 5.10.: Time series of (a) the magnitude of the total wind stress (b) the SBL-averaged cross-front velocity u from the model and the observations with the barotropic geostrophic velocities and Ekman velocities subtracted, (c) as (b) but for the alongfront velocity v and with an additional v with barotropic and baroclinic geostrophic velocities, and Ekman velocities subtracted (red curve). Gray-shaded area in each panel denotes the core frontal region along transect FO2.

5.5. Discussion

A few existing studies have shown that the theoretical scaling of SI dissipation rate is in good agreement with turbulence observations in the presence of destabilizing surface forcing, i.e. $B_0 + B_E > 0$ (Thomas and Taylor, 2010; D’Asaro et al., 2011; Thomas et al., 2016). However, how SI-turbulence behaves if $B_0 + B_E \leq 0$ remained unclear.

At the moment, available parameterizations ignore SI-induced mixing if $B_0 + B_E \leq 0$, assuming a complete shut-down of SI in this case (e.g., Bachman et al., 2017). The microstructure-based measurements used in this thesis resolve the vertical structure of SBL turbulence, explicitly showing SI-induced turbulence during the transition towards shear instability ($Ri \approx 1/4$). This turbulence is less likely affected by other near-surface processes due to the protecting effect of stable stratification and its deeper location of the SBL, remote from the wave-affected near-surface region. These are the first direct field observations supporting the relevance of symmetric instability under conditions with a negligible net buoyancy forcing (i.e. $B_0 + B_E \approx 0$) that has so far rarely been discussed in theoretical and numerical investigations. However, during daytime, when the magnitude of the stabilizing atmospheric buoyancy flux is larger than the destabilizing Ekman buoyancy flux, i.e. $B_0 + B_E < 0$, SI is likely to be replaced by shear instability (or by a gradual decay of turbulence), suggesting that the diurnal variability plays an important role in controlling frontal instability.

The high-resolution turbulence measurements within the anticyclonic region of the front along transect FO2 allow assessing the decay efficacy of kinetic energy of the jet due to small-scale turbulence. The local profile of kinetic energy of the jet $KE(z)$ for the anticyclonic side of the core frontal region was computed through

$$KE(z) = \frac{1}{2} | (v(z) - \langle v \rangle)^2 |, \quad (5.2)$$

based on the region-averaged profiles of the observed velocity $v(z)$ and the geostrophic velocity $v_g(z)$ as shown in Figure 5.7a, where $\langle \cdot \rangle$ indicates the vertical average across the low-PV layer. Vertically averaging $KE(z)$ yields the averaged frontal $\langle KE \rangle$ (per unit mass) for both v and v_g as summarized in Table 5.1 (the different vertical averaging ranges are also provided in this table). Note that since there were only a few velocity points available within the low-PV layer for calculation, $KE(z)$ was based on high-resolution linear interpolation of v . Similarly, the region-averaged turbulence dissipation rate profile shown in Figure 5.7d were vertically averaged across the low-PV layer, yielding the averaged turbulence dissipation rates $\langle D \rangle$.

From the averaged kinetic energy of the jet $\langle KE \rangle$ and the averaged turbulence dissipation rate $\langle D \rangle$, an estimate of the decay time scale of the jet due to the small-scale turbulence can be computed through

$$t_d = \frac{\langle KE \rangle}{\langle D \rangle}. \quad (5.3)$$

The results of this calculation for different cases are summarized in Table 5.1. The small decay time scale, $t_d = \mathcal{O}(1 \text{ hour})$, shows that small-scale turbulence has a strong dynamical impact on the frontal jet, and also suggests that the system can directly respond to diurnal changes in the surface forcing. It should be noted here that SI is also fueled by the horizontal shear of the jet, which is different from shear instability, therefore, implies a second decay time scale from SI that may be larger. This point will be subject of future research.

Table 5.1.: Vertically averaged parameters for the core frontal region along transect FO2, including the kinetic energy $\langle KE \rangle$, the dissipation rate $\langle D \rangle$, and the decay time scale t_d , based on the observed alongfront velocities v and the geostrophic velocity v_g across the deeper part of the low-PV layer ($-H < z < -17.5 \text{ m}$, corresponding to the ADCP range), and the full-depth of the low-PV layer ($-H < z < -10 \text{ m}$, corresponding to the turbulence profile range) additionally for v_g .

Velocity	Depth range (m)	$\langle KE \rangle$ (J kg^{-1})	$\langle D \rangle$ (W kg^{-1})	t_d (h)
v	$-H < z < -17.5$	1.88×10^{-4}	1.07×10^{-7}	0.49
v_g	$-H < z < -17.5$	0.88×10^{-4}	1.07×10^{-7}	0.23
v_g	$-H < z < -10$	2.36×10^{-4}	1.00×10^{-7}	0.65

5.6. Summary

Frontal instability and turbulence in an upwelling filament (Figure 3.1a) were investigated under conditions of both stabilizing buoyancy forcing (Section 5.3) and negligible net buoyancy forcing (Section 5.4). The data along transect FO1 show a nearly compensated front during daytime warming, revealing a complete shut-down of SI due to strongly stabilizing buoyancy forcing ($B_0 + B_E < 0$), where turbulence was mainly driven by wind-forcing. On the other hand, the data along transect FO2 show a dynamically active front under diurnal warming, characterized by a deep vigorously turbulent mixing layer, a moderate horizontal buoyancy gradient, and a negligible net buoyancy forcing (i.e. $B_0 + B_E \approx 0$). The governing processes inside the core frontal region along transect FO2 with reference to Figure 5.6, corresponding to the range $-3 \text{ km} < x < 4 \text{ km}$, are summarized in Figure 5.11. On the anticyclonic side of the front, two subregions with a local peak in turbulence were identified: (i) surface boundary layer turbulence characterized by strong baroclinicity, stable stratification,

and conditions favorable for SI (despite the negligible net buoyancy forcing), and (ii) thermocline turbulence, where the strong cross-front inertial shear plays an essential role. On the cyclonic side of the front, conditions for SI were less clear, and turbulence was more likely driven by shear instability.

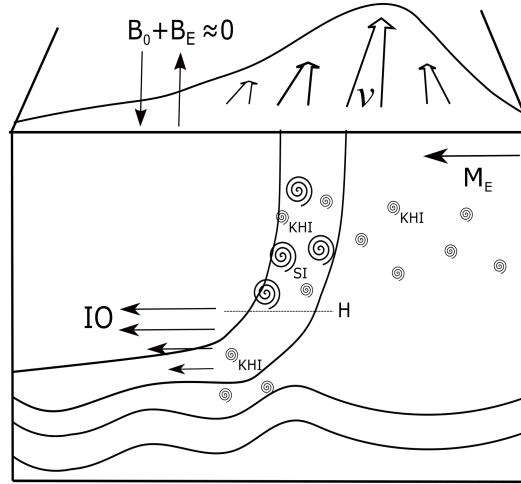


Figure 5.11.: Sketch of governing processes in the core frontal region ($-3 \text{ km} < x < 4 \text{ km}$): (i) negligible net buoyancy forcing ($B_0 + B_E \approx 0$), (ii) destabilizing Ekman transport, M_E , (iii) a mixture of SI and shear instability on the anticyclonic region of the front in the SBL (iv) shear instability on the cyclonic region of the front in the SBL, and (v) thermocline mixing driven by shear instability due to inertial oscillations (IO). KHI denotes regions prone to Kelvin-Helmholtz instability.

The core frontal region in the SBL was characterized by $f q < 0$ and $f q_{bc} > 0$. This indicates that the flow is unstable with respect to SI. The vertical shear associated with the frontal jet brings the Richardson number close to the critical value for shear instability ($Ri = 1/4$), indicating a transition from SI to shear instability. The mixture of SI and shear instability was tightly linked to the high mixing rates in this region. The small decay time scale of $\mathcal{O}(1 \text{ hour})$ for the vertical shear of the frontal jet, suggests a direct and efficient pathway for the down-scale transport of kinetic energy towards small-scale turbulence and dissipation. More importantly, this short decay time scale supports a strong diurnal variability of mixing.

A thin turbulent mixing layer was observed in the thermocline, where it was protected by overlying stable stratification, thus the direct effect of the surface forcing is expected to be less relevant. The only conceivable generation mechanism for the observed high turbulence levels in the thermocline is shear instability, which is, however,

not well-resolved by the 8-m vertical bins of the ADCP used in this study. Nonetheless, the total vertical shear was found to be dominated by the cross-front shear. A slab-like model suggests that the cross-front shear was excited by large variances in wind stresses that induced near-inertial oscillations.

The overall conclusion for this chapter is that both “unforced” SI and shear instability contribute, with variable proportions depending on the diurnally varying buoyancy forcing, to energy dissipation in a submesoscale front. This is different from the thermocline region, where turbulence inside a thin mixing layer was driven by a cross-front inertial shear triggered by rapid changes in the wind stress.

Chapter 6.

Conclusion and outlook

6.1. Overview

Recent theory and numerical simulations suggest submesoscale fronts and filaments are subject to various types of instabilities, providing a potentially important pathway for the downscale transport and dissipation of mesoscale energy in the ocean. The main focus of this thesis was to investigate the real-ocean relevance of these recent theoretical concepts.

6.2. Conclusion

The investigation was based on field data from two submesoscale upwelling filaments in the Benguela upwelling system (South-East Atlantic), which combined densely-spaced cross-front turbulence microstructure measurements with high-resolution velocity measurements taken simultaneously from a towed research catamaran. The observations were carried out under destabilizing ($B_0 + B_E > 0$), stabilizing ($B_0 + B_E < 0$) and negligible net buoyancy forcing ($B_0 + B_E \approx 0$) conditions, allowing an understanding of how energy is transferred in a submesoscale fronts under different buoyancy forcing.

In the presence of destabilizing surface forcing ($B_0 + B_E > 0$), the measurements revealed a sharp submesoscale front associated with an energetic frontal jet reaching speeds of up to 1.0 m s^{-1} at the edge of the upwelling filament, characterized by

downfront winds, strong horizontal density gradients, and vigorous turbulence. Three distinct stability regimes were identified:

(i) A 30-35 m deep mixing layer region, where down-front winds induced a vertical two-layer structure: the upper part of the low-PV layer was characterized by convective mixing due to the destabilizing cross-front Ekman transport, while in the lower part (the so-called SI layer) turbulence was driven by forced SI, which extracted the energy from the *kinetic* energy of the background flow. Dissipation rates in this region scaled with the Ekman buoyancy flux, in excellent quantitative agreement with recent numerical simulations of FSI.

(ii) The cyclonic flank of the main frontal region, where the cyclonic vorticity was sufficiently strong to suppress SI, despite strong baroclinicity. Turbulence in this region was locally driven by Kelvin-Helmholtz instability.

(iii) The anticyclonic flank of the main frontal region, characterized by a Rossby number of $\zeta/f \approx -1$ in the presence of weak lateral density gradients. The turbulence was driven by inertial/symmetric instability, which extracted energy from the *potential* energy of the background flow.

These are the first direct field observations that explicitly show the high-resolution vertical structure of the turbulence associated with forced SI and marginal shear instability, and captured a mixed type of symmetric/inertial instability. All these instabilities contribute to the down-scale transport of large-scale energy towards small-scale turbulence and dissipation, supporting recent theory.

The dataset measured in the virtual absence of the net buoyancy forcing ($B_0 + B_E \approx 0$) exhibit a sharp submesoscale front associated with a frontal jet of 0.6 m s^{-1} , a pronounced cross-front velocity of -0.2 m s^{-1} , and vigorous turbulence. Enhanced turbulence was identified in the SBL and thermocline of the anticyclonic frontal region. The turbulence in SBL, where characterized by moderate horizontal density gradients, a deep low-PV layer, and a negative Rossby number, was driven by a mixture of SI and Kelvin-Helmholtz instability, suggesting a transition between these two regimes. Where it was characterized by a strong cross-front inertial shear, a thin turbulent mixing layer in the thermocline was associated with shear instability triggered by wind-forced inertial oscillations. These are the first direct field observations that focus on unforced frontal instability and turbulence, which is inconsistent with the argument from previous studies that SI in the SBL can only be sustained under conditions with destabilizing buoyancy forcing.

Finally, the measurements obtained in the presence of stabilizing buoyancy forcing ($B_0 + B_E < 0$) reveal virtually no lateral buoyancy gradients and weak downfront winds, resulting in a complete shut-down of frontal instabilities, and showing that the turbulence in this case is driven by wind forcing. This suggests that the diurnal variability plays an important role in controlling frontal instability and associated turbulence.

Overall, the observations of this thesis provide direct evidence of the relevance of forced/unforced SI, ISI, and marginal shear instability for energy dissipation in submesoscale fronts and filaments, supporting the recent relevant theoretical concepts.

6.3. Outlook

There are several questions and challenges remaining at the end of this thesis which I hope to pursue in the future. In the following, points for future work are listed.

As shown in Figure 4.4c, a pronounced turbulent mixing layer within a narrow region down to 40 m depth was found inside the upwelling filament at approximately $x = 2 - 3$ km, close to the submesoscale front on the southern flank of the filament. Frontal instability and surface forcing seem to be less relevant to these sharp strongly turbulent mixing layers because of the virtual absence of baroclinicity, vorticity and the presence of stable stratification. As the data contained only a few profiles in this region and were measured in one direction (i.e a two-dimensional transect), diagnosing the source of the turbulence becomes difficult. Thus, it still remains unclear what the dominant processes of mixing are in this region. This would be an interesting focus for a further study.

In Chapter 5, a symmetrically unstable front and the cross-front shear associated with inertial oscillations in the SBL and the thermocline are separately discussed in section 5.4.2 and section 5.4.3. As suggested by Thomas et al. (2016), a potential interaction between a symmetrically unstable front and an inertial shear leads to a reduction of stratification, which makes the extraction of kinetic energy from the background flow under SI conditions more efficient. However, this process is time-dependent. As there was only one transect available, the data in this region are temporally limited, which makes studying in this transient process impossible. Therefore, it remains un-

clear how transient inertial shear effects the symmetrically unstable front. This would be another point for a further study.

Another interesting point in Chapter 5 is the reduction of cross-front velocity in the core frontal region shown in Figure 5.4c. This velocity reduction event is possibly associated with submesoscale mixed layer instability (Haine and Marshall, 1998; Boccaletti et al., 2007). This instability acts to draw potential energy from lateral density gradients and then converts it into eddy kinetic energy, and ultimately triggers an ageostrophic secondary circulation (See Figure 2.1), restratifying the mixed layer. An estimate of buoyancy flux due to mixed layer instability

$$B_{MLI} = -\frac{CH^2M^2}{|f|} \quad (6.1)$$

(where $C = 0.08$ is a model constant) proposed by Fox-Kemper et al. (2008) has been widely used in diagnosing the presence of mixed layer instability (e.g., Mahadevan et al., 2010; Köhn et al., 2017). Using the representative values of $H = -40$ m, $M^2 = 3.2 \times 10^{-7} \text{ s}^{-2}$, and $f = -6.6 \times 10^{-5} \text{ rad s}^{-1}$ for the frontal region along with transect FO2, gives a non-negligible value of $B_{MLI} = -2.0 \times 10^{-7} \text{ m}^2 \text{ s}^{-3}$, implying mixed layer instability may be present. However, further analysis is required. The competition between stabilizing and destabilizing processes may form another further study.

The focus of this thesis is on frontal instability and energy dissipation in submesoscale fronts, mainly paying attention to the deeper part of the SBL, where stable stratification is sufficiently strong to host frontal instability and quell surface turbulence. Based on Large Eddy Simulations, Hamlington et al. (2014) demonstrated a potential interaction between SI and Langmuir turbulence, and found that small-scale turbulence is amplified in the presence of Stokes forcing. This process, however, cannot be well-understood based on the observations in this thesis, as the data have a spatial resolution of a few hundred meters, and the upper 10 m of the data is always discarded due to ship effects. Thus these limitations make resolving a coherent structure of Langmuir turbulence impossible. So far, studies have rarely provided direct observations of co-existence of Langmuir turbulence and symmetric instability. It is worthwhile to discuss the real-ocean relevance of this recent concept based on data collected by instruments which can overcome the issues mentioned above, such as an autonomous glider.

Appendix A.

Accuracy of satellite SSH data

As an offset between features is seen in SST and SSH in the vicinity of the filament FC (black box in SIunits.dtx 3.1a), it is important to clarify the data quality of the SSH data that were used in the thesis, especially in the coastal upwelling cell. The measurement uncertainty of the AVISO product we used in our study is described in the CMEMS Quality Information Document (QUID) at <http://marine.copernicus.eu/documents/QUID/CMEMS-SL-QUID-008-032-062.pdf>. There, the uncertainty is estimated from a comparison with independent measurements from TOPEX-Poseidon. (Figure A.1) below shows the variances of the differences between both products for the Benguela upwelling region, based on the data directly from the AVISO team, shown in Figure 10 of the QUID document. It turns out that errors are not elevated in the vicinity of coastal upwelling cell, despite its proximity to the coast, with an average variance of 3.2 cm^2 across the area shown in (Figure A.1). This corresponds to an RMS of 1.8 cm, which is about 20 % of the SSH range in the vicinity of the two eddies in the filament region. The error is thus significant but too small to obscure the true SSH structure associated with these eddies. An offset between the features seen in SST and SSH thus can be argued that it is caused by the large resolution mismatch (1 km vs. 25 km) between two datasets.

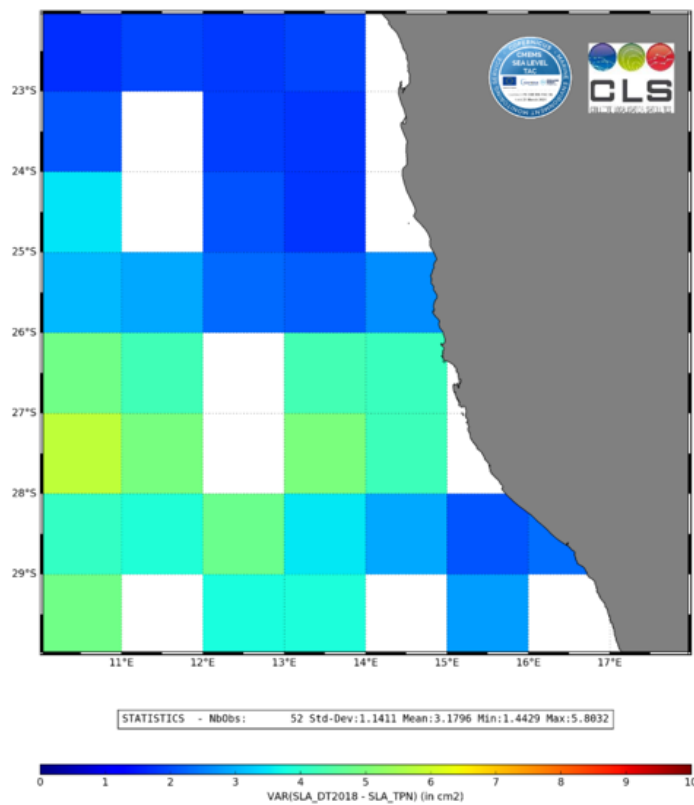


Figure A.1.: Variances of the differences between gridded AVISO SSH product and independent TOPEX-Poseidon along-track measurements using the DUACS DT2018 versions. The figure represents a zoom over the Benguela upwelling system. Source: AVISO team.

Appendix B.

Catamaran-mounted ADCP correction

As the catamaran was towed at a distance of 100-150 m behind the ship, moving among the surface waves, the velocity data collected from catamaran-mounted ADCP (CADCP) is needed to be corrected. The velocity data from the 75-kHz vessel-mounted ADCP (VADCP), which were always available during the entire campaign, were therefore taken as the reference. The following three steps demonstrate how the CADCP data were corrected with VADCP data as the reference.

Step 1. To ensure the consistency of vertical resolution for both data sets, CADCP data, obtained with the uppermost bin located 4.5 m below the surface in 2-m vertical bins, were vertically averaged across the VADCP data collected in the water column below 17.5 m depth in 8-m vertical bins.

Step 2. For the comparison, the relative velocity of the CADCP, u_c^{rel} , was computed by subtracting catamaran's moving velocity, u_c^{mv} , from the absolute velocity of the ocean current, u_c^{abs} , i.e. $u_c^{rel} = u_c^{abs} - u_c^{mv}$. Similarly, the relative velocity, u_v^{rel} , from the VADCP data was computed through $u_v^{rel} = u_v^{abs} - u_v^{mv}$.

Step 3. Finally, the relative velocity components from both datasets were compared to obtain the rotated angle for the CADCP correction. The comparison results were summarized in Table B.1. Based on the available data, it is suggested that the CADCP needs to be rotated with an angle of 313.0 °. Figure B.1 shows an excellent agreement between the velocities from the VADCP and the corrected CADCP.

Table B.1.: The least Root Mean Square of Difference (RMSD, unit: m s^{-1}) between velocity data from two ADCPs by rotating CADC data with the optimal angle in VADCP sampling depths. Data below 73.5 m depth were not considered due to large data missing.

Depth (-m)	Optimal angle ($^{\circ}$)	RMSD u	RMSD v	Data missing (%)
17.5	314.2	0.11	0.12	0
25.5	313.0	0.10	0.13	0
33.5	313.0	0.10	0.13	0
41.5	312.8	0.11	0.14	0
49.5	312.3	0.10	0.14	0
57.5	312.4	0.10	0.13	0
65.5	312.8	0.10	0.13	0
73.5	313.3	0.10	0.13	0
81.5	313.8	0.10	0.13	31
89.5	312.3	0.07	0.09	65
97.5	311.8	0.05	0.06	88
Average (17.5-73.5 m)	313.0	0.10	0.13	–

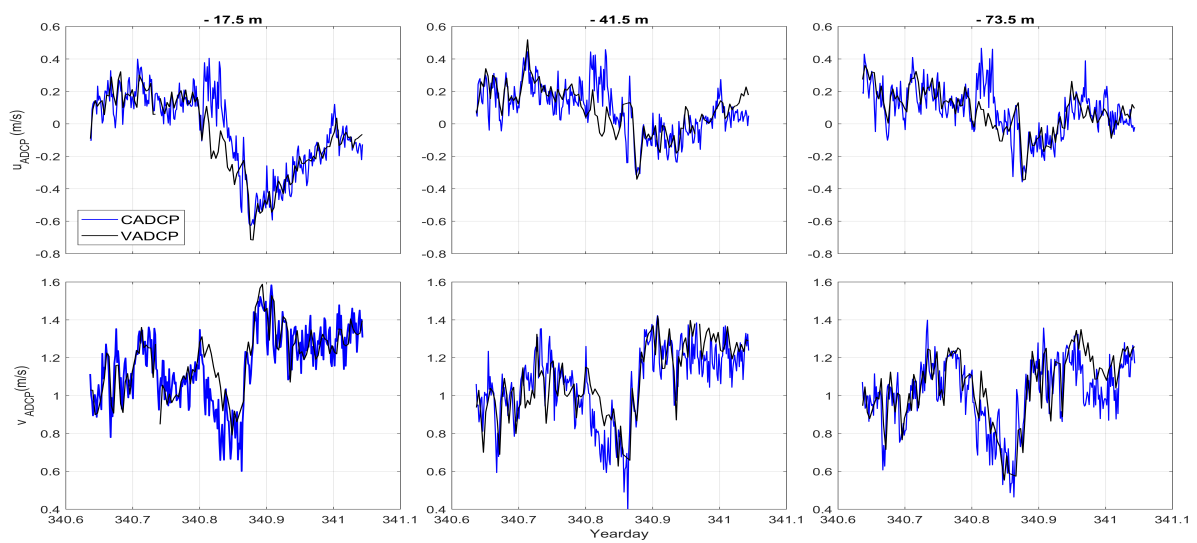


Figure B.1.: Comparison of velocity data between two ADCPs in geographical-based u and v components for -17.5, -41.5, and -73.5 m.

Appendix C.

Isopycnal averaging procedure

While averaging the parameters horizontally at constant depths across the thermocline, the lateral spatial information is generally lost because of the up and down movements of isopycnals. To eliminate this bias, it is useful to implement horizontally isopycnal-averaging. This method takes densities as the reference frame for the vertical coordinate instead of water depths, thus the coordinates become (x, y, σ_θ) . In the following, an example based on the data shown in Section 5.4.3 is demonstrated here.

The data used for laterally averaging along isopycnals, ranging from the upper limit $\rho_{up} = 25.57 \text{ kg m}^{-3}$ defined as the first non-titled isopycnal starting from the surface and lower limit $\rho_{lo} = 25.83 \text{ kg m}^{-3}$ defined as an arbitrary isopycnal below the thermocline where the stratification was relatively small as indicated by pink lines in Figure 5.8. The isopycnal layers are constructed with densities ρ_i reaching from ρ_{up} to ρ_{lo} with 20 intervals. For each density profile, the local depth of isopycnals z_i were computed corresponding to the densities ρ_i . While the ρ_i are constant, the z_i will be different for each profile. Using an interpolation scheme to transform the parameters (e.g. N^2 and ε) from their original z -positions to the z_i . The N_i^2 and ε_i are then the values of N^2 and ε at the isopycnal layers with density ρ_i . The interpolated data averaged along isopycnal layers for each index i over the different profiles denoted with a bracket $\langle \cdot \rangle$. For example, if the ε_i are the values corresponding to the ρ_i , then $\langle \varepsilon_i \rangle$ is the isopycnal average of ε over different profiles. Same averaging procedure for the z_i , the mean vertical position of isopycnal $\langle z_i \rangle$ can be computed. Finally, $\langle \varepsilon_i \rangle$ and $\langle N_i^2 \rangle$ as a function of $\langle z_i \rangle$ are shown in Figure 5.9a,b for comparison with 8-m vertical averaging. Note here that quantities are renamed as $\langle \varepsilon_\rho \rangle$, $\langle N_\rho^2 \rangle$, and $\langle z_\rho \rangle$ in Figure 5.9a,b to be clearly distinguished from 8-m vertical averaging.

Appendix D.

Curriculum vitae

Jen-Ping Peng

E-mail: jen-ping.peng@io-warnemuende.de

Phone: +49 (0) 381 5197-155



Current affiliation

Post-Doc at the Leibniz Institute for Baltic Sea Research (IOW), Germany

Jul. 2020 – present

Website: <https://www.io-warnemuende.de/jen-ping-peng-en.html>

Scientific educations and employments

Ph.D. in Physical Oceanography

Jan. 2017 – Dec. 2020

Leibniz Institute for Baltic Sea Research (IOW), Rostock, Germany

Supervisor: PD Dr. Lars Umlauf

Thesis: “Frontal Instability and Energy Dissipation in Submesoscale Fronts”

Research Assistant, National Cheng Kung University, Taiwan (R.O.C.)

Mar. 2016 – Dec. 2016

Supervisor: Prof. Dr. Dong-Jiing Doong

Research Assistant, National Taiwan Ocean University, Taiwan (R.O.C.)

Oct. 2014 – Feb. 2015

Supervisor: Prof. Dr. Dong-Jiing Doong

Intern (German Academic Exchange Service (DAAD) scholarship)

Jul. 2014 – Sep. 2014

Franzius institute, Leibniz University Hannover, Germany

Supervisor: Prof. Dr. Torsten Schlurmann

M.Sc. in Physical Oceanography (GPA: 3.8/4.0)

Sep. 2013 – Oct. 2014

National Taiwan Ocean University, Taiwan (R.O.C.)

Supervisor: Prof. Dr. Dong-Jiing Doong

Thesis: “A Study on Coastal Sea Surface Temperature Drop after Typhoon Passage”

Exchange student (Government scholarship)

Feb. 2013 – Jul. 2013

Swinburne University of Technology, Melbourne, Australia

Supervisor: Prof. Dr. Alexander V Babanin

B.Sc. in Oceanography (GPA: 3.3/4.0)

Sep. 2009 – Jun. 2013

National Taiwan Ocean University, Taiwan (R.O.C.)

Teaching assistant

Hydrodynamics (Bachelor level), Physics department, University of Rostock	Oct. 2018	—	Mar. 2019
Marine turbulence (Master level), Physics department, University of Rostock	Apr. 2019	—	Sep. 2019
MATLAB (Bachelor level), Department. of Marine Environmental Informatics, National Taiwan Ocean University (R.O.C.)	Sep. 2013	—	Feb. 2014

Field campaigns

1. Boundary layer flow in the Bornö Fjord with R/V Alice (University of Copenhagen) Sep. 2019
Main instruments: Turbulence microstructure profiler, Acoustic Doppler Velocimeter
2. Boundary layer flow over steep seafloor in the Northern Baltic Sea with R/V Electra Feb. 2019
(Stockholm University)
Main instruments: Turbulence microstructure profiler, Echo sounder (Simrad EK80)
3. Submesoscale processes in the Central Baltic Sea with R/V EMB (German research Nov. — Dec. 2018
foundation funded TRR181 project: Energy transfers in atmosphere and ocean)
Main instruments: Turbulence microstructure profiler, Catamaran-towed ADCP,
Seaglider
4. Submesoscale processes in the Central Baltic Sea with R/V EMB (German research Oct. — Nov. 2017
foundation funded TRR181 project: Energy transfers in atmosphere and ocean)
Main instruments: Turbulence microstructure profiler, Shipboard ADCP,
Thermistor chain

Computational skills

MATLAB (processing, analysis, and synthesis of large observed and satellite datasets)

Machine learning model (based on Artificial Neural Network)

Working in Linux/Windows environment

Language skills

Mandarin Chinese (Mother Tongue), English (Fluent), & German (Basic)

Peer-reviewed publications

1. **Jen-Ping Peng**, Lars Umlauf, Julia Dräger-Dietel, & Ryan North. Unforced frontal instability, inertial oscillation, and energy dissipation in a submesoscale upwelling filament, *Journal of Geophysical Research*, planned to be submitted in December 2020.
2. **Jen-Ping Peng**, Peter Holtermann, & Lars Umlauf (2020). Frontal instability and energy dissipation in a submesoscale upwelling filament, *Journal of Physical Oceanography*, 50, 2017 – 2023
3. Dong-Jiing Doong, **Jen-Ping Peng**, & Alexander V. Babanin (2019). Field investigations of coastal sea surface temperature drop after typhoon passages, *Earth System Science Data*, 11, 323 – 340.
4. Dong-Jiing Doong, **Jen-Ping Peng**, & Ying-Chih Chen (2018). Development of a warning model for coastal freak wave occurrences using an artificial neural network, *Ocean Engineering*, 169, 270 – 280.
5. Dong-Jiing Doong, Cheng-Han Tsai, Ying-Chih Chen, **Jen-Ping Peng**, & Ching-Jer Huang (2015). Statistical analysis on the long-term observations of typhoon waves in the Taiwan sea, *Journal of Marine Science and Technology*, 23, 893 – 900.

Scientific presentations

1. **Jen-Ping Peng** & Lars Umlauf. Frontal dynamics and turbulence in the upwelling filament under diurnal effects, *Virtual European Physical Oceanography and Shelf Sea Seminar Series*, online, 02 Dec. 2020 (**Oral presentation**).
2. **Jen-Ping Peng** & Lars Umlauf. Frontal instability and energy dissipation in submesoscale fronts, *Physics seminar at Leibniz Institute for Baltic Sea Research (IOW)*, online, 03 Nov. 2020 (**Oral presentation**).
3. **Jen-Ping Peng**, Peter Holtermann, & Lars Umlauf. Frontal instability and energy dissipation in a submesoscale upwelling filament, *Ocean Sciences Meeting*, San Diego, California, USA, 16–21 Feb. 2020 (**Oral presentation**).
4. **Jen-Ping Peng**, Peter Holtermann, & Lars Umlauf. Frontal instability and energy dissipation in a submesoscale upwelling filament, *Warnemünde Turbulence Days*, Vilm, Germany, 8–12 Dec. 2019 (**Oral presentation**).
5. **Jen-Ping Peng** & Lars Umlauf. Mixed-layer instabilities and turbulence in a submesoscale upwelling filament, *EGU General Assembly*, Vienna, 7–12 Apr. 2019 (**Poster presentation**).

Bibliography

- Bachman, S. D., B. Fox-Kemper, J. R. Taylor, and L. N. Thomas, 2017: Parameterization of frontal symmetric instabilities. i: Theory for resolved fronts. *Ocean Modell.*, **109**, 72–95.
- Barkan, R., K. B. Winters, and S. G. Llewellyn Smith, 2015: Energy cascades and loss of balance in a reentrant channel forced by wind stress and buoyancy fluxes. *J. Phys. Oceanogr.*, **45** (1), 272–293.
- Boccaletti, G., R. Ferrari, and B. Fox-Kemper, 2007: Mixed layer instabilities and re-stratification. *J. Phys. Oceanogr.*, **37** (9), 2228–2250.
- Capet, X., J. C. McWilliams, M. J. Molemaker, and A. Shchepetkin, 2008: Mesoscale to submesoscale transition in the California Current System. Part II: Frontal processes. *J. Phys. Oceanogr.*, **38** (1), 44–64.
- Charney, J. G., 1971: Geostrophic turbulence. *J. Atmos. Sci.*, **28** (6), 1087–1095.
- D’Asaro, E., C. Lee, L. Rainville, R. Harcourt, and L. Thomas, 2011: Enhanced turbulence and energy dissipation at ocean fronts. *Science*, **332** (6027), 318–322.
- D’Asaro, E. A., 1985: The energy flux from the wind to near-inertial motions in the surface mixed layer. *J. Phys. Oceanogr.*, **15** (8), 1043–1059.
- Dräger-Dietel, J., K. Jochumsen, A. Griesel, and G. Badin, 2018: Relative dispersion of surface drifters in the Benguela upwelling region. *J. Phys. Oceanogr.*, **48** (10), 2325–2341.
- Eden, C., L. Czeschel, and D. Olbers, 2014: Toward energetically consistent ocean models. *J. Phys. Oceanogr.*, **44** (12), 3160–3184.
- Eden, C., and R. J. Greatbatch, 2008: Towards a mesoscale eddy closure. *Ocean Modell.*, **20** (3), 223–239.

- Edson, J. B., and Coauthors, 2013: On the exchange of momentum over the open ocean. *J. Phys. Oceanogr.*, **43** (8), 1589–1610.
- Fairall, C., E. F. Bradley, J. Hare, A. Grachev, and J. Edson, 2003: Bulk parameterization of air-sea fluxes: Updates and verification for the COARE algorithm. *J. Climate*, **16** (4), 571–591.
- Feistel, R., and Coauthors, 2010: Density and absolute salinity of the Baltic Sea 2006–2009. *Ocean Sci.*, **6** (1), 3–24.
- Fox-Kemper, B., and R. Ferrari, 2008: Parameterization of mixed layer eddies. part ii: Prognosis and impact. *J. Phys. Oceanogr.*, **38** (6), 1166–1179.
- Fox-Kemper, B., R. Ferrari, and R. Hallberg, 2008: Parameterization of mixed layer eddies. part i: Theory and diagnosis. *J. Phys. Oceanogr.*, **38** (6), 1145–1165.
- Fox-Kemper, B., and Coauthors, 2011: Parameterization of mixed layer eddies. iii: Implementation and impact in global ocean climate simulations. *Ocean Modell.*, **39** (1–2), 61–78.
- Grisouard, N., 2018: Extraction of potential energy from geostrophic fronts by inertial–symmetric instabilities. *J. Phys. Oceanogr.*, **48** (5), 1033–1051.
- Gula, J., M. J. Molemaker, and J. C. McWilliams, 2014: Submesoscale cold filaments in the Gulf Stream. *J. Phys. Oceanogr.*, **44** (10), 2617–2643.
- Haine, T. W., and J. Marshall, 1998: Gravitational, symmetric, and baroclinic instability of the ocean mixed layer. *J. Phys. Oceanogr.*, **28** (4), 634–658.
- Hamlington, P. E., L. P. Van Roekel, B. Fox-Kemper, K. Julien, and G. P. Chini, 2014: Langmuir–submesoscale interactions: Descriptive analysis of multiscale frontal spin-down simulations. *J. Phys. Oceanogr.*, **44** (9), 2249–2272.
- Harlass, J., M. Latif, and W. Park, 2015: Improving climate model simulation of tropical atlantic sea surface temperature: The importance of enhanced vertical atmosphere model resolution. *Geophys. Res. Lett.*, **42** (7), 2401–2408.
- Hoskins, B. J., 1982: The mathematical theory of frontogenesis. *Annu. Rev. Fluid Mech.*, **14** (1), 131–151.
- Hoskins, B. J., and F. P. Bretherton, 1972: Atmospheric frontogenesis models: Mathematical formulation and solution. *J. Atmos. Sci.*, **29** (1), 11–37.

- Jay, D. A., J. Pan, P. M. Orton, and A. R. Horner-Devine, 2009: Asymmetry of Columbia River tidal plume fronts. *J. Mar. Syst.*, **78** (3), 442–459.
- Johnston, T. S., D. L. Rudnick, and E. Pallàs-Sanz, 2011: Elevated mixing at a front. *J. Geophys. Res. Oceans*, **116** (C11).
- Köhn, E. E., S. Thomsen, D. L. Arévalo-Martínez, and T. Kanzow, 2017: Submesoscale CO₂ variability across an upwelling front off Peru. *Ocean Sci.*, **13** (6), 1017–1033.
- Lévy, M., R. Ferrari, P. J. Franks, A. P. Martin, and P. Rivière, 2012: Bringing physics to life at the submesoscale. *Geophys. Res. Lett.*, **39** (14).
- Lévy, M., P. J. Franks, and K. S. Smith, 2018: The role of submesoscale currents in structuring marine ecosystems. *Nat. Commun.*, **9** (1), 1–16.
- Lévy, M., P. Klein, A.-M. Tréguier, D. Iovino, G. Madec, S. Masson, and K. Takahashi, 2010: Modifications of gyre circulation by sub-mesoscale physics. *Ocean Modell.*, **34** (1-2), 1–15.
- Lucarini, V., R. Blender, C. Herbert, F. Ragone, S. Pascale, and J. Wouters, 2014: Mathematical and physical ideas for climate science. *Reviews of Geophysics*, **52** (4), 809–859.
- Lucarini, V., and F. Ragone, 2011: Energetics of climate models: Net energy balance and meridional enthalpy transport. *Reviews of Geophysics*, **49** (1).
- Mahadevan, A., 2016: The impact of submesoscale physics on primary productivity of plankton. *Ann. Rev. Mar. Sci.*, **8**, 161–184.
- Mahadevan, A., and A. Tandon, 2006: An analysis of mechanisms for submesoscale vertical motion at ocean fronts. *Ocean Modell.*, **14** (3-4), 241–256.
- Mahadevan, A., A. Tandon, and R. Ferrari, 2010: Rapid changes in mixed layer stratification driven by submesoscale instabilities and winds. *J. Geophys. Res. Oceans*, **115** (C3).
- McWilliams, J. C., 2016: Submesoscale currents in the ocean. *Proc. Royal Soc. Lond.*, **472** (2189), 20160117.
- McWilliams, J. C., J. Gula, M. J. Molemaker, L. Renault, and A. F. Shchepetkin, 2015: Filament frontogenesis by boundary layer turbulence. *J. Phys. Oceanogr.*, **45** (8), 1988–2005.

- Millero, F. J., R. Feistel, D. G. Wright, and T. J. McDougall, 2008: The composition of standard seawater and the definition of the reference-composition salinity scale. *Deep Sea Res. Part I*, **55** (1), 50–72.
- Molemaker, M. J., J. C. McWilliams, and I. Yavneh, 2005: Baroclinic instability and loss of balance. *J. Phys. Oceanogr.*, **35** (9), 1505–1517.
- Moum, J., M. Gregg, R. Lien, and M. Carr, 1995: Comparison of turbulence kinetic energy dissipation rate estimates from two ocean microstructure profilers. *J. Atmos. Oceanic Technol.*, **12** (2), 346–366.
- Müller, P., J. McWilliams, and M. Molemaker, 2005: Routes to dissipation in the ocean: The 2D/3D turbulence conundrum. *Marine Turbulence*, 397–405.
- Nagai, T., A. Tandon, H. Yamazaki, and M. J. Doubell, 2009: Evidence of enhanced turbulent dissipation in the frontogenetic kuroshio front thermocline. *Geophys. Res. Lett.*, **36** (12).
- Nagai, T., A. Tandon, H. Yamazaki, M. J. Doubell, and S. Gallager, 2012: Direct observations of microscale turbulence and thermohaline structure in the Kuroshio Front. *J. Geophys. Res. Oceans*, **117** (C8).
- Nikurashin, M., and R. Ferrari, 2011: Global energy conversion rate from geostrophic flows into internal lee waves in the deep ocean. *Geophys. Res. Lett.*, **38** (8).
- Nikurashin, M., G. K. Vallis, and A. Adcroft, 2013: Routes to energy dissipation for geostrophic flows in the southern ocean. *Nat. Geosci.*, **6** (1), 48–51.
- Olbers, D., J. Willebrand, and C. Eden, 2012: *Ocean dynamics*. Springer Science & Business Media.
- Peng, J.-P., P. Holtermann, and L. Umlauf, 2020: Frontal instability and energy dissipation in a submesoscale upwelling filament. *J. Phys. Oceanogr.*, **50** (7), 2017–2035.
- Pollard, R. T., 1970: On the generation by winds of inertial waves in the ocean. *Deep Sea Research and Oceanographic Abstracts*, Elsevier, Vol. 17, 795–812.
- Ramachandran, S., and Coauthors, 2018: Submesoscale processes at shallow salinity fronts in the Bay of Bengal: Observations during the winter monsoon. *J. Phys. Oceanogr.*, **48** (3), 479–509.

- Risien, C. M., C. Reason, F. Shillington, and D. B. Chelton, 2004: Variability in satellite winds over the Benguela upwelling system during 1999-2000. *J. Geophys. Res. Oceans*, **109** (C3).
- Savelyev, I., and Coauthors, 2018: Aerial observations of symmetric instability at the north wall of the gulf stream. *Geophysical Research Letters*, **45** (1), 236–244.
- Sen, A., R. B. Scott, and B. K. Arbic, 2008: Global energy dissipation rate of deep-ocean low-frequency flows by quadratic bottom boundary layer drag: Computations from current-meter data. *Geophys. Res. Lett.*, **35** (9).
- Shannon, L., and G. Nelson, 1996: The Benguela: large scale features and processes and system variability. *The South Atlantic Past and Present Circulation*, Springer, 163–210.
- Smyth, W., and J. Moum, 2013: Marginal instability and deep cycle turbulence in the eastern equatorial Pacific Ocean. *Geophys. Res. Lett.*, **40** (23), 6181–6185.
- Snyder, S., P. J. Franks, L. D. Talley, Y. Xu, and S. Kohin, 2017: Crossing the line: Tunas actively exploit submesoscale fronts to enhance foraging success. *Limnol. Oceanogr.*, **2** (5), 187–194.
- Sullivan, P. P., and J. C. McWilliams, 2010: Dynamics of winds and currents coupled to surface waves. *Annu. Rev. Fluid Mech.*, **42**.
- Tandon, A., and C. Garrett, 1995: Geostrophic adjustment and restratification of a mixed layer with horizontal gradients above a stratified layer. *J. Phys. Oceanogr.*, **25** (10), 2229–2241.
- Taylor, J. R., and R. Ferrari, 2009: On the equilibration of a symmetrically unstable front via a secondary shear instability. *J. Fluid Mech.*, **622**, 103–113.
- Taylor, J. R., and R. Ferrari, 2010: Buoyancy and wind-driven convection at mixed layer density fronts. *J. Phys. Oceanogr.*, **40** (6), 1222–1242.
- Thomas, L., and J. Taylor, 2010: Reduction of the usable wind-work on the general circulation by forced symmetric instability. *Geophys. Res. Lett.*, **37** (18).
- Thomas, L. N., 2005: Destruction of potential vorticity by winds. *J. Phys. Oceanogr.*, **35** (12), 2457–2466.

- Thomas, L. N., A. Tandon, and A. Mahadevan, 2008: Submesoscale processes and dynamics. *Ocean modeling in an Eddying Regime. Geophys. Monogr. Ser.*, vol. 177, edited by M. W. Hecht and H. Hasumi, AGU, Washington, D. C., 17–38.
- Thomas, L. N., J. R. Taylor, E. A. D’Asaro, C. M. Lee, J. M. Klymak, and A. Shcherbina, 2016: Symmetric instability, inertial oscillations, and turbulence at the Gulf Stream front. *J. Phys. Oceanogr.*, **46** (1), 197–217.
- Thomas, L. N., J. R. Taylor, R. Ferrari, and T. M. Joyce, 2013: Symmetric instability in the Gulf Stream. *Deep Sea Res. Part II*, **91**, 96–110.
- Thomsen, S., T. Kanzow, F. Colas, V. Echevin, G. Krahmann, and A. Engel, 2016: Do submesoscale frontal processes ventilate the oxygen minimum zone off Peru? *Geophys. Res. Lett.*, **43** (15), 8133–8142.
- Xu, Z., P. Chang, I. Richter, and G. Tang, 2014: Diagnosing southeast tropical atlantic sst and ocean circulation biases in the cmip5 ensemble. *Climate dynamics*, **43** (11), 3123–3145.
- Yu, X., A. C. Naveira Garabato, A. P. Martin, D. Gwyn Evans, and Z. Su, 2019: Wind-forced symmetric instability at a transient mid-ocean front. *Geophys. Res. Lett.*, **46** (20), 11 281–11 291.

Selbstständigkeitserklärung

Ich versichere hiermit, dass ich die vorliegende Arbeit selbstständig verfasst und keine anderen als die angegebenen Quellen und Hilfsmittel benutzt habe. Ich versichere, dass die eingereichte elektronische Fassung mit den gedruckten Exemplaren übereinstimmt.

Rostock, 25.06.2020